Copyright
by
Shoupu Wan
2009

The Dissertation Committee for Shoupu Wan
certifies that this is the approved version of the following dissertation:

Atomic Fock States and Quantum Computing

Committee:

Qian Niu, Supervisor

Mark G Raizen, Supervisor

Allan H MacDonald

Gregory A Fiete

Charles Radin

Atomic Fock States and Quantum Computing

by

Shoupu Wan, B.S., M.S.

DISSERTATION

Presented to the Faculty of the Graduate School of

The University of Texas at Austin

in Partial Fulfillment

of the Requirements

for the Degree of

DOCTOR OF PHILOSOPHY

THE UNIVERSITY OF TEXAS AT AUSTIN

August 2009

Dedicated to:

my wife Li Yang

my parents Yu-Zhang Wan and Fu-Lian Ge

my brother Shou-Lu and sister Shou-Qin

Acknowledgments

I would like to take this opportunity to express my thanks toward Professor Qian Niu and Professor Mark Raizen.

Professor Niu is a highly esteemed scholar with an affable personality. I am impressed by the breadth and depth of his grasp of physics concepts. For just any research topics I wanted to start on, Professor Niu can always give me a jump-start. Professor Niu's group-meetings are especially enjoyable. With a blackboard and some chalk, he shares many hard-to-find insights with us. Moreover, with his encouragements, I dare to ask the silliest questions.

Through the years, I am impressed by Mark's leadership, confidence, and orderliness. He has the vision. More importantly, he has the method to realize his vision. Mark cares about every progress of his students. I especially enjoyed conversations with him, through which I learned how to lead a successful life. He taught me all kinds of skills, including writing skills, people skills, and how to improve them.

Though short, the time I spent with both of them is very enjoyable and will certainly be of great value for the rest of my life.

The next person I would like to thank is Professor John Markert. During the late years of my PhD study, I was forced to switch dissertation advisor. I had a chance to talk to Professor Markert about my situation. He showed

strong support and deep sympathy for me. He did a lot more than he has to to help me get over the difficulty. I am in debt to Professor Markert.

I want to thank Professor Allan MacDonald. His lectures are full of wisdoms that nobody could afford to miss. Also, Allan is very kind to students in the Department. As a worldwide renowned scientist, Allan helped check my application status and emailed it to me, before I entered UT!

Thanks are due to Professor Gregory Fiete, who provided inspiring suggestions at the beginning of my theoretical research. Chatting with him is always beneficial and pleasant.

I must thank Professor Charles Radin in the Department of Mathematics. Professor Charles Radin serves on my committee and is always happy to answer my mathematical inquiries.

Thanks are also due to Professor William Beckner in the Department of Mathematics, who has been a helpful figure during my PhD studies.

I also want to thank other faculty members in the Department: Professor Linda Reichl, Professor Michael Downer, Professor George Sudarshan, Professor Greg Sitz, Professor Manfred Fink, Professor Austin Gleeson, and Professor Daniel Heinzen.

I feel compulsory to acknowledge several faculty members outside the Department, who provided me many opportunities that are otherwise unavailable. They are Professor Sanjay Banerjee and Professor Ray Chen from the Department of Electrical & Computer Engineering, Mr. Glenn Downing, Pro-

fessor Greg Plaxton, and Professor Emmett Witchel from the Department of Computer Sciences.

Many of the staff members in the Department have been very helpful and friendly. It is my pleasure to acknowledge their services here. They are Carol Noriega, Linda Hallidy, Becky Drake, Olga Vorloou, Pat Morgan, Eric Hayes Patkowski, Jack Clifford, Allan Schroeder, and Glenn Suchan.

I appreciate the friendships and helps from several graduate students and postdocs. I thank Dr. Changhyun Ryu, Dr. Emek Yesilada, Dr. Xu Du, and Dr. Wooshik Shim, for their hands-on help in my early years of PhD study. The students and postdocs in Professor Raizen's group, Professor Niu's group and some AMO physics groups are always great resources to resort to: Tongcang Li, Hrishikesh Kelkar, Travis Bannerman, Charlotte Sanders, Rob Clark, Thomas Jarvis, Michael Borysow, Rudy Kohn, Philip Smith, Minxi Jiang, Chih-Piao Chuu, Shengyuan Yang, Tianyi Cai, Hui Pan, et al.

The author also appreciate the friendships from fellow Chinese students: Rongxing Huang, Shengyong Qin, Tianchun Zhou, Fanglei Zhuang, Peng Dong, Tingji Tang, Wei Lu, Zhaorigetu Chen, and more.

My wife, Yang Li, deserves a special position in my acknowledgment list. She is a brave woman. She is constantly supportive throughout our marriage and especially during my PhD study at UT. She undertook most of the tasks and met the needs of the family. She provided me a warm home. She consoled me when I felt frustrated. Most importantly, she brought our

two daughters, Sannie and Jenna, to this family. Without her love, I would have done little.

I would like to thank my parents, my brother, my sister and other members in the family, for their enduring love and encouragements. I also appreciate the support and understanding of my parents-in-law, Fu-Cai Yang and Zhong-Fang Cang. They have been very generous to us during the years of hardship and frustration.

The author would like to give special thanks to Kirsten Viering, Isaac Chavez, David Medellin, Rudy Kohn, and Shengyuan Yang for proofreading this dissertation.

S.P.W.

July 27, 2009

Austin, TX

Atomic Fock States and Quantum Computing

Publication No. _____

Shoupu Wan, Ph.D.
The University of Texas at Austin, 2009

Supervisors: Qian Niu
Mark G Raizen

The potential impact of quantum computing has stimulated a world-wide effort to develop the necessary experimental and theoretical resources. In the race for the quantum computer, several candidate systems have emerged, but the ultimate system is still unclear. We study theoretically how to realize atomic Fock states both for fermionic and bosonic atoms, mainly in one-dimensional optical traps. We demonstrate a new approach of quantum computing based on ultracold fermionic atomic Fock states in optical traps.

With the Pauli exclusion principle, producing fermionic atomic Fock states in optical traps is straightforward. We find that laser culling of fermionic atoms in optical traps can produce a scalable number of ultra-high fidelity qubits. We show how each qubit can be independently prepared, and how to perform the required entanglement operations and detect the qubit states

with spatially resolved, single-atom detection with adiabatic trap-splitting and fluorescence imaging.

On the other hand, bosonic atoms have a strong tendency to stay together. One must rely on strong repulsive interactions to produce bosonic atomic Fock states. To simulate the physical conditions of producing Fock states with ultracold bosonic atoms, we study a many-boson system with arbitrary interaction strength using the Bethe ansatz method. This approach provides a general framework, enabling the study of Fock state production over a wide range of realistic experimental parameters.

Table of Contents

Acknowledgments **v**

Abstract **ix**

List of Tables **xiv**

List of Figures **xv**

Chapter 1. Introduction to Ultracold Atomic Physics and Atomic Fock States **1**

1.1 Cooling of atoms 1
1.1.1 Sisyphus cooling and optical molasses 3
1.2 Trapping and storing of atoms 10
1.2.1 Magnetic traps 11
1.2.2 Optical dipole trap 13
1.2.3 Magneto-optical traps 16
1.3 Bose-Einstein condensates 17
1.4 Atomic Fock states and quantum computing 18
1.5 The DiVincenzo criteria for quantum computing 18
1.6 Interacting many-boson systems and the Bethe ansatz method 19
1.7 Organization of the dissertation 21

Chapter 2. Quantum Computing with Ultracold Fermionic Atoms in Optical Traps **23**

2.1 Preparation of fermionic Fock states 24
2.2 Simulation models 26
2.2.1 Laser-culling 26
2.2.2 Adiabatic trap-splitting 34
2.3 Fidelity of preparing fermionic atoms in ground Fock states . 36

2.4 Scalability 42
2.5 Entanglement generation and implementation of universal gates 44
2.6 Qubit State Detection 48
2.7 Sources of decoherence 50
2.8 The DiVincenzo criteria 53

Chapter 3. Calculations of Atomic Fock States Using Bethe Ansatz 55
3.1 Strongly interacting atoms 55
3.2 Formulation of the problem 57
3.3 The perturbation and variational solutions 60
3.4 Bethe Ansatz solutions 63
3.5 More about the single-particle energies 70
3.6 Atomic Fock states 74

Chapter 4. Conclusion 81

Appendices 83

Appendix A. Controlling laser power, laser frequency, and temperature 84
A.1 Basics of PID control 85
A.1.1 Feed forwards 89
A.2 Lock-in amplification 90
A.3 Saturated absorption spectroscopy 92
A.4 Frequency controls in a semiconductor diode laser 96
A.5 Temperature Control 98
A.6 Laser power control 99

Appendix B. Issues Related to Bethe Ansatz 102
B.1 Truncations on the boundary conditions in Bethe ansatz method 102
B.2 Valid Bethe ansatz solutions 107
B.3 Energy-level ordering of Bethe ansatz states 109

Appendix C. The Wentzel-Kramers-Brillouin (WKB) method 111

Bibliography **117**

Index **129**

Vita **131**

List of Tables

1.1 The Mid-Level Quantum Computation Roadmap: Promise Criteria. 20

A.1 Ziegler-Nichols tuning method 87

List of Figures

1.1 Examples of magnetic sublevels and transition matrix elements. Due to the selection rule of electric dipole transition, a transition between substates with equal m_F must absorb or emit a photon with linear polarization and that between substates with m_F's differing by ± 1 must absorb or emit a photon with $\sigma^{\pm}$ polarization, respectively. The numbers by the lines connecting a ground and an excited state are the Clebsch-Gordan coefficients for the corresponding transition. **a** Level diagram for a bosonic atom whose ground states have quantum numbers $F = 1$, $m_F = \pm 1, 0$ and excited states have quantum numbers $F = 2$, $m_F = \pm 2, \pm 1, 0$. **b** Level diagram for a fermionic atom whose ground states have quantum numbers $F = 1/2$, $m_F = \pm 1/2$ and excited states have quantum numbers $F = 3/2$, $m_F = \pm 3/2, \pm 1/2$. 6

1.2 Polarization gradients in one-dimensional optical field. The surfaces (red) represent the trace of the end of the electric field vectors at various positions z over a period of the wave oscillation. The lines (black) highlight a few positions $z_1, z_2, \cdots$. **a**. σ^+-σ^- configuration. The laser field is formed by two circularly polarized, counter-propagating beams with opposite helicity. This configuration induces a static magnetic field in the frame of a moving atom whose hyperfine splitting causes a frequency shift in addition to the Doppler shift. **b**. lin$\perp$lin configuration. The laser field is formed by two linearly polarized, counter-propagating beams with orthogonal polarization planes. 7

1.3 **a**. Magnetic coils for a Ioffe-Pritchard-type trap. **b**. Magnetic trapping potential of a Ioffe-Pritchard trap in the x-z plane. . 12

1.4 Rabi oscillations as these occur in 2-level atom driven by coherent laser field with detunings 0 (blue), 3γ (purple), 6γ (yellow), and 9γ (green), where γ is the absorption peak width. The average population in the excited state is proportional to δ^{-2}, as $\delta \to \infty$. 14

1.5 **a.** Schematic drawing of a magneto-optical trap. Three orthogonal pairs of counter-propagating laser beams converge to the trap center(shown as red directed lines). All laser beams are red-detuned with respect to the resonance frequency. A pair of anti-Helmholtz coils (shown in gray, the arrows denotes the direction of current) generate magnetic fields (shown as black lines). The laser beams converge onto the point with minimum magnetic field, where atoms are collected and trapped (shown in blue). The laser beams are also used for optical molasses with sub-Doppler cooling mechanism. The six circular lines denote the helicities of the circular polarizations. **b.** The difference of the Zeeman shifts as function of position in a 1D MOT. δ is the laser detuning. Atoms are confined approximately to $[-x_0, x_0]$ (the gray area). 16

2.1 Steps used in producing ultra-high-fidelity qubits. **I**. A degenerate Fermi gas, produced by evaporative cooling, whose interaction strength is tuned to zero ($B \approx 0$). **II**. Adiabatic laser-culling removes all of the atoms except a pair of atoms in the ground state of the trap which have opposite spins, following the Pauli exclusion principle. Due to the applied magnetic field gradient, the two spin states experience different potentials. Only the potential for the $|\uparrow\rangle$ state is shown. **III**. An adiabatic trap-splitting separates the pair into two adjacent micro-traps. Potentials for both spin states are shown (solid and dashed). . 25

2.2 The trapping potentials used in the simulations. **a**. Truncated harmonic trap. The truncation energy E_t and truncated trap size (or simply trap size) z_t are shown. **b**. Truncated harmonic trap with a positive magnetic gradient. The trap size, z, is defined as the length of the parabolic part in the potential profile. Dashed lines denote the level of the ground and first-excited state. 27

2.3 Exact numerical calculation for truncated harmonic trap with trap size $z = 4.14$. Dashed lines denote the eigen-energy level of the ground and first-excited state. The trapping potential of the truncated harmonic trap is depicted (dot-dashed). The unit of energy is $\hbar\omega$ and energy reference is set at the bottom of the trap. 28

2.4 Comparison between exact numerical calculations and WKB approximation. **a**. Ground-state wavefunction comparison at fixed trap size $z = 4.14$. The left vertical axis is the probability density; the right axis depicts the trapping potential (dot-dashed) and energy level. The ground state wavefunctions of the direct numerical calculation (solid) is compared with that obtained with the WKB method (dashed). **b**. Ground-state eigen-energy as a function of the truncation size z. The vertical lines show the ionization thresholds for atoms in the first (solid thick), second (solid thin), third (dot-dashed), and fourth (dashed) excited states. 29

2.5 Laser-culling simulation model. Parameters used in the simulation: the trap size is $4.4x_0$, the magnetic force is $0.5\hbar\omega/x_0$. **a** Density of states (DOS). The vertical dotdashed line denotes the barrier height of the trap. Inset: Lorentzian (solid) and Gaussian (dashed) regressions of the resonance peak at $E \approx 0.365$ and the unit of the horizontal axis is this peak's FWHM. **b** Stationary wavefunction at $E \approx 0.365$. Inset shows the panorama of the wavefunction. **c** Stationary wavefunction at $E \approx 1.29$. . 31

2.6 Peak width (FWHM) ratio of the excited state to the ground state (in base-10 logarithmic scale) as function of the trap size and magnetic gradient, in the laser-culling process. The white color represents out-of-range color, *i.e.*, should be colored more than its surrounding. 33

2.7 Simulation model of separating a pair of atoms in opposite spin states. The parameters shown in this figure are d, the distance between the energy minima (in unit of x_0), and g, the force produced by the applied magnetic field gradient (in unit of $\hbar\omega/x_0$). Dashed lines show the energy levels of the ground and first excited state, obtained numerically. The excitation gap is defined as the energy difference between the two levels. 35

2.8 Excitation gap (in unit of $\hbar\omega$) during adiabatic trap-splitting for separating a pair of ultracold ^{6}Li atoms. Red (blue) color represents large (small) excitation gap. The horizontal axis is the magnetic force g and the vertical axis is the distance d. . 37

2.9 Holding time (in unit of $1/\omega$) during the laser-culling process. The scale of the contour plot is in base-10 logarithmic scale. Redder color represents longer holding time. 39

2.10 Fidelity of laser-culling. Shown is the base-10 logarithm of the ground state fidelity loss. Red (blue) color represents high (low) fidelity. The white areas are out-of-range clippings: near the left-hand side, the white areas should be redder than its surrounding color; near center-top, the white area should be bluer than its surrounding color. 40

2.11 Loss of fidelity during trap-splitting. Shown in base-10 logarithmic scale. Red (blue) color represents high (low) fidelity. We assume complete suppression of excitation by maintaining a sufficient energy gap and keeping the process adiabatic. The horizontal axis is the magnetic force g and the vertical axis is the distance d. 42

2.12 Array of $2N$ optical traps. With the scalability of our system, we can prepare a fiducial antiferromagnetic state with $2N$ qubits. 44

2.13 Artist's concept of a 4×4 matrix of fermionic, Fock-state qubits, initialized to fiducial antiferromagnetic state with 16 qubits. Red (blue) color in the trapping potential means higher (lower) energy. Atoms are shown as little balls, with blue color meaning spin-up, red-color spin-down. All atoms are in the ground-state of the micro-traps. By moving the containing micro-trap, each atom can be made to engage in a two-qubit gate operation with each other atom by the qubit transport technique [10]. 45

3.1 Configuration space for a 3-atom system. The space is divided by the δ-interaction into wedged open spaces. The red, blue, and green surfaces denotes the positions where the atom-atom interactions take place. Together with the square-well potential, the spaces where atoms can move freely are the so-called Weyl Chambers [60]. 58

3.2 Eigenenergies of Equation (3.5) for weakly interacting atoms with perturbation and variational methods. The zero energy reference is the bottom of the square well. **a**. The average energy per atom for a system of 2 through 17 atoms. **b**. The single-particle energies of 17 interacting atoms. 62

3.3 Bethe ansatz states for sodium atoms. The total energy of 4-particle bound states are plotted against trap depth (**a**) and interaction strength (**b**). The numbers at the beginning of each energy level are the quantum numbers of the bound state. We used the bottom of the trap as the energy zero. Trap size $L = 5$ μm. Transverse trapping frequency $\omega_\perp = 2\pi \times 150$ kHz. . . 69

3.4 Bethe ansatz single-particle energies for sodium atoms. The energy zero is set to the bottom of the trap. The horizontal axis is the interaction c (in unit of $\hbar^2/2mL^2$) and the vertical is the single-particle energy (circle, square, diamond, and triangle in that order). Trap size $L = 5$ μm. Transverse trapping frequency $\omega_\perp = 2\pi \times 150$ kHz. Panel from **a**-**h** shows the ground state and the lowest 7 excited states of Bethe ansatz solutions as shown in Figure 3.3. 71

3.5 **a.** Single-particle energies of 2 sodium atoms in a square well of width 100 μm. **b.** Zoomed-in view of the dip in the lowest single-particle energy. 72

3.6 Gedanken experiment designed to probe the 'single-particle' (quasi-particle) energy. The experimental setup consists of an ultracold atom source (S), a controlling gate (G) and a drain (D). We assume S is full of particles while D is empty. The 1D many-atom system (System) is embedded between the source and the gate. The source, system, gate, and drain are separated by δ-barriers, which may be generated by tightly focused blue-detuned laser beams. The source and drain may be considered as reservoirs whose chemical potentials can be controlled. The experiment is designed to detect the atomic 'current', which is throttled by the gate energy offset and/or size through the resonant tunnelling. The energy levels are drawn schematically. 73

3.7 Single-particle energies of 4 sodium atoms in Bethe ansatz ground states. Trap size $L = 5\mu$m. **a.** Dependence on interaction strengths (c). Trap depth $V_0 = k_B \times 25$nK, where k_B is Boltzmann's constant. The dotdashed vertical line denotes the maximum interaction strength above which no Bethe ansatz state of 4-atom system exists. The other two vertical lines denote the interaction strengths of sodium (dotted) and ^{87}Rb (dashed) atoms at $\omega_\perp = 2\pi \times 150$ kHz and zero magnetic field. Inset, the trap depth is lifted to $k_B \times 40$nK, the condition at which all 4 atoms remain trapped to the Tonks limit. **b.** Dependence of the single-particle energies of a 4-atom system on the trap depth (V_0). Transverse trapping frequency $\omega_\perp = 2\pi \times 150$ kHz. Magnetic field is zero. The vertical line (dotdashed) denotes the minimum trap depth below which no bound state of the 4-atom system exists. 74

3.8 Ionization thresholds of sodium atoms with all parameters fixed except trap depth. Only highest single particle energies of the Bethe ansatz N-atom states are shown for $N = 2$ (circle), 3 (square), 4 (diamond), 5 (upright triangle), and 6 (invert triangle). Trap size $L = 5$ μm; Transverse trapping frequency $\omega_\perp = 2\pi \times 150$ kHz. The ionization thresholds (with the current numeric calculation step size) are also ticked along the horizontal axis. 76

3.9 Map of Fock states and the calculated ionization thresholds for sodium atoms in a 1D optical trap in the adiabatic limit. Transverse trapping frequency $\omega_\perp = 2\pi \times 150$ kHz and zero magnetic field are assumed. The interaction strength is implicit in the unit we adopted, since c^{-1} and $\hbar^2 c^2/m$ are used to make the axes dimensionless. **a.** Contour plot of Fock states as function of trap depth and size; **b.** and **c.** views of cross-sectional cuts along the lines indicated in **a**, respectively. The ticks on horizontal axes give the corresponding ionization thresholds. . 77

3.10 Excitation energy gaps between ground and first-excited states as function of trap depth for 2 (circle), 3 (square), 4 (diamond), 5 (upright triangle), and 6 (invert triangle) sodium atoms. Trap size is 5 μm. 79

A.1 **a** The PID control flowchart. Arrow denotes direction of control flow. The detector senses fluctuations in the process (red) and sends error signal to the PID controller (labelled as P, I, and D, respectively). The outputs of the PID controller is summed and applied to the process to reduce the fluctuation. **b**. The Bode plots of the transfer functions of the P, I, D control units (black), and the process (red). The latter is assumed to be a two-stage amplifier which starts to roll off at 12dB/octave at frequency f_c [46]. 86

A.2 The Bode plot of the response frequencies of the weighed sum of the P, I, and D control units (black) after the PID tuning. The transfer function of the system is characterized by a two-stage RC-filter (red). Their product gives the overall loop gain, whose Bode plot is shown (green). 88

A.3 **a.** Absorption peak as measured by the voltage output of a photodiode. Without using lock-in amplification, the best locking reference level are as shown in the dashed line and the resulted laser frequency is one of the side points (red) of the absorption peak. **b.** The decoded lock-in signal for the absorption peak. With the lock-in amplification, an absolute reference signal at 0 volt can lock laser frequency on the center of the absorption peak. 90

A.4 Experimental set-up for saturated absorption spectroscopy. . . 93

A.5 **a.** Population distribution of the ground state (blue) and the excited state (purple) for a blue-detuned laser frequency. The absorptions distribution of the probe beam is also shown (dashed). **b.** The saturated absorption spectroscopy for an isolated transition. When the peak in the dashed line and the burnt hole aligns at $v = 0$, a peak appears. 94

A.6 **a.** Two transitions sharing one ground state. **b.** Two transitions sharing one excited state. 95

A.7 **a.** Population distribution of the ground state (blue) and the excited state (purple) The absorption distribution of the probe beam has two peaks corresponding to the two transitions ω_1 and ω_2 (dashed). **b.** The saturated absorption spectroscopy for an isolated transition. 96

A.8 Diffraction grating used in Littrow configuration for use in a semiconductor diode laser. 97

A.9 PID temperature control servo circuit. Starting from upper left are 1) a bridge with a thermistor on one of the 4 arms, error signal generation unit, 2) differential amplifier, error signal filtering and amplifying unit, 3) integral, derivative, and proportional feedbacks, 3) heater, actuator, respectively. 98

A.10 A laser power stabilization system **a** The schematic drawing for the feedback loop. The laser power in the chamber is the control object. The laser power exiting the vacuum chamber is detected by a photodiode. The difference between the output voltage and a preset voltage is taken as the error signal. This error signal is amplified and conditioned in the feedback control circuit. Finally, the circuit outputs a voltage to adjust the laser power dissevered to the chamber. **b** The feedback control circuit. The reference voltage is generated by a temperature-stabilized zener diode. A simple integral control is used. All electronic components in the feedback loop are of high bandwidth so that the overall signal has a bandwidth ≥ 1 MHz. 101

B.1 Configuration space and boundary conditions for a 2-boson system. The perpendicular dotted lines, x_1 and x_2, are the coordinate axes. The solid lines at $x_{1,2} = \pm\frac{x_0}{2}$ denotes the square well enclosed by potential barrier. The solid diagonal line $x_1+x_2 = 0$ denotes where δ-interaction takes place; the anti-diagonal line $x_1 - x_2 = 0$ (dashed) denotes the additional space-reflection symmetry. The other dashed lines are boundaries for the problem. The numbers 1-8 denote the regions that have distinct forms of wavefunctions where regions 1 & 2, 1 & 3, 5 & 6, and 7 & 8 are related by space-reflection symmetry, respectively. . 104

B.2 Verification of the Bethe ansatz solutions using solutions at $c = 0$. The title of each panel denotes the quantum numbers that are used for the calculation; the horizontal axis denotes the interaction strengths; the vertical axis denotes the wave numbers of the Bethe ansatz solutions. The red bold numbers together with the dotdashed lines in each panel denotes the wave numbers of the solutions at $c = 0$. The quantum numbers $\{0, 1, 2, 3\}$ and $\{1, 2, 2, 3\}$ denote states that have no valid limit as $c \to 0$. 108

C.1 The trapping potential used for the WKB calculation. For $|x| \leq z_t/2$, the trap is parabolic; for $|x| > z_t/2$, the trap is assumed to be flat. The truncation energy E_t, truncated trap size z_t, atom energy E and classical turning point $z/2$ are as shown. A patching region (gray rectangle)is constructed around the turning point. 112

Chapter 1

Introduction to Ultracold Atomic Physics and Atomic Fock States

In this chapter, we give an introduction to some of the most relevant physics and technology. We review the rudiments of cooling and trapping of neutral atoms using laser and magnetic fields [1], on which the main topics are based upon. We give the motivation for simulating the production of atomic Fock states and why we choose fermionic atoms confined in arrays of optical traps as the basic building block for quantum computing.

1.1 Cooling of atoms

Temperature is one of the most basic concepts in physics. To get an insight on what temperature is, we need to consider a macroscopic system consisting of a large number of atoms confined in a fixed spatial volume, for example, atoms in an optical trap (which will be explained in later sections). The number of accessible states of such a system is myriad, because of the enormous degrees of freedom. The entropy of such a system is defined as the

[1] Some of the work presented in this chapter is done under the supervision of Professor Daniel J. Heinzen

logarithm of the total number of accessible states for a given particle number, energy, etc. With its statistical definition, the temperature of this system is the inverse of the derivative of *entropy* to the *internal energy*, with particle numbers held constant. As is known in quantum mechanics, such a system has at least one (sometimes more) ground state with a *minimum* total energy (the ground level). For most systems, the number of accessible states at or near the ground level is limited and scarce. The merit of physics lies in studying a relatively simple system. Even a complex system becomes simple when cooled to sufficiently low temperature—you get the unwanted complexities frozen out and the target of study conspicuous.

There are different ways to interpret the cooling process under different contexts. From the perspective of information theory, the entropy of a system describes how chaotic the states of its constituents are. To cool a system is to fix the irregularities. By virtue of the thermodynamic second law, entropy never decreases in a large, isolated system. Thus to cool a system is to extract its entropy and dump it to the environment [16, 17, 85, 87].

In statistical physics, the set of accessible states form a distribution in phase space and each state in the set is equally likely to be occupied. In this case, entropy is defined as logarithm of the total volume of the phase space subtended by the set of accessible states. From this point of view, a cooling process contracts the phase-space volume occupied by the accessible states [70]. From the aspect of quantum statistical mechanics, an ensemble of dilute

gas is described by a density matrix

$$\sum_{i=1}^{N} |a_i|^2 \, |\phi_i\rangle \, \langle\phi_i|, \tag{1.1}$$

where $|\phi_i\rangle$ represents the eigenstate with the ith lowest eigen-energy and $\sum_i |a_i|^2 = 1$. The colder a system is, the smaller the upper limit N becomes. Therefore in this sense, to cool a system is to press the non-zero elements in the density matrix toward the ground level end.

Laser cooling relies on the interaction between atoms and photons, where photons act as the entropy carriers. We examine the mechanism and condition for laser cooling in the following subsection.

1.1.1 Sisyphus cooling and optical molasses

In a thick media, a freely moving ball eventually gets stuck in the media. This is because of the viscous force between the media and the ball which tends to unify the motion of ball and the media. This is exactly analogous to the classical picture of laser cooling. Let us start our analysis with the simplest atomic model: a fiducial 2-level atom, which has one absorption resonance peak with center frequency ω_0 and full-width-half-maximum (FWHM) γ. The interaction between such an atom and a laser beam is described by a series of alternating absorptions and emissions. Since each photon carries a momentum, $\hbar\omega/c$, where $\hbar = h/2\pi$ and h is Planck's constant, c is speed of light, absorbing a photon causes the atomic momentum to change. The absorptions are dominated by stimulated absorptions from the laser beam, while

both spontaneous and stimulated emissions are significant. If a stimulated absorption is followed by a stimulated emission, it leaves no change in the atom's momentum. If a stimulated absorption is followed by a spontaneous emission in random direction, the average effect is that the atom acquires momentum in the direction of the laser beam. This acquired momentum could cause increased or decreased kinetic energy with equal probability. So there is no net cooling of the atom.

However, an additional ingredient to the above picture is the relativistic Doppler effect, by which the actual angular frequency of the incident light 'seen' by the atoms is

$$\omega^* = \frac{1 - \beta \cos\theta}{\sqrt{1 - \beta^2}} \omega, \tag{1.2}$$

where $\beta = |\vec{v}|/c$, $\vec{v}$ is the velocity of the atoms, c is the speed of light, θ is the angle of the incident light relative to the direction of $\vec{v}$. From Equation (1.2), if an atom's motion is toward ($\theta = 180\,^\circ$) or away from ($\theta = 0\,^\circ$) the source of light, it 'sees' bluer or redder than normal. Now suppose we tune the frequency of the laser beam to the redder side by $|\delta| > \gamma$ (red-detuned). Frequency compensation from the Doppler effect happens to be that if atoms move toward (away from) the laser source, the laser frequency is closer to (further from) the atomic absorption resonance frequency. Therefore the overall effect is atoms moving toward the laser source with certain speed get slowed down, while all other atoms experience no effect. With more laser beams incident from other directions, more atoms will be slowed down. The laser cooling experiment based on this classical picture would be set up with 3 counter-propagating

pairs of laser beams and each pair is orthogonal to the others [20, 41]. All laser beams are red-detuned by the same amount. Within a certain velocity range, wherever it is moving, an atom will be slowed down. The overall effect is that atoms are 'jammed' in the laser light. The minimum temperature reachable by the above cooling mechanism, limited by the Doppler effect, is $\hbar\gamma/2k_B$, where k_B is Boltzmann's constant. This is because of the finite width in the absorption resonance peak which transforms to a finite speed range in the slowed atoms by the Doppler effect. A finite speed range means non-zero kinetic energy range.

However, it is observed in experiment that much lower temperatures can be reached with a slightly modified optical molasses [59]. Soon after that, a quantum mechanical cooling mechanism with multilevel atoms in polarization-gradient field was proposed [24, 92]. The cooling effect of optical pumping of a multilevel atom in laser fields with certain polarization gradient was largely ignored in the previous analysis of classical laser-cooling mechanism. Next, we examine two cooling mechanisms that are independent of the Doppler cooling mechanism. The first one occurs in multilevel atoms with level diagrams as shown in Figure 1.1**a** in a 1D standing wave with polarization configuration as shown in Figure 1.2**a**. The polarization configuration shown in Figure 1.2**a** results from two counter-propagating same-frequency laser beams with circular polarizations of opposite helicities (thus given the name σ^+-σ^-). The second cooling mechanism occurs in multilevel atoms with level diagram as shown in Figure 1.1**b** in a standing-wave laser field with polarization of the kind shown

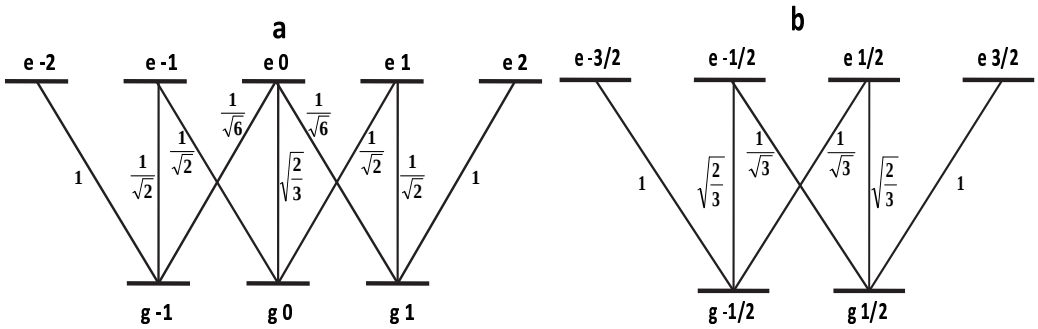

Figure 1.1: Examples of magnetic sublevels and transition matrix elements. Due to the selection rule of electric dipole transition, a transition between substates with equal m_F must absorb or emit a photon with linear polarization and that between substates with m_F's differing by ± 1 must absorb or emit a photon with $\sigma^{\pm}$ polarization, respectively. The numbers by the lines connecting a ground and an excited state are the Clebsch-Gordan coefficients for the corresponding transition. **a** Level diagram for a bosonic atom whose ground states have quantum numbers $F = 1$, $m_F = \pm 1, 0$ and excited states have quantum numbers $F = 2$, $m_F = \pm 2, \pm 1, 0$. **b** Level diagram for a fermionic atom whose ground states have quantum numbers $F = 1/2$, $m_F = \pm 1/2$ and excited states have quantum numbers $F = 3/2$, $m_F = \pm 3/2, \pm 1/2$.

in Figure 1.2**b**. The polarization configuration shown in Figure 1.2**b** results from two counter-propagating same-frequency laser beams with orthogonal linear polarizations (thus the name lin$\perp$lin).

Firstly, let us study fiducial atoms from Figure 1.1**a** in polarization gradient field of σ^+-σ^- configuration of Figure 1.2**a**. From the illustration of the polarization field, an atom that sits still in the light field will interact with a (locally) linearly polarized electromagnetic field. Thus the $|g, -1\rangle$ and $|g, +1\rangle$ are equally populated, because there is no net optical pumping. However for a moving atom toward the source of the σ^+ laser beam,

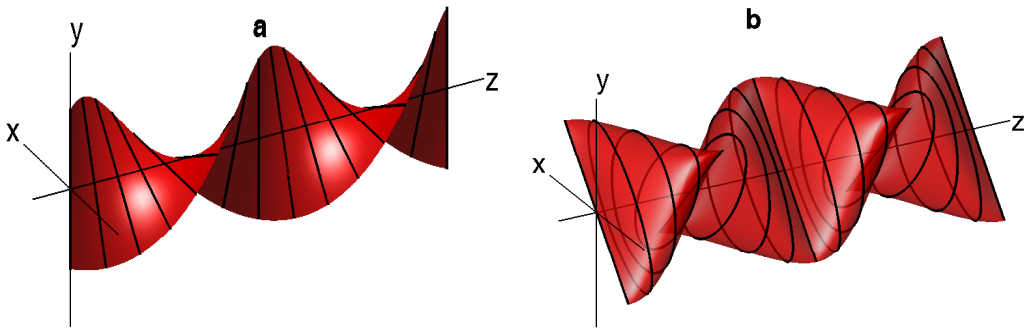

Figure 1.2: Polarization gradients in one-dimensional optical field. The surfaces (red) represent the trace of the end of the electric field vectors at various positions z over a period of the wave oscillation. The lines (black) highlight a few positions $z_1, z_2, \cdots$. **a**. σ^+-σ^- configuration. The laser field is formed by two circularly polarized, counter-propagating beams with opposite helicity. This configuration induces a static magnetic field in the frame of a moving atom whose hyperfine splitting causes a frequency shift in addition to the Doppler shift. **b**. lin$\perp$lin configuration. The laser field is formed by two linearly polarized, counter-propagating beams with orthogonal polarization planes.

it feels an electromagnetic field with rotating polarization that is reminiscent of σ^+ light. This symmetry-breaking effect results in more absorptions of σ^+ photons than σ^- photons. On the other hand, once an atom is in state $|g, +1\rangle$, it likely gets 'stuck' in the cycling transitions, $|g, +1\rangle \Leftrightarrow |e, +1\rangle$ and $|g + 1\rangle \Leftrightarrow |e, +2\rangle$, since these transitions have bigger strengths than the other transition $|g, +1\rangle \Leftrightarrow |e, 0\rangle$. Consequently, the atomic population in state $|g, +1\rangle$ slightly outweighs that in $|g, -1\rangle$, due to the optical pumping effect. These extra atomic population in the magnetic sublevel $|g, +1\rangle$ scatters six-times more σ^+ photons than σ^-. The faster atoms move, the faster the local laser polarization spins, the more population imbalance, and the more photon

scattering imbalance. In a similar way, atoms moving toward the source of the σ^- laser beam may be argued. In summary, atoms experience a viscous force moving in both directions and this force is independent of the Doppler effect and thus is not bound by the Doppler limit given by Equation (1.2). The only intrinsic cooling limit of this cooling mechanism originates from the photon-recoil energy. The lowest temperature reachable with this cooling mechanism is

$$T_{recoil} = \frac{\hbar^2\omega^2}{2mk_Bc^2}, \tag{1.3}$$

where m is the mass of the atom. Note that this cooling mechanism does not require the laser to be specifically detuned. However, in consideration of the classical laser cooling mechanism, red-detuning is still necessary for efficient general laser cooling.

Now we study the other sub-Doppler cooling mechanism with the fiducial atoms of Figure 1.1**b** in polarization gradient field of Figure 1.2**b**, the lin⊥lin configuration. The presence of a near-resonance laser field not only induces atomic transitions, but also causes the atomic levels to shift. The light shifts in the two state that are involved in an electric dipole transition is

$$\Delta E = \pm\frac{\hbar\Omega^2}{4\delta}, \tag{1.4}$$

where '+ (−)' is for the lower (upper) level, δ is the detuning of the laser frequency from the resonance frequency, Ω is the Rabi oscillation frequency. Apparently, with a red-detuned laser field, the lower level shifts down and the upper level shifts up.

According to Reference [70],

$$\Omega = \frac{-eE_0}{\hbar}\langle e|r|g\rangle, \tag{1.5}$$

where E_0 is the amplitude of the electric field that drives this transition, the matrix element $\langle e|r|g\rangle$ is proportional to the Clebsch-Gordan coefficient shown in Figure 1.1. Due to quantum mechanical selection rules, transitions with $\Delta m = -1, 0, +1$ can only be driven by electric fields with polarizations σ^-, linear, and σ^+, respectively. Therefore for multilevel atoms with different magnetic sublevels, E_0 should be understood as the amplitude of the component electric field with the corresponding polarization. For multilevel atoms, if there are multiple transitions associated with a single level, then the total shift in the energy level is the sum of all the transitions. For example, for the magnetic sublevel $|g, +1/2\rangle$, the total light-shift is

$$\Delta E = \Delta E_{-1/2} + \Delta E_{1/2} + \Delta E_{3/2}, \tag{1.6}$$

where $\Delta E_{-1/2}$, ΔE, and ΔE are the light-shifts caused by the transitions $|g, 1/2\rangle \Leftrightarrow |e, -1/2\rangle$, $|g, 1/2\rangle \Leftrightarrow |e, 1/2\rangle$, and $|g, 1/2\rangle \Leftrightarrow |e, 3/2\rangle$ driven by the corresponding constituent laser fields with polarizations σ^-, linear, and σ^+, respectively.

As shown in Figure 1.2**b**, the local polarization varies between linear and circular on the scale of $\lambda/4$. Although the total laser intensity is uniform along the axis, for the magnetic sub-state $|g, 1/2\rangle$, the total light-shift varies on the scale of $\lambda/4$, in the same pattern as the polarization gradient. As a result,

the energy level of the magnetic sub-state $|g, 1/2\rangle$ becomes rugged—hills and valleys of size $\lambda/4$ form along the standing-wave direction. In a similar way, the energy levels of the magnetic sub-state $|g, 1/2\rangle$ is modulated. The two have opposite signs—where it is a hill for one, it is a valley for the other.

For atoms with zero speed, the steady-state atomic population is always distributed in favor of energy valley. Therefore the population difference between $|g, 1/2\rangle$ and $|g, -1/2\rangle$ varies sinusoidally, according to the hill-valley pattern. For an atom that moves, it has to climb a hill in either direction. However, as it climbs the hill, the optical pumping effect redistribute the populations among the magnetic sub-states to renewed equilibrium with the local polarization. Therefore, as the atom continues moving on, it has to climb out the valley it has just dug. This is analogous to a heavy wheel rolling on a sandy seashore. Note that though this cooling mechanism requires the laser beam to be red-detuned, the cooling effect is not affected either by the line width of any absorption peak, or by the Doppler effect. In fact, this cooling mechanism can result in the same temperature limit given by Equation (1.3).

1.2 Trapping and storing of atoms

To make cooling results sustainable in experiment, we need a way of storing atoms. There are quite a few types of storage techniques, including various kinds of magnetic traps, magneto-optical traps, and optical dipole traps.

Magnetic trapping relies on static magnetic field to confine atoms with

permanent magnetic dipole moments. Since the amplitude maximum in the magnetic field is forbidden, the center of a magnetic trap lies in a field minimum. Adiabatic following assumption states that an atom's magnetic moment can usually follow the changing magnetic field. But this assumption can be violated with extremely abrupt changes in magnetic field, such as a sign-flipping, where Majorana losses will occurs [66]. Optical dipole traps rely solely on the interaction between photons and atomic dipoles to provide confinement. Because of parity symmetry, neutral atoms have zero permanent dipole moment. Instead, an oscillating dipole moment is induced in an atom by the applied light field which, in turn, interacts with the light field. Magneto-optical trap (MOT) is a hybrid type of magnetic and optical traps. It combines cooling and trapping in a single step and proves the most robust and commonly used trap so far. We will talk more about all three types of traps next.

1.2.1 Magnetic traps

Magnetically trapped neutral atoms were first observed in 1985 [73]. The biggest advantage of a magnetic trap is that it provides the best isolation for ultracold atoms from any interaction with photons and material (chamber wall *etc.*), leaving only collisions from background gas. Since its first successful demonstration, magnetic traps have found applications in high-resolution precision spectroscopy, collision studies, Bose-Einstein condensation, and atom optics. We study a type of magnetic trap constructed with sophisticated controls of trapping frequencies and ease of optical access—the Ioffe-Pritchard

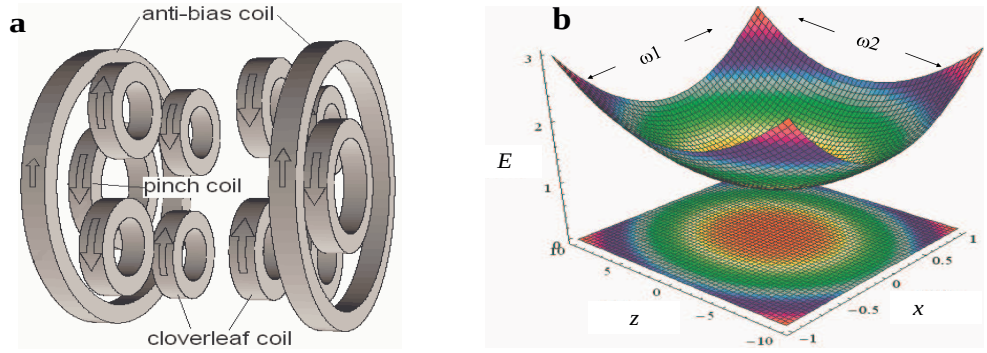

Figure 1.3: **a**. Magnetic coils for a Ioffe-Pritchard-type trap. **b**. Magnetic trapping potential of a Ioffe-Pritchard trap in the x-z plane.

trap (see Figure 1.3**a**).

When an atom with a magnetic dipole moment is in an external magnetic field, an extra term will appear in its Hamiltonian,

$$\begin{aligned} V &= -\vec{\mu} \cdot \vec{B} \\ &= -g\mu_B |\vec{B}| m_F, \end{aligned} \tag{1.7}$$

where $\vec{\mu}$ is the atomic magnetic moment, and $\vec{B}$ is the magnetic field, we have chosen the quantization axis to be along the $\vec{B}$ direction and m_F is the quantum number. With adiabatic following assumption, the quantum number m_F remains unchanged as the atom moves in the magnetic field and then the energy at any position is directly proportional to the absolute value of the local magnetic field. The magnetic field produced by Ioffe-Pritchard trap is

[53]

$$\vec{B} = B_0 \begin{bmatrix} 0 \\ 0 \\ 1 \end{bmatrix} + B' \begin{bmatrix} x \\ -y \\ 0 \end{bmatrix} + \frac{B''}{2} \begin{bmatrix} -zx \\ -zy \\ z^2 - (x^2+y^2)/2 \end{bmatrix}, \tag{1.8}$$

where x, y are the radial coordinates and z is the axial coordinate. Therefore the trapping potential can be obtained as

$$V = -g\mu_B m_F \sqrt{{B_0}^2 + \left(B'^2 - B_0 B''/2\right)(x^2+y^2) + B_0 B'' z^2}. \tag{1.9}$$

From Equation (1.9), it is clear that magnetic sublevels with negative m_F's are weak-field-seekers and thus trappable. The trapping potential in the $x-z$ plane is plotted in Figure 1.3**b**. The trapping frequency along the axial direction is

$$\omega_1 = \sqrt{\frac{g\mu_B m_F B''}{m}}, \tag{1.10}$$

where m is the atomic mass. The trapping frequency in the radial directions is given by

$$\omega_2 = \sqrt{\frac{g\mu_B m_F}{m}\left(\frac{B'^2}{B_0} - \frac{B''}{2}\right)}. \tag{1.11}$$

1.2.2 Optical dipole trap

As we discussed in Section 1.1.1, near-resonance oscillating electromagnetic fields not only cause atomic transitions, but also light shifts in the related atomic levels (Equation (1.4)). It is these light shifts that make optical dipole traps possible [19, 39]. For simplicity, we study the interaction between a strongly focused Gaussian beam and a two-level atom. The laser intensity of a Gaussian beam is given by

$$I(\rho, z) = I_0 \left(\frac{w_0}{w(z)}\right)^2 e^{-\frac{2\rho^2}{w(z)^2}}, \tag{1.12}$$

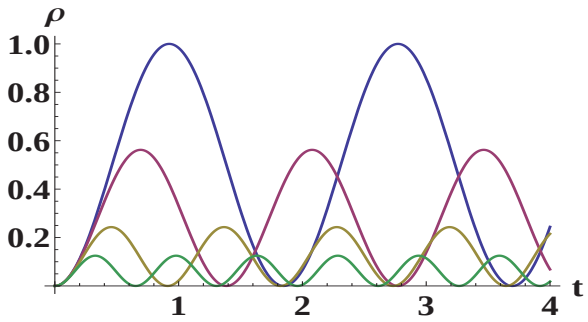

Figure 1.4: Rabi oscillations as these occur in 2-level atom driven by coherent laser field with detunings 0 (blue), 3γ (purple), 6γ (yellow), and 9γ (green), where γ is the absorption peak width. The average population in the excited state is proportional to δ^{-2}, as $\delta \to \infty$.

where $\rho = \sqrt{x^2 + y^2}$, w_0 is the beam waist, $I_0 = 2P/\pi {w_0}^2$, P is the total power in the laser beam, and

$$w(z) = w_0 \sqrt{1 + z^2/{z_R}^2}, \tag{1.13}$$

where $z_R = \pi {w_0}^2/\lambda$ is the Rayleigh range.

Recall the light shifts in atomic energy levels as given by Equation (1.4), when interacting with a Gaussian beam, atoms experience a dipole force,

$$F \simeq \pm \frac{\hbar}{4\delta} \nabla \left[\Omega^2(\vec{r})\right], \tag{1.14}$$

where '+ (−)' is for populations in the lower (upper) level and $\vec{r} \equiv (\vec{\rho}, z) \equiv (x, y, z)$. Depending on whether it is in the ground or excited state, an atom may be attracted to or repelled from the center of the beam focus under the influence of this dipole force. Furthermore, along the Gaussian beam axis, atoms experience a radiation pressure due to the travelling-wave nature of the laser

beam and may stay untrapped. During a period of the Rabi oscillation, the fraction of time that an atom spends in the excited state is $\propto \delta^{-2}$ (see Figure 1.4). On average, atoms experience an attractive force toward the center of the beam waist if they spend most of the time in the ground state. The radiation pressure is also $\propto \delta^{-2}$, however the dipole force is $\propto \delta^{-1}$. Therefore, with sufficiently large detuning $|\delta|$, both the radiation pressure and the repellent force to the excited-state population decrease faster than the attractive force on ground state population. Beyond some threshold the attractive force dominates. In the so-called far-off-resonance trap (FORT), an optical dipole trap produces three-dimensional confinement as well as keeping the atomic population in ground-state. Expanded around the energy minimum, the optical dipole trap may be approximated by harmonic potential:

$$\begin{aligned} V(\rho, z) &= -V_0 \left(1 - \frac{2\rho^2}{{w_0}^2} - \frac{z^2}{{z_R}^2}\right) \\ &= -V_0 + \frac{1}{2} m {\omega_1}^2 \rho^2 + \frac{1}{2} m {\omega_2}^2 z^2. \end{aligned} \tag{1.15}$$

One of the main disadvantages of the red-detuned optical trap is that the minimum of the trap potential lies at the laser intensity maximum. This leads to significant photon-scattering, even with big detuning [35]. A solution is to form a blue-detuned optical "cup" where atoms are confined near the intensity minima and spontaneous emission is thus ameliorated [25]. TEM_{10}-based quasi-1D optical "box" was developed in our group [45, 72], which can provide extremely tight confinement in the transverse directions [71].

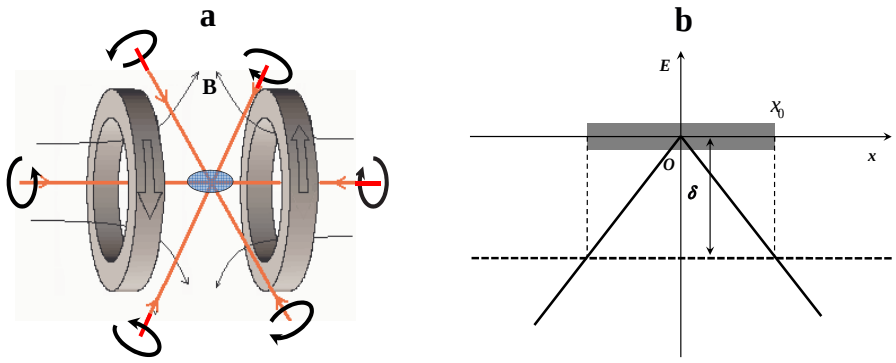

Figure 1.5: **a.** Schematic drawing of a magneto-optical trap. Three orthogonal pairs of counter-propagating laser beams converge to the trap center(shown as red directed lines). All laser beams are red-detuned with respect to the resonance frequency. A pair of anti-Helmholtz coils (shown in gray, the arrows denotes the direction of current) generate magnetic fields (shown as black lines). The laser beams converge onto the point with minimum magnetic field, where atoms are collected and trapped (shown in blue). The laser beams are also used for optical molasses with sub-Doppler cooling mechanism. The six circular lines denote the helicities of the circular polarizations. **b.** The difference of the Zeeman shifts as function of position in a 1D MOT. δ is the laser detuning. Atoms are confined approximately to $[-x_0, x_0]$ (the gray area).

1.2.3 Magneto-optical traps

A MOT is a hybrid trap composed of a static inhomogeneous magnetic field and six laser beams, which contrive to provide a robust trapping potential [83]. Because of the robustness and strong atom-capturing capability, a MOT is frequently used to accumulate cold atoms in the early stage of an ultracold physics experiment. A schematic of a MOT setup is shown in Figure 1.5**a**. In addition to the Doppler cooling effect, the MOT also provides spatial confinement for a certain range of atomic velocities. This is done through a magnetic field gradient generated by anti-Helmholtz coils. On a suitable length scale,

along any direction starting from the trap center, the magnetic field can be approximately expressed as

$$B = B'r, \tag{1.16}$$

where B' is the magnetic gradient along a given direction (a function of the polar and azimuthal angles of that direction), r is the radius. Usually the laser frequency is red-detuned by $\sim$ 15 MHz and B' is along the axis of the anti-Helmholtz coils which is $\sim$ 10 Gauss/cm. A MOT can capture atoms up to 30 m/s. Near the trap center where the magnetic field is about zero, classical and sub-Doppler cooling mechanism works as usual. In pure optical molasses, very slowly moving atoms can keep wandering with little confining force. But in a MOT, cold atoms are confined to a volume which is approximately defined by the equation

$$-\vec{\mu} \cdot \vec{B}(r) = \hbar\delta. \tag{1.17}$$

To summarize, atoms can both be captured and trapped within a MOT.

1.3 Bose-Einstein condensates

The development of cooling and trapping of neutral atoms culminated with the successful achievement of Bose-Einstein condensates (BEC) in dilute gases [3, 15, 26], seventy years later after its first prediction by Satyendra N. Bose and Albert Einstein [13]. BECs provide a research platform for quantum physics on macroscopic scale. BECs become the playground and jurisdiction of many theories in modern physics. See references [47, 81] for more information.

1.4 Atomic Fock states and quantum computing

Quantum computing with trapped ultracold atoms were proposed a decade ago [50]. The earlier efforts in implementing quantum logic with neutral atoms have focused on neutral atoms in optical lattices. However, as we note it, neutral atoms in optical lattices has two disadvantages that hinder further progress. Firstly, there is no individually addressable well-defined qubits in optical lattice. Secondly, there is no effective way of measuring the state of an individual qubit. To overcome these difficulties, some proposals were made to use atomic ensembles as the building blocks of quantum computing [30, 63, 64, 89].

The realization of Bose-Einstein condensation (BEC) in dilute gases has provided a new path toward the production of atomic Fock (or number) states. Fock states refer to the quantum states with definite particle numbers. Trapped ultracold atoms in the ground-state of an optical trap has many attractive characteristics for quantum computing: individual addressability, easy manipulation, superior scalability [4, 31, 50]. Recent experimental work has demonstrated all the necessary steps toward the realization of atomic Fock states with ultracold bosonic atoms [21].

1.5 The DiVincenzo criteria for quantum computing

The necessary characteristics for any quantum computing candidates, the so-called DiVincenzo criteria, have been outlined [29]. The DiVincenzo criteria states that for a system to be a candidate for an implementation of

quantum computation, it should

1. be a scalable physical system with well-defined qubits,
2. be initializable to a simple fiducial state such as $|000\ldots\rangle$,
3. have decoherence times much longer than gate operation time,
4. have a universal set of quantum gates;
5. permit high quantum efficiency, qubit-specific measurements;

Additionally, for the system to be compatible with requirements of quantum information and communication, it should

6. readily convert quantum information between stationary and flying qubits;
7. transmit flying qubits between different locations with high fidelity.

Table 1.1 gives the latest status of several promising physical systems as the building blocks of quantum computing, including that of neutral atoms in optical lattices [67].

1.6 Interacting many-boson systems and the Bethe ansatz method

Ultracold bosonic atoms have become the starting point for many modern physics researches. Experimental and theoretical studies have been carried out toward the production of Fock states with trapped sodium atoms

Table 1.1: The Mid-Level Quantum Computation Roadmap: Promise Criteria.

QC Approach	Quantum Computation					QC Networkability	
	#1	#2	#3	#4	#5	#6	#7
NMR							
Trapped Ion							
Neutral Atom							
Cavity QED							
Optical							
Solid State							
Superconducting							
Unique Qubits	This field is so diverse that it is not feasible to label the criteria with "Promise" symbols.						

Legend:

= a potentially viable approach has achieved sufficient proof of principle

= a potentially viable approach has been proposed, but there has not been sufficient proof of principle

= no viable approach is known

(Data taken from "Quantum Computation Roadmap", last updated in April 2004, `http://qist.lanl.gov/pdfs/rm_intro.pdf`)

[21, 27, 32, 82]. However, interacting many-boson systems pose a computationally hard problem. Previous theoretical work is either carried out with special cases with infinitely strong interaction, or unnaturally divided the interaction into a few regimes and used different calculation methods in different regimes.

The interaction strength between atoms is another control parameter in addition to the trap size and trap depth. Atomic interaction strength can be tuned by Feshbach resonances or by adjusting the transverse confinement of the optical trap [49, 72]. Though strong repulsion between atoms are desirable for the production of Fock states, what can be experimentally realized is the regime of relatively but not infinitely strong interactions. As a result, calculations made in the Tonks-Girardeau regime may only provide very inaccurate guide for experiment [37]. In order to provide more accurate calculations for the production of bosonic Fock states, we use the Bethe ansatz to calculate the single-particle energies of a group of interacting atoms with interaction strength as one of the scalable parameters.

1.7 Organization of the dissertation

In Chapter 2, we consider optically trapped ultracold fermionic atoms (exemplified by ^{6}Li atoms) as the basics for quantum logic and provide theoretical insights on the advantages. We simulate the production of fermion Fock states with the aim to implementing practical quantum logic. We focus on the most practical aspects of quantum computation: the fidelities of initialization, gate operation and state-detection. We produce atom Fock states

step by step, and in each step, we ensure certain predefined fidelity so that overall we can have ultra-high fidelity in any quantum operation and qubit state detection. With an array of fermionic atoms in Fock states as the starting point of quantum logic, we strive to fulfill the DiVincenzo criteria for quantum computation.

In Chapter 3, we discuss the application of the Bethe ansatz to calculate the single-particle energies in many-boson systems confined in one-dimensional square-wells and the production of Fock states in bosonic atoms, such as sodium atoms (^{23}Na).

The works discussed in this dissertation are published in [84] and [91].

Chapter 2

Quantum Computing with Ultracold Fermionic Atoms in Optical Traps

The potential impact of quantum computing has stimulated a world-wide effort to develop the necessary experimental and theoretical resources [12, 18, 40, 42, 51, 54, 57, 75, 97]. A status report of a few proposed quantum computing schemes are listed in Table 1.1. In this chapter, we develop an quantum computing approach based on ultracold fermionic atoms in optical traps that have the potential for large-scale quantum computations.

One of the key questions is that of fidelity of the atomic Fock states, and in that regard bosons are not ideal because they rely on strong interactions to maintain a relatively large excitation gap, and to suppress low-frequency excitations during the culling process. This leads us to propose instead fermionic atoms where a precise number would be rigorously enforced by the Pauli exclusion principle which states that "No two identical fermionic particles may exist the same quantum state at any moment". Calculations of eigen-energies and wavefunctions of non-interacting fermionic atoms are thus straightforward. We show that laser-culling of fermionic atoms in optical traps can produce a scalable number of ultra-high fidelity Fock-state qubits. We show how each

qubit can be independently prepared, how to perform the required entanglement operations, and how to measure the qubit state with spatially-resolved, single-atom detection.

More specifically, we exemplify our simulations using ^{6}Li atoms. ^{6}Li has the advantage that the interaction strength and sign (attractive or repulsive) can be tuned with an external magnetic field. Two magnetic sublevels of one hyperfine ground state, $\left|F = \frac{1}{2}, m_F = \frac{1}{2}\right\rangle$ and $\left|F = \frac{1}{2}, m_F = -\frac{1}{2}\right\rangle$ are used to define a qubit. We denote these states as $|\uparrow\rangle$ and $|\downarrow\rangle$ respectively. Under low magnetic field condition, the atom in spin state $|\downarrow\rangle$ is a low-field-seeker while the atom in spin state $|\uparrow\rangle$ is a high-field-seeker. At large magnetic field, both of these states become high-field seekers with a well-defined frequency splitting that is nearly field-independent [35].

2.1 Preparation of fermionic Fock states

The starting point of the "on demand" single atom preparation is optically trapped ultracold ^{6}Li atoms with equal populations in two spin states [1, 78]. The atoms can be cooled by evaporation at a magnetic field around 300 Gauss, where the scattering length $a_s \approx -300a_0$ (a_0 is the Bohr radius) [65]. a_s is large enough for efficient evaporation of the spin mixture, and is at a minimum as a function of magnetic field. After evaporative cooling, a weakly interacting degenerate Fermi gas forms at temperature $T \ll T_F$, where T_F is the Fermi temperature. The single atom preparation process can be split into three steps (see Figure 2.1):

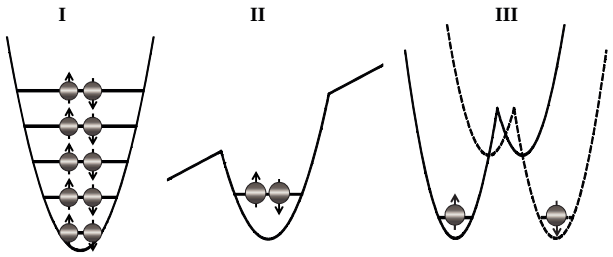

Figure 2.1: Steps used in producing ultra-high-fidelity qubits. **I**. A degenerate Fermi gas, produced by evaporative cooling, whose interaction strength is tuned to zero ($B \approx 0$). **II**. Adiabatic laser-culling removes all of the atoms except a pair of atoms in the ground state of the trap which have opposite spins, following the Pauli exclusion principle. Due to the applied magnetic field gradient, the two spin states experience different potentials. Only the potential for the $|\uparrow\rangle$ state is shown. **III**. An adiabatic trap-splitting separates the pair into two adjacent micro-traps. Potentials for both spin states are shown (solid and dashed).

Step I The magnetic field is tuned to near ~ 0 Gauss from the initial field of 300 Gauss, resulting in a non-interacting degenerate Fermi gas (DFG). In this state, a spin pair fills each level, up to the Fermi level.

Step II Atom pairs are ejected by laser-culling. This is accomplished by adiabatic lowering of the optical potential. This prepares a single pair in the ground state.

Step III The well is adiabatically split into two parts that are spatially separated. In the presence of a magnetic field bias this prepares one spin state on the left and the other on the right. Each atom can then serve as the initial state for a qubit.

Step IV The trap wall is adiabatically raised to a higher level to preserve the

resultant qubit states.

There are two important non-trivial steps in the Fock state preparation, *i.e.*, the laser-culling and the trap-splitting. Next we explain the simulation models we used for the analysis of these two steps in Section 2.2 and then, in Section 2.3, we show how ultra-high fidelity is enforced at each step.

2.2 Simulation models

We will explain the simulation models that are used in preparing the ultracold atomic fermionic qubits. For the rest of this chapter, we adopt the following units: the unit of energy is $\hbar\omega$, the unit of length is $x_0 \equiv \sqrt{\frac{\hbar}{m\omega}}$, and the unit of force is $\hbar\omega/x_0$.

2.2.1 Laser-culling

The laser-culling technique was first studied in Reference [32] for producing Fock states in strongly interacting bosonic atoms. Here we go over the simulation models used for analyzing the fidelities in preparing Fock states in optically trapped fermionic atoms. The Bethe ansatz calculation method for generating bosonic atomic Fock states using laser-culling will be presented in Chapter 3.

A harmonic trapping potential is the most common approximation for an optical trap. Naturally, a truncated harmonic trap becomes the convenient model in the discussion of laser-culling (see Figure 2.2**a**). In this chapter, we

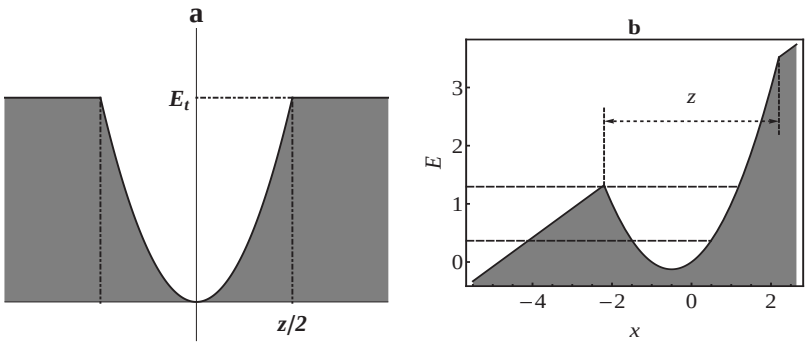

Figure 2.2: The trapping potentials used in the simulations. **a**. Truncated harmonic trap. The truncation energy E_t and truncated trap size (or simply trap size) z_t are shown. **b**. Truncated harmonic trap with a positive magnetic gradient. The trap size, z, is defined as the length of the parabolic part in the potential profile. Dashed lines denote the level of the ground and first-excited state.

consider the 1D case only. The arguments can be easily generalized to 3D.

For the calculation of states whose energy levels are deeply bound in a truncated harmonic trap, the Wentzel-Kramers-Brillouin (WKB) method provides a good approximation. The details of using this method to calculate the energy levels and wavefunctions of fermionic atoms in a 1D optical trap is described Appendix C. But the result of the WKB calculation is surprisingly simple—the energy levels and wavefunctions are exactly the same as those in a harmonic trap with the same trapping frequency.

However, as pointed out in the Appendix, WKB method has its limitation—a sufficient spatial gap is required between the turning point $z/2$ of the state of interest and the truncation point $z_t/2$. Equivalently, there must be a sufficient energy gap between the energy level and the truncation energy (see

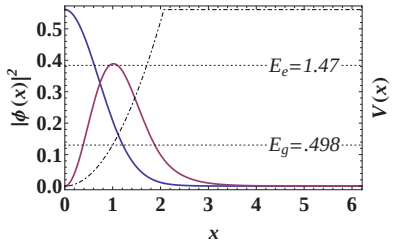

Figure 2.3: Exact numerical calculation for truncated harmonic trap with trap size $z = 4.14$. Dashed lines denote the eigen-energy level of the ground and first-excited state. The trapping potential of the truncated harmonic trap is depicted (dot-dashed). The unit of energy is $\hbar\omega$ and energy reference is set at the bottom of the trap.

Figure 2.2). Since we are primarily interested in the ground state during a laser-culling process, WKB method is useful only for $E_t \gg \hbar\omega$.

A direct numerical calculation is possible, in which the wavefunction in the trap area is expressed as parabolic cylinder function, while that outside is exponential function. By specifying the wavefunction is continuous and have continuous derivatives at the the boundaries, we can get numerical eigen-energies and wavefunctions for the ground state and first excited state (see Figure 2.3).

A comparison between the WKB method and the exact numerical method sheds light on the validity range of the WKB approximation. As shown in Figure 2.4, the WKB approximation remains valid until the trap size decreases to $z \approx 4.0$.

As outlined in Section 2.1, we need a constant force (or a tilt in the trapping potential), f, to split the atoms apart in **Step III**. But as will become

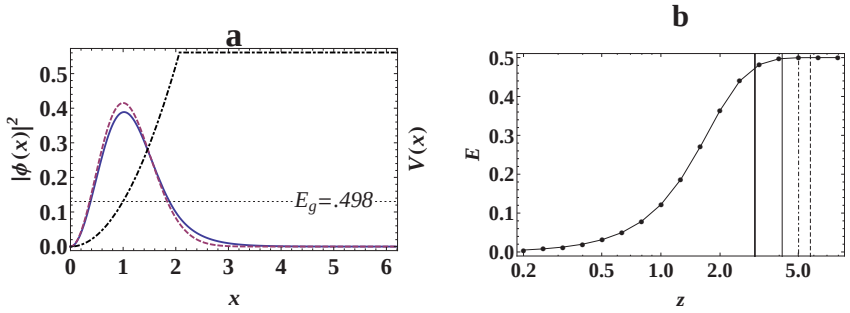

Figure 2.4: Comparison between exact numerical calculations and WKB approximation. **a**. Ground-state wavefunction comparison at fixed trap size $z = 4.14$. The left vertical axis is the probability density; the right axis depicts the trapping potential (dot-dashed) and energy level. The ground state wavefunctions of the direct numerical calculation (solid) is compared with that obtained with the WKB method (dashed). **b**. Ground-state eigen-energy as a function of the truncation size z. The vertical lines show the ionization thresholds for atoms in the first (solid thick), second (solid thin), third (dot-dashed), and fourth (dashed) excited states.

clear in the fidelity analysis of the final qubit preparation (Section 2.3), a force is already necessary during the laser-culling process of **Step II**. We can provide this force by applying a magnetic field gradient along the axis of the 1D optical trap. The purpose of f is to sweep the atoms away from the micro-traps as soon as they are ionized. For simplicity, we assume the force has a positive sign for the $|\uparrow\rangle$ state.

To accurately predict the fidelity in the laser-culling process of fermionic atoms, we need to develop a more general solution which incorporate a slope in the trapping potential and remain valid throughout the laser-culling process. In our next simulation, we approximate the optical trap and the magnetic gradient with a tilted, truncated harmonic trap (see Figure 2.2**b**). The tilted,

truncated harmonic trap is specified by the trap size (or truncation size) z and the force (or potential gradient) f. After reaching a minimum trap size, the trap is held constant for a certain time to allow ionized atoms to escape, while maintaining a high occupation probability of the ground-state. The trap size, force, and holding time are optimized for best fidelity.

Because of the tilt, the trap has no stationary bound state, only quasi-bound states. In the limit $z \to \infty$, these quasi-bound states become the bound states. The lifetimes of the quasi-bound states determine the rate of the change of trap occupation probability. The optimized final trap depth, tilt, and holding time is estimated with the following scattering model [28].

Suppose a stream of incoming atoms is incident from $x = -\infty$, with energy E, scattered by the trap potential. We assume the trap is located at $[-z/2, z/2]$. Let $\psi_E(x)$ be the wavefunction of the stationary state of the incoming atoms. Outside the trap ($x < -z/2$),

$$\cos(b)\,\mathrm{Ai}(\chi) + \sin(b)\,\mathrm{Bi}(\chi), \tag{2.1}$$

where $\chi = \sqrt[3]{2f}\left(x - \frac{-z^2+2E}{2f}\right)$, and b is an unknown parameter. Inside the trap,

$$\psi_E(x) = a(E)\, e^{-x^2/2} H_\nu(x), \tag{2.2}$$

where $H_\nu(x)$ is the Hermite function of degree ν, $a(E)$ is the amplitude [58]. We require that $\psi_E(x)$ be continuous and differentiable for all x. Boundary conditions are thus established, from which $a(E)$ can be obtained. Of special interest to us are those states that have significant amplitude in the trap area,

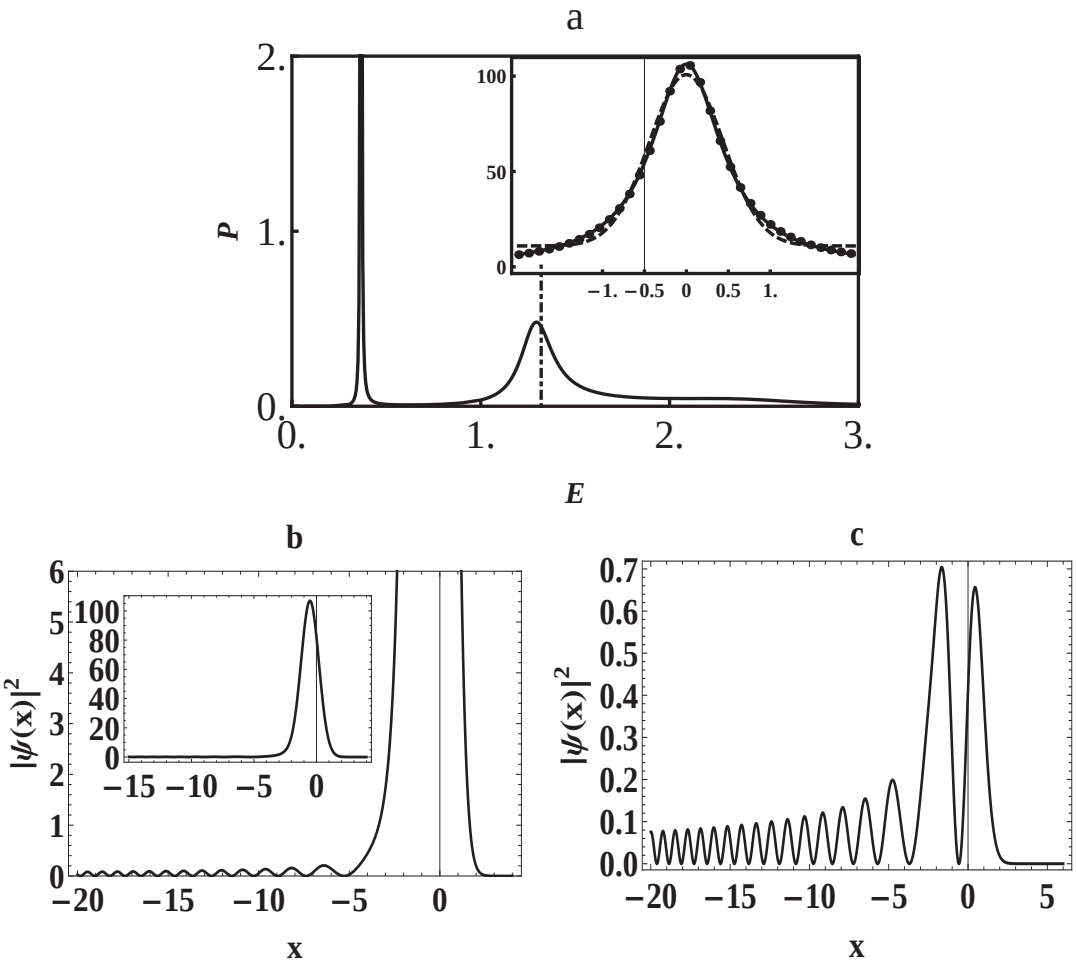

Figure 2.5: Laser-culling simulation model. Parameters used in the simulation: the trap size is $4.4x_0$, the magnetic force is $0.5\hbar\omega/x_0$. **a** Density of states (DOS). The vertical dotdashed line denotes the barrier height of the trap. Inset: Lorentzian (solid) and Gaussian (dashed) regressions of the resonance peak at $E \approx 0.365$ and the unit of the horizontal axis is this peak's FWHM. **b** Stationary wavefunction at $E \approx 0.365$. Inset shows the panorama of the wavefunction. **c** Stationary wavefunction at $E \approx 1.29$.

because they correspond to the quasi-bound states of the trap. For simplicity, we can take $P(E) \equiv |a(E)|^2$ as a measure of the density-of-states of the trap. For $z = 2.2$, $f = 0.5$, we find two conspicuous peaks at $E \approx 0.366$ and 1.29 in the DOS vs E plot (see Figure 2.5**a**). The wavefunctions of the stationary states at these two energies are also shown in panel **b** and **c** of the same figure. Note that in the limit of zero magnetic force, the resonance peaks at these two energies correspond to the ground and first-excited states of the truncated harmonic trap, respectively.

$P(E)$ describes not only the ionization thresholds, but also the dynamical properties of the quasi-bound states. To see that, we study the evolution of a wavefunction $\phi(x,t)$. Imagine that at time $t = 0$, we have

$$\phi(x,0) = \begin{cases} c\,\psi_{E_0}(x), & -z/2 < x < z/2; \\ 0, & \text{otherwise}, \end{cases} \tag{2.3}$$

where E_0 is one of the resonance energies, c is a normalization factor such that $\int_{-\infty}^{\infty} |\phi(x,0)|^2 dx = 1$ and there is no other atom source. Subsequently, the atom will start to tunnel out of the trap. The probability, $R_{E_0}(t)$, for an atom to remain in the trap is given by

$$R_{E_0}(t) = \int_{-z/2}^{z/2} dx\, |\phi(x,t)|^2. \tag{2.4}$$

To make further progress, we make two approximations. Firstly, in the vicinity of a resonance peak at $E = E_0$, one can write the stationary wavefunction at energy E as

$$\psi_E(x) \approx C(E) a(E) \psi_{E_0}(x), \tag{2.5}$$

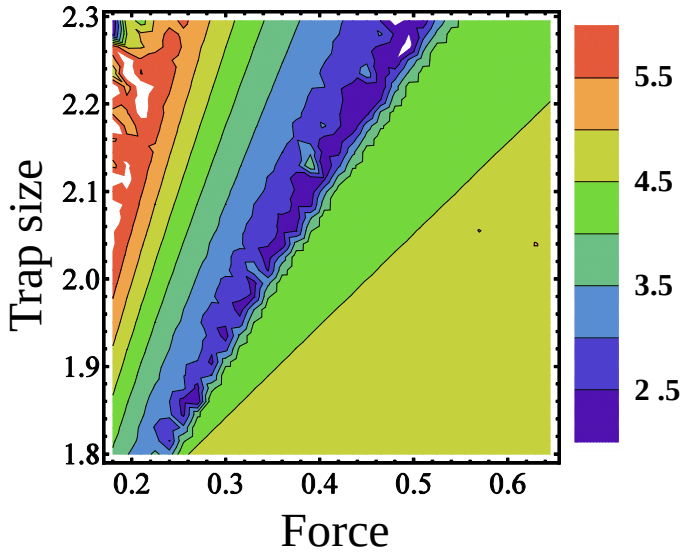

Figure 2.6: Peak width (FWHM) ratio of the excited state to the ground state (in base-10 logarithmic scale) as function of the trap size and magnetic gradient, in the laser-culling process. The white color represents out-of-range color, *i.e.*, should be colored more than its surrounding.

where $C(E)$ is a slowly varying quantity. Secondly, due to the oscillatory nature of Airy functions, the main contribution to the inner product of two wavefunctions comes from the integral over the trap region, or,

$$\int_{-\infty}^{\infty} dx \psi_E^*(x)\psi_{E_0}(x) \approx \int_{-z/2}^{z/2} dx \psi_E^*(x)\psi_{E_0}(x) \tag{2.6}$$

for $E \neq E_0$.

Now we can evaluate $R_{E_0}(t)$ by expanding $\phi(x,t)$ in terms of the wavefunctions of the stationary states, $\psi_E(x)$. We find

$$R_{E_0}(t) \approx |C(E_0)|^2 \left| \int_{E_0-\epsilon/2}^{E_0+\epsilon/2} a(E) e^{iEt} dE \right|^2 , \tag{2.7}$$

where ϵ is the range of integration. In the vicinity of a resonance peak, the function $P(E)$ is essentially Lorentzian (see the inset of Figure 2.5**a**), and we finally obtain

$$R_{E_0}(t) \approx e^{-\gamma_{E_0} t}, \tag{2.8}$$

where γ_{E_0} is the full width at half maximum (FWHM) of the resonance peak at $E = E_0$. The lifetime of the quasi-bound state at $E = E_0$ is $\tau_{E_0} = \gamma_{E_0}^{-1}$. Eq.(2.8) is used to determine an optimized combination of minimum trap depth, magnetic force, and holding time for the best fidelity. It is also worth noting that ultimately the *difference* in the lifetimes between the ground and the first excited quasi-bound states determines the fidelity of producing a pair of atoms in the ground state of the trap. In Figure 2.6, we plot the peak width (FWHM) ratio between the resonance peaks corresponding to the first excited and the ground quasi-bound states.

Of course, when the width of the resonance peak is big enough, the shape of the peak will deviate from Lorentzian. Then the decay of the quasi-bound state due to tunnelling would become non-exponential (see Reference [93] for more details). But this non-exponential decay does not affect the precision of our simulation.

2.2.2 Adiabatic trap-splitting

A double-well potential with a bias (voltage in solid-state physics) potential is a very commonly used model to study transport problems. In **Step II** of the process of producing qubits for quantum computing, we use this

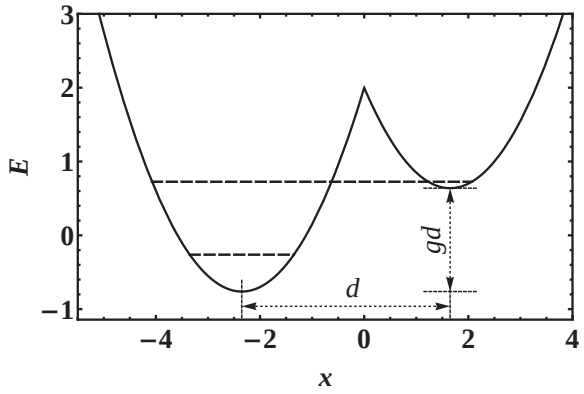

Figure 2.7: Simulation model of separating a pair of atoms in opposite spin states. The parameters shown in this figure are d, the distance between the energy minima (in unit of x_0), and g, the force produced by the applied magnetic field gradient (in unit of $\hbar\omega/x_0$). Dashed lines show the energy levels of the ground and first excited state, obtained numerically. The excitation gap is defined as the energy difference between the two levels.

model to study the adiabatic trap splitting. For simplicity, we adopt a simpler potential than that of a realistic optical tweezer. The double-well potential is composed of two spliced parabolic sections. Each parabolic section has an energy minimum and each has the same trapping frequency (see Figure 2.7). Such a double-well potential has an infinitely sharp, unrealistic 'tip' on the barrier separating the two wells. But this should not affect the order of magnitude in our estimation. The bias potential is produced by applying an appropriate magnetic field gradient. Since $|\downarrow\rangle$ is a low-field-seeker and $|\uparrow\rangle$ is a high-field-seeker at low magnetic field, each atom is displaced to a different location as soon as the trap is split.

We assume the splitting is performed adiabatically. We calculate the

energy levels and probability distribution at various splitting parameters (displacement and force). A sufficient energy gap between the ground state and the first-excited state, or the *excitation gap*, (see Figure 2.7) must be maintained throughout the trap-splitting process in order to suppress transitions from the ground state. In Figure 2.8, we plot the excitation gap as function of the splitting parameters g and d. As shown in this figure, the best we can do is to always remain in regions where the gap is close to $\hbar\omega$. This can generally be fulfilled by applying a magnetic field gradient at the beginning of the trap-splitting such that a force of 0.7 is maintained throughout the splitting process. For $\omega = 2\pi \times 1$ kHz and magnetic field gradient of about 2.3 Gauss/cm, the excitation gap is about 48 nano-Kelvin (see Figure 2.8).

2.3 Fidelity of preparing fermionic atoms in ground Fock states

We now show in detail how ultra-high fidelity is enforced at each step of the preparation of fermionic Fock states.

Step I In the presence of a scattering length $a_s \approx -300a_0$ between the $|\uparrow\rangle$ and $|\downarrow\rangle$ states, the Fermi gas is weakly interacting. At $T = 0$, the Fermi gas may form a BCS state. The pairing gap for such a state can be estimated through $\Delta \approx 0.5E_F \exp(\pi/2k_F a)$ [36]. For a degenerate ^{6}Li gas with $k_F^{-1} \sim 1000a_0$, the pairing gap $\Delta \approx 0.002E_F$. With such a small Δ, the occupation probability of the lowest energy state (*e.g.* the $\mathbf{k} = \mathbf{0}$ state for a uniform gas) $n_{\mathbf{k}=\mathbf{0}} = (1 - \eta_{\mathbf{k}}/\epsilon_{\mathbf{k}})/2 \approx 1 - 4 \times 10^{-6}$, where $\eta_{\mathbf{k}} = \varepsilon_{\mathbf{k}} - E_F$, $\varepsilon_{\mathbf{k}} = \hbar^2 k^2/2m$, $\epsilon_{\mathbf{k}} =$

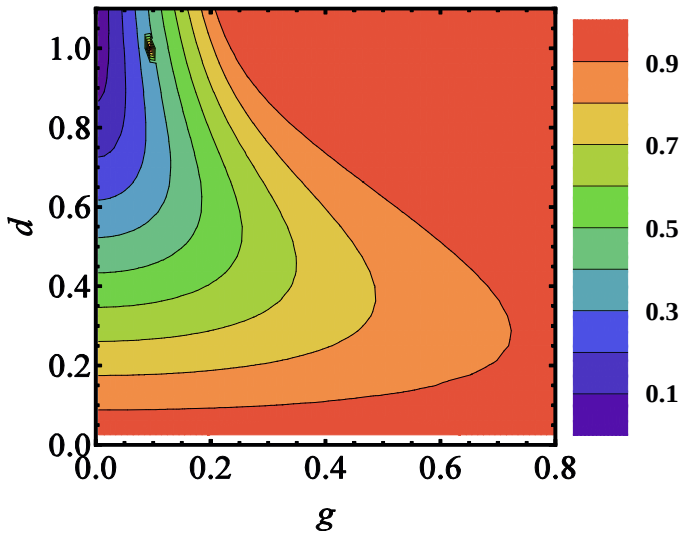

Figure 2.8: Excitation gap (in unit of $\hbar\omega$) during adiabatic trap-splitting for separating a pair of ultracold ^{6}Li atoms. Red (blue) color represents large (small) excitation gap. The horizontal axis is the magnetic force g and the vertical axis is the distance d.

$(\Delta^2 + \eta_{\mathbf{k}}^2)^{1/2}$ is the quasi-particle excitation energy, and we take the chemical potential $\mu \approx E_F$ for the BCS state. In addition, for such a small pairing gap, finite temperature effects dominate, and there may be even no BCS pairing. However, the finite temperature does not affect the ground state occupation probability. Consider a temperature $T = 0.05T_F$, for which the ground state occupation probability is approximately $1/\left[\exp\left(-E_F/k_BT\right) + 1\right] = 1 - 4 \times 10^{-5}$. Clearly, the probability loss is negligibly small. Therefore a fast sweep of the magnetic field (i.e., the scattering length) to the non-interacting region does not affect the ground state occupation probability or the fidelity of the single atom preparation.

Step II A non-interacting DFG in a deep optical trap serves as the starting point for the laser-culling process. The trap wall is reduced to a level slightly below the ionization threshold of the first-excited state of the optical dipole trap. The trap reduction rate is chosen to fulfill the adiabaticity requirement. To that end, we enforce a constraint: we always maintain a constant trapping frequency, ω, throughout the laser-culling process, which can be accomplished by dynamically varying the focus of the beam [55]. (In practice, this step may not be necessary, but it greatly simplifies the calculation.) According to the WKB method, the non-interacting atoms with energy much lower than the trap depth are largely unaffected by the laser-culling until the trap depth is very close to the energy level of first-excited state. Therefore if we start out with degenerate Fermi gas, we should have essentially unitary fidelity of completely filled ground state. The adiabaticity condition is fulfilled as long as the WKB approximation is maintained valid, which holds until the trap depth is around $3\hbar\omega/2$, where $\hbar \equiv h/2\pi$ and h is Planck's constant. Beyond this point, the trap reduction rate must be slowed down to continue maintaining adiabaticity conditions.

With the simulation model explained in Section 2.2.1, we now estimate the resulting fidelity of the laser-culling process. The goal is to produce exactly one pair of atoms, with spin up and down, respectively, on the ground state of the optical trap. With the help of Pauli exclusion principle, if we got two atoms in the ground state, they are guaranteed to be of spin up and down, respectively. Now let's estimate the fidelity of eliminating all atoms except the

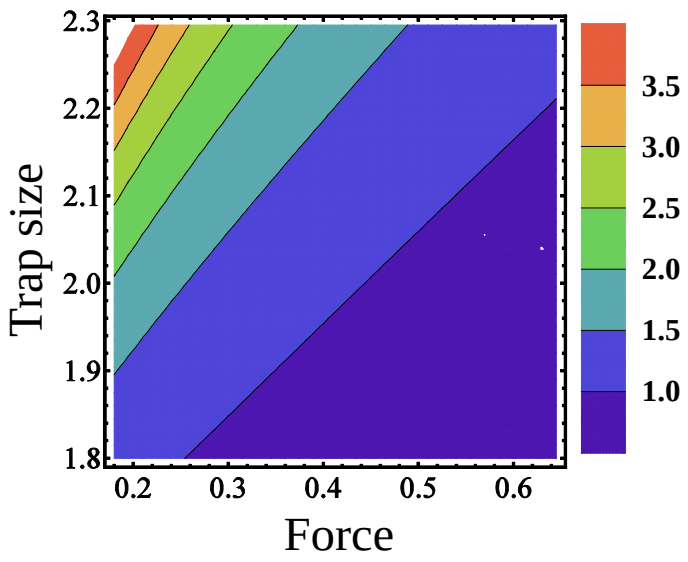

Figure 2.9: Holding time (in unit of $1/\omega$) during the laser-culling process. The scale of the contour plot is in base-10 logarithmic scale. Redder color represents longer holding time.

ground-state ones, assuming unity fidelity from the last step.

Because of the applied magnetic field gradient, all states are quasi-bound states and have finite lifetime. Our task is to let go the extra atoms in the optical trap while keeping the pair of ground state atoms as entirely as possible. There are three parameters at our play: the force f, the culling length z, and the holding time t. By virtue of Equation (2.8), we can estimate the lifetime of each quasi-bound states by obtaining the width (FWHM) of the corresponding resonance peaks. In practice, we choose f and z as the independent variables. For given f and z, we determine the holding time t to be six times the lifetime of the first-excited quasi-bound state. That is, we

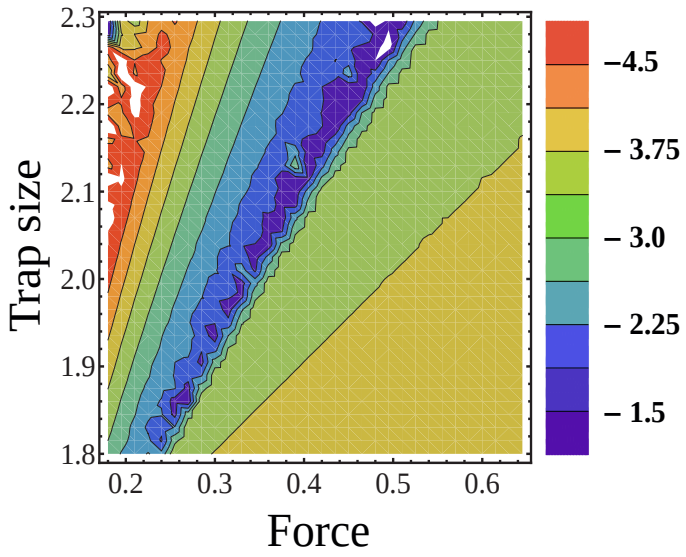

Figure 2.10: Fidelity of laser-culling. Shown is the base-10 logarithm of the ground state fidelity loss. Red (blue) color represents high (low) fidelity. The white areas are out-of-range clippings: near the left-hand side, the white areas should be redder than its surrounding color; near center-top, the white area should be bluer than its surrounding color.

require a residual probability $\leq 10^{-5}$ for any remaining excited atom as the benchmark for any combination of f and z. The necessary holding times are shown in Figure 2.9.

Taking into account all the steps in laser-culling, we show the fidelity of preparing a single pair of atoms in the ground state of a micro-trap in Figure 2.10. For a set of realistic parameters: trapping frequency $\omega = 2\pi \times 1$ kHz, magnetic field gradient 0.66 Gauss/cm, truncated trap size 8.8 μm, the ground-state to first-excited state lifetime ratio is 7.53×10^5. With a holding time 218 ms, we get a residual probability of 10^{-5} for the excited-state and a

ground state occupation probability larger than 0.99998.

Step III Now we should have a pair of ^{6}Li atoms with spin states $|\downarrow\rangle$ and $|\uparrow\rangle$, respectively, in the ground state of an optical trap. What we need to do next is to produce two separate well-defined qubits. We realize this by using a deterministic trap-splitting technique [10, 45]. We impose a suitable positive magnetic field gradient while we adiabatically split the optical tweezer (that holds the pair) into two beams. Under low magnetic field condition, the atom in spin state $|\downarrow\rangle$, a low-field-seeker, is driven to the left while the atom in spin state $|\uparrow\rangle$, a high-field-seeker, is driven to the right. If we do this adiabatically, during and after the splitting the atoms should stay in the ground state and become two well-defined qubits.

Figure 2.11 shows the calculated loss of fidelity of the trap-splitting process, defined as 1 minus the combined probability that the atoms with the right spin states finish in the ground-state of the right traps, according to the scheme outlined above. It shows that this step can be realized at ultra-high fidelity, as a function of the separation displacement d and of the applied magnetic force g. (As a digression, if the two wells are identical, this method creates an entangled spin pair, which will be analyzed in more detail in a later publication.) With a trapping frequency $\omega = 2\pi \times 1$ kHz, a magnetic field gradient of 0.66 Gauss/cm and a separation displacement $d = 6.25$ μm, we find 0.99998 trap-splitting fidelity.

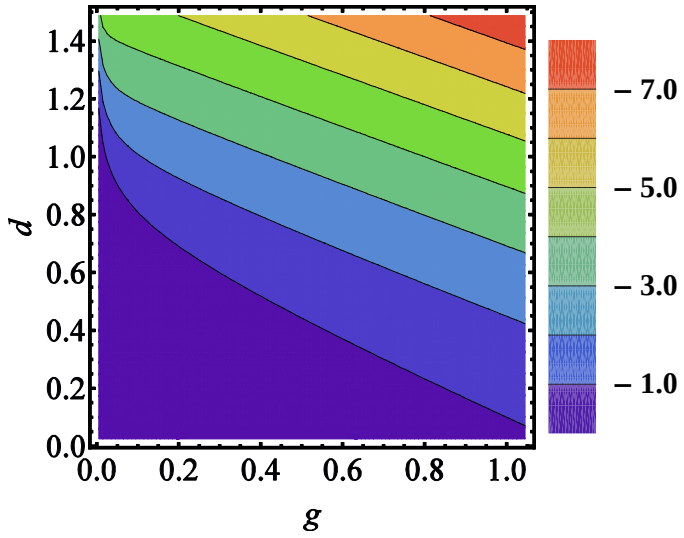

Figure 2.11: Loss of fidelity during trap-splitting. Shown in base-10 logarithmic scale. Red (blue) color represents high (low) fidelity. We assume complete suppression of excitation by maintaining a sufficient energy gap and keeping the process adiabatic. The horizontal axis is the magnetic force g and the vertical axis is the distance d.

2.4 Scalability

So far, we have shown that two fermionic Lithium-6 atoms in the ground states of two adjacent micro-traps can be prepared at ultra-high fidelity. The quantum computing power of this system is manifest only after we scale it up by a factor of ≈ 50.

How can scale this qubit-preparation process to multiple traps, and make the "switchyard" of multiplexed beams to perform the required complex operations while maintaining a relatively high fidelity? This can be done with the scalable microelectromechanical systems (MEMS) technology [56]. Using

this technology, an array of beams can be directed to each site. Alternative approaches have also been developed and proposed in Reference [8, 33, 96]. By steering the beams, we can transport individual atoms and bring them into pairwise interaction with arbitrary control. The geometry that optimizes such an arrangement is an optical donut mode from a blue-detuned beam at 532 nm which would confine the atoms in a long tube [72]. An array of micro-traps would most easily be accomplished with red-detuned beams that create attractive potentials along the axis.

The preparation process is the same as outlined in Section 2.1. With the numbers used for the fidelity analysis of laser-culling and trap-splitting processes, we estimate an overall fidelity of 0.998 to prepare 100 qubits initialized in the antiferromagnetic state

$$\overbrace{|\downarrow,\uparrow,\downarrow,\uparrow,\cdots,\downarrow,\uparrow\rangle}^{100 \text{ qubits}}, \tag{2.9}$$

starting with a degenerate fermi gas of ^{6}Li atoms. To summarize, we can prepare an array of $2N$ micro-traps, each with one atom in the ground state, as illustrated in Figure 2.12.

This technique also enables the creation of a two dimensional optical trap array, and entanglement of any pair using the qubit transfer technique of Reference [10]. This could overcome the limitations of linear case where only nearest-neighbor operations are possible (see artist's concept Figure 2.13).

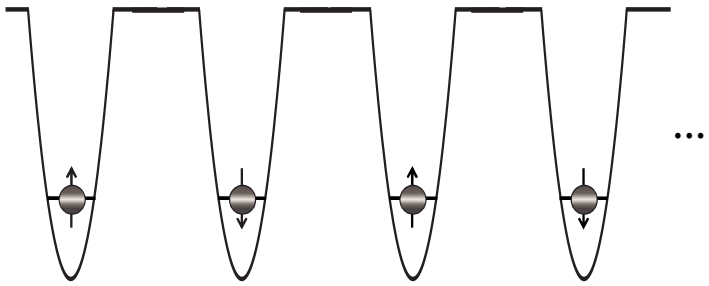

Figure 2.12: Array of $2N$ optical traps. With the scalability of our system, we can prepare a fiducial antiferromagnetic state with $2N$ qubits.

2.5 Entanglement generation and implementation of universal gates

Consider a system that can be subdivided into two or more subsystems. Quantum entanglement refers to the correlated state among the subsystems where the state of one subsystem can not be determined on itself but together with other subsystem(s). This property is not affected whether the subsystems directly interact with each other or however far they are spatially apart from each other. Quantum entanglement has important applications in quantum information theory, quantum computing, quantum cryptography and quantum state teleportation [6, 7, 14].

Let each subsystem in the system has a set of eigen states $|a_i\rangle$. The system state can be expressed as a superposition of the direct products of each subsystem:

$$|\Psi\rangle = C_1 |\alpha_1\rangle |\beta_1\rangle + C_2 |\alpha_2\rangle |\beta_2\rangle + \cdots . \tag{2.10}$$

If the state $|\Psi\rangle$ can be factored, with each factor represents the state

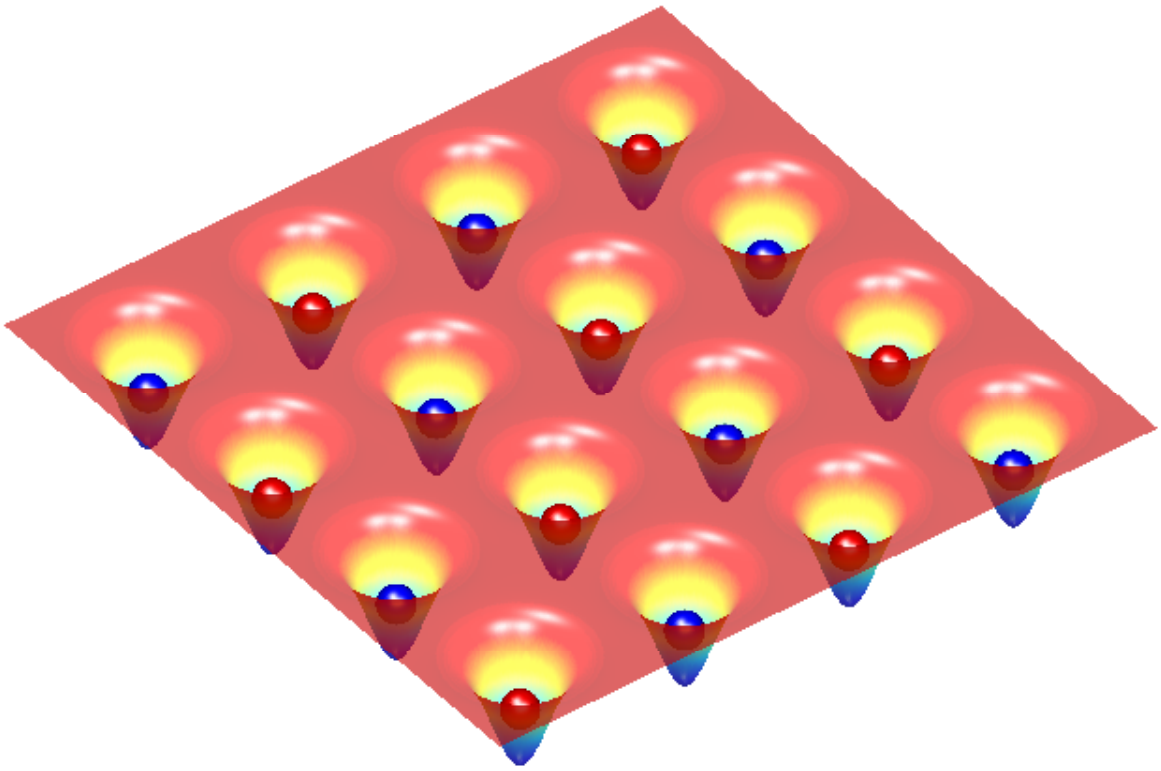

Figure 2.13: Artist's concept of a 4×4 matrix of fermionic, Fock-state qubits, initialized to fiducial antiferromagnetic state with 16 qubits. Red (blue) color in the trapping potential means higher (lower) energy. Atoms are shown as little balls, with blue color meaning spin-up, red-color spin-down. All atoms are in the ground-state of the micro-traps. By moving the containing micro-trap, each atom can be made to engage in a two-qubit gate operation with each other atom by the qubit transport technique [10].

of one subsystem, then the state $|\Psi\rangle$ is an unentangled state, otherwise, an entangled state.

Here we give a naïve example of quantum entanglement generation out of an *isolated* system consisting of 2 identical, spin-1/2 atoms. Imagine that the electric dipole transition between the two spin states, denoted as $|\uparrow\rangle$ and $|\downarrow\rangle$, is forbidden. However, the two spin states are coupled through a stimulated Raman transition via an excited state $|e\rangle$ and the Rabi oscillation rate is controlled precisely by the detunings and intensities of the Raman beams [88]. The quantum mechanical state of the two atoms may be expressed as $|\eta_1, \eta_2\rangle$, where η_1 (η_2) represents the state of the first (second) particle and each of η_1, η_2 may assume values $\uparrow, \downarrow$, respectively.

Imagine also that we have an analogue knob controlling the atom-atom interaction. When the knob is set to a number λ, the atom-atom interaction energy is [50]

$$\begin{cases} \lambda c_0, & \text{if the atomic state is } |\uparrow,\downarrow\rangle, \\ 0 & \text{otherwise.} \end{cases} \tag{2.11}$$

We can generate an Einstein-Podolsky-Rosen (EPR) pair (maximum entanglement) with the following steps

1. With help of the stimulated Raman transition, we apply a $\pi/2$-pulse on both atoms. The state of the atomic system is transformed to

$$|\psi\rangle = \frac{1}{2}\left[|\uparrow,\uparrow\rangle + |\uparrow,\downarrow\rangle + |\downarrow,\uparrow\rangle + |\downarrow,\downarrow\rangle\right]. \tag{2.12}$$

2. We turn the interaction-knob up to a certain level for a certain time to introduce a $\pi/2$-pulse in the phase-shift of the atomic state. The state

of the atomic system is then transformed to

$$\begin{aligned} |\psi\rangle &= \frac{1}{2}\left[|\uparrow,\uparrow\rangle + e^{i\pi}|\uparrow,\downarrow\rangle + |\downarrow,\uparrow\rangle + |\downarrow,\downarrow\rangle\right] \\ &= \frac{1}{2}\left[|\uparrow,\uparrow\rangle - |\uparrow,\downarrow\rangle + |\downarrow,\uparrow\rangle + |\downarrow,\downarrow\rangle\right]. \end{aligned} \tag{2.13}$$

3. Now we selectively address the second atom with the stimulated Raman transition and produce a $\pi/2$-rotation. The state of the atomic system becomes

$$\begin{aligned} |\psi\rangle = &\frac{1}{2\sqrt{2}}\left[|\uparrow,\uparrow\rangle + |\uparrow,\downarrow\rangle\right] - \frac{1}{2\sqrt{2}}\left[-|\uparrow,\uparrow\rangle + |\uparrow,\downarrow\rangle\right] \\ &+ \frac{1}{2\sqrt{2}}\left[|\downarrow,\uparrow\rangle + |\downarrow,\downarrow\rangle\right] + \frac{1}{2\sqrt{2}}\left[-|\downarrow,\uparrow\rangle + |\downarrow,\downarrow\rangle\right] \\ = &\frac{1}{\sqrt{2}}\left[|\uparrow,\uparrow\rangle + |\downarrow,\downarrow\rangle\right]. \end{aligned} \tag{2.14}$$

Expression (2.14) represents an entangled state for the two atoms. Note that from Equation (2.12) to Equation (2.13), conditional evolution is needed; from Equation (2.13) to Equation (2.14), individual atom addressability is needed.

Now that we have an understanding of what entanglement is and how to generate it, we are well motivated to discuss how to realize arbitrary single-qubit gates and two-qubit gates in the fermionic Fock state qubit(s). The implementation of a single-qubit gate demands the capability of addressing each atom individually. As seen in the above example, this can be accomplished with the stimulated Raman transitions, as what is currently implemented with trapped ions [11, 74] and with neutral atoms [95]. In addition to the individual atom addressability, the realization of a two-qubit gate demands tunable interaction between qubits, upon which conditional evolution may be built. The

original proposal of a two-qubit gate for neutral atoms was based on collisions [50]. This scheme was realized experimentally with atoms in an optical lattice [67]. As is well-known, fermionic atoms in the same internal state cannot collide due to the Pauli exclusion principle. However, atoms in different internal states can be made to have a large collisional phase-shift, which can be used to engineer two-qubit SWAP gates, as proposed in Reference [44]. (A full SWAP gate performs a π-rotation, which swaps the qubit states $|01\rangle$ and $|10\rangle$, while a $\sqrt{\text{SWAP}}$ generates entanglements between the two qubits.) One significant advantage of this approach is that the scattering length can be made very large by tuning closer to the Feshbach resonance. The speed of each gate operation is therefore only limited by the trap frequencies.

In the realization of a $\sqrt{\text{SWAP}}$ gate, one should choose the trapping frequency ω of the optical trap and s-wave scattering length such that $(\hbar/m\omega)^{1/2}$ and $2a_s$ are comparable, thus optimizing the speed of $\sqrt{\text{SWAP}}$ gate [44]. For a set of parameters $\omega = 2\pi \times 1$ kHz and $a_s \sim 330a_0$, a high fidelity $\sqrt{\text{SWAP}}$ gate can be implemented in a time period ≈ 40 ms. It is straightforward to envision that with an array of many qubits, a sequence of $\sqrt{\text{SWAP}}$ operations can build scalable entanglement in this system. This two-qubit operation, together with single-qubit rotations, provides a set of universal quantum gates.

2.6 Qubit State Detection

The detection of each qubit at the end of a quantum computation is accomplished by spatially-resolved fluorescent imaging. Fluorescent imaging

technique has recently been refined to resolve atom pair separations down to nearest neighbors in a 1D optical lattice [52]. The reproducible fluorescent imaging has become a highly reliable tool for measuring the final quantum states of qubits [77].

To reliably detect the qubit state, we first displace the two spin component spatially. This can be accomplished with the same method that was used to separate the spin pair (see Figure 2.7 and Figure 2.11). When we perform the trap-splitting with an arbitrary state, the atom is ambiguously shifted both to the right and the left (in a state similar to the Schrödinger's cat). The fidelity of such shift can be just as high as the adiabatic trap-splitting, analyzed in the previous sections.

Then, we probe the location of the qubit, taking advantage of the spatial-resolution capability of the fluorescent imaging. This step can be performed with a few repeated detections for better fidelity, if necessary. Through the fluorescent imaging, the ambiguity of the position of the qubit is resolved: the atom is either found to the left or to the right, by the power of quantum projection (in analogy to finding out whether the cat is dead or alive). The probability of finding the qubit in one spin state or the other may be obtained by repeated measurements. The overall fidelity of this split-and-detect process can be made sufficiently high to fulfill the requirements of a realistic quantum computation.

2.7 Sources of decoherence

Decoherence is closely related to entanglement between system and environment. Decoherence so far is one of the major challenges in the way of a practical quantum computer for all the promising candidates listed in Table 1.1.

For any system bearing our interests, there is always the complimentary part—*the environment* which includes everything else that has interactions with the system but is not in the system— and together the two form an isolated *universe*. Decoherence occurs when a system interacts with its environment such that quantum entanglement is produced between the two [69]. Often, the environment contains large amount of degrees of freedom, that the decoherence process is practically irreversible in a thermodynamical sense. In this regard, decoherence results in the loss of information from a system into the environment.

We denote the system as $\mathcal{S}$ and the environment as $\mathcal{E}$. We assume that $\mathcal{S}$ has a basis consisting of two orthogonal states $\{|\alpha_i\rangle \, | i = 1, 2\}$. Initially, $\mathcal{S}$ is in state

$$|\phi\rangle = C_1 \, |\alpha_1\rangle + C_2 \, |\alpha_2\rangle \, , \tag{2.15}$$

$\mathcal{E}$ is in state $|\Phi_0\rangle$, and as a result, the universe is in state $C_1 \, |\alpha_1\rangle \, |\Phi_0\rangle + C_2 \, |\alpha_2\rangle \, |\Phi_0\rangle$. Then the system and environment are allowed to evolve together, for a certain period of time. As before, the interaction between the system

and the environment results in a conditional evolution:

$$\begin{array}{l} |\alpha_1\rangle\,|\Phi_0\rangle \rightarrow |\alpha_1\rangle\,|\Phi'\rangle\,, \\ |\alpha_2\rangle\,|\Phi_0\rangle \rightarrow |\alpha_2\rangle\,|\Phi''\rangle\,. \end{array} \tag{2.16}$$

At the end of the time period, the state of the universe becomes

$$|\Psi\rangle = C_1\,|\alpha_1\rangle\,|\Phi'\rangle + C_2\,|\alpha_2\rangle\,|\Phi''\rangle \tag{2.17}$$

At this time, the state of the system is not a well-defined state by itself—it is coupled with that of the environment in a non-locally correlated way. Decoherence does not generate wave function collapse. It only gives the appearance that the wavefunction of the system collapses. Often, there are immense number of degrees of freedom in $\mathcal{E}$. This has two closely related effects. Firstly, the inner product between $|\Phi'\rangle$ and $|\Phi''\rangle$ is made essentially zero; secondly, the time period for the reversal in the state of the universe becomes essentially infinity. If we trace off all the degrees of freedom belonging to the environment from Equation (2.17), we obtain the density matrix for the system:

$$\begin{aligned} \rho &= Tr_{\mathcal{E}}\left\{|\Psi\rangle\,\langle\Psi|\right\} \\ &= |C_1|^2\,|\alpha_1\rangle\,\langle\alpha_1| + |C_2|^2\,|\alpha_2\rangle\,\langle\alpha_2|\,. \end{aligned} \tag{2.18}$$

The system cannot be described by a pure state of its own, but by the density matrix ρ of Equation (2.18).

Our proposed system for quantum computation has many decoherence sources. For example, since we rely on stimulated Raman transition to imple-

ment the one-qubit gate, spontaneous Raman transitions are inevitable and this process entangles the system with the surrounding vacuum.

Other sources of decoherence in this system include spontaneous absorption and emission. Still another decoherence source comes from the shot noise of the laser tweezers, which results in fluctuation in the trapping potential. Yet another decoherence source comes from off-resonance photon-scattering of the optical tweezer. The photon-scattering effect in optical dipole trap was studied in Reference [35] and the scattering rate for a far-off-resonance trap is given by

$$\Gamma_{\text{scat}} = \frac{2A}{\hbar\omega_0}\left(\frac{\omega}{\omega_0}\right)^3 U_0, \tag{2.19}$$

where $A = \frac{4{\omega_0}^3\mu^2}{3\hbar c^3}$ is the Einstein coefficient, ω_0 is the resonance frequency and the ω is the laser frequency, U_0 is the well-depth.

Among the various decoherence sources, the laser intensity noise in the optical trap can be one of the major factors. Experimental control of intensity noise is discussed in Appendix A.6. Additionally, this can be reduced by injection-locked semiconductor lasers which can be intensity squeezed almost 10 dB below the shot noise [48]. The photon-scattering effect can also be reduced. Since the scattering rate is proportional to the cube of ω, large detuning can help the decoherence due to photon-scattering. The current estimate of various decoherence effects is made in Reference [22].

2.8 The DiVincenzo criteria

The DiVincenzo criteria have been discussed in Section 1.4. For convenience we reiterate the five DiVincenzo criteria for quantum computation here: for a system to be a candidate for an implementation of quantum computation, it should (1) be a scalable physical system with well-defined qubits, (2) be initializable to a simple fiducial state such as $|000\ldots\rangle$, (3) have decoherence times much longer than gate operation time, (4) have a universal set of quantum gates, and (5) permit high quantum efficiency, qubit-specific measurements. In this section, we test our system of an array of ultracold ^{6}Li qubits against the criteria for quantum computation, and show that it has the potential for satisfying these five DiVincenzo criteria.

First DiVincenzo criterion As shown in Figure 2.10, if we choose parameters near the upper-left corner, ultrahigh fidelity can be achieved in preparing a single pair of qubits. Thus our system provides well-defined qubits and fulfills first part of the first DiVincenzo criterion. Also the scalability of our system is guaranteed by the MEMS beam steering technology, by which a relatively high fidelity can still be ensured. This completes the first DiVincenzo criterion.

Second DiVincenzo criterion As explained in Section 2.3 and 2.4, the qubit preparation process automatically initializes the produced array of qubits in the antiferromagnetic Néel state $|\uparrow,\downarrow,\uparrow,\downarrow,\cdots,\uparrow,\downarrow\rangle$ [76]. Thus this fulfills the second DiVincenzo criterion.

Third DiVincenzo criterion With the decoherence analysis of Section 2.7, the decoherence time of this system depends on the photon shot-noise in optical trap, off-resonance photon-scattering, spontaneous absorptions and emissions, and spontaneous Raman transitions. Even so, this quantum computing system has much less of a decoherence problem in comparison with other proposals listed in Table 1.1.

Fourth DiVincenzo criterion The trap-splitting and fluorescent imaging techniques enables the detection of arbitrary qubit states with the individual atom addressability. This fulfills the fourth DiVincenzo criterion.

Fifth DiVincenzo criterion As explained in Section 2.5, we realized single-qubit gates, two-qubit gates, and other complicated qubit manipulation and operations using various techniques either in existence or developed in this report. All these evidences suggest that the third DiVincenzo criterion be also fulfilled.

The last two criteria with regard to the quantum networkability are yet to be confirmed for the fermionic Fock-state atomic qubits. However, we believe that no other system is known to satisfy all the five DiVincenzo criteria for quantum computation, while our system has the potential to do so.

Chapter 3

Calculations of Atomic Fock States Using Bethe Ansatz

Due to the potential application in quantum computation and information processing, few-body quantum states with a definite number of atoms and well-defined wavefunctions have recently become the focus of research endeavors. Theoretical work on producing atoms in Fock states has been done in many publications [27, 32, 82]. The role of physical parameters such as trap depth and trap size are considered. Possible time sequence in varying these parameters, either in parallel or in tandem, are also analyzed. However a systematic analysis involving the role of interaction is still largely missing in the literature. In this Chapter, we present a unique calculation model based on the Bethe ansatz.

3.1 Strongly interacting atoms

With their tendency to stick together, bosonic atoms rely on strong repulsive interactions for the production of Fock states. In the infinitely strong interaction regime, the so-called Tonks-Girardeau regime, calculations have been made trivial thanks to the boson-fermion correspondence in one-

dimension [37]. With the available experimental technology, it is possible to artificially generate strong interactions between bosonic atoms such as sodium. One method is to use Feshbach resonances [49]; another is to use the optical box technique to confine the atomic wavefunction in two of the three dimensions [72]. Even so, the Tonks-Girardeau regime remains experimentally challenging. To make it worse, with the maximum interaction strength that can be realized with the above techniques, we are left with a difficult many-body problem and no existing method to obtain a solution. Direct diagonalization of an N-atom hamiltonian has been used in Reference [32]. However, there are various drawbacks in this method, not to mention that it is very time-consuming to calculate the quantum state for a large number of particles.

There is also a technical reason to tune the interaction strength during the number-state experiment. In order to load a Bose-Einstein condensate into the optical box, the transverse trapping frequency is often relaxed in the beginning and tightened up toward the end. This is done so as to promote loading efficiency and then enhance atom-atom interactions. We need to analyze the change in the atomic state during this process to gain insight in the fidelity of the number-state production.

To face up to reality, we need a new model that can calculate the energy levels and wavefunctions of an N-atom system with variable interaction strength. The Bethe ansatz method makes no assumptions about the interaction strength between atoms and thus provides an ideal tool for this purpose and we are able to study the connections across various interaction regimes.

This method was first developed by Hans Bethe to solve the problem of a one-dimensional (1D) spin 1/2 Heisenberg ferromagnet [9]. Since it's invention, Bethe's method has found important applications in the study of interacting spin systems [61, 80, 90]. It has also been applied to solve the problem of a 1D bosonic gas with repulsive δ-function interactions [34, 43, 60, 62, 68, 86, 94].

We use the Bethe ansatz method to calculate the single-particle energy levels for arbitrary interaction. With these calculations, we are able to chart Fock states in the parameter space with interaction as one of its dimensions.

3.2 Formulation of the problem

In order to tackle the interacting many-body problem with arbitrary interaction strength, we make a few simplifications. Firstly, we compromise on the exactness of the trapping potential. We assume that the trapping potential is a one-dimensional (1D) square well potential. For an N-particle system, the configuration space, consisting of the N coordinates, $\{x_1, x_2, \cdots x_N\}$, would be a N-dimensional (ND) Euclidian space. Secondly, we assume the atom-atom interaction potential is a δ-function.

A many-atom system with a δ-function interaction trapped in 1D square well potential with finite well depth was first studied using the Bethe ansatz in Reference [60]. Following the notations and formulation therein, we specify the 1D square well potential by its length L and depth V_0. We write the atom-atom interaction potential as $\frac{\hbar^2}{m} c\delta(x_i - x_j)$, where x_i and x_j are the positions of the interacting particles, $\hbar$ is Planck's constant, m is an atom's mass, and c

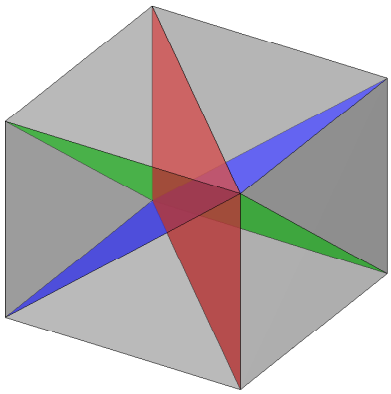

Figure 3.1: Configuration space for a 3-atom system. The space is divided by the δ-interaction into wedged open spaces. The red, blue, and green surfaces denotes the positions where the atom-atom interactions take place. Together with the square-well potential, the spaces where atoms can move freely are the so-called Weyl Chambers [60].

is the interaction strength with dimensions [1/length]. In Figure 3.1, we show the configuration space of 3-particles. According to Reference [79] we have the following expression for c,

$$c = \frac{4a}{{a_\perp}^2}\left(1 - C\frac{a}{a_\perp}\right)^{-1}, \tag{3.1}$$

where a is the s-wave scattering length in 3D space, $a_\perp = \sqrt{2\hbar^2/m\omega_\perp}$, $\omega_\perp$ is the transverse trapping frequency, and $C \approx 1.4603$ is an empirical constant number. Since the interaction strength c depends on both the scattering length and the transverse trapping frequency $\omega_\perp$, tuning either of them will affect it. The transverse trapping frequency may be controlled by the optical box parameters [72], and the scattering length may be adjusted by a Feshbach resonance [49]. To gain a sense of order of magnitude, for sodium atoms

trapped in a 1D optical box with transverse trapping frequency $\omega_\perp = 2\pi \times 150$ kHz and zero magnetic field, we have $c = 16863.6$ cm^{-1}, and for ^{87}Rb atoms in a similar trap with zero magnetic field, we have $c = 92391.6$ cm^{-1}.

We can properly scale our equations to contain dimensionless quantities only. One way to do that is to use $1/c$ as the unit of length and $\hbar^2 c^2/m$ as the unit of energy. The square well potential is then

$$V(x) = \begin{cases} -{k_0}^2/2, & |x| < x_0/2, \\ 0, & \text{otherwise}, \end{cases} \tag{3.2}$$

where k_0 and x_0 are dimensionless numbers. With these parameters, the well width is $L = x_0/c$ and well depth is $V_0 = \hbar^2 c^2 {k_0}^2/2m$ in cgs unit.

The hamiltonian for the many-body system may be written as

$$\mathcal{H} = -\frac{1}{2}\sum_{i=1}^{N}\frac{\partial^2}{\partial x_i^2} + \sum_{i=1}^{N} V(x_i) + \sum_{\substack{i,j=1 \\ i>j}}^{N} \delta(x_i - x_j). \tag{3.3}$$

This way of dimension-scaling gives simple equations, with the interaction strength hidden from any consideration. However, the resulting equations are valid only for $0 < |c| < \infty$.

Another way to scale the quantities is using L as the unit of length and $\hbar^2/mL^2$ as the unit of energy. The potential of the square well is given as

$$V(x) = \begin{cases} -{k_0}^2/2, & |x| \leq 1/2, \\ 0, & |x| > 1/2, \end{cases} \tag{3.4}$$

where, as before, k_0 is a dimensionless number. The N-atom hamiltonian is then

$$\mathcal{H} = -\frac{1}{2}\sum_{i=1}^{N}\frac{\partial^2}{\partial x_i^2} + \sum_{i=1}^{N} V(x_i) + c\sum_{\substack{i,j=1 \\ i>j}}^{N} \delta(x_i - x_j). \tag{3.5}$$

This scaling method does not put any restrictions on the interaction strength c which is explicit in the equations. We will refer to the first scaling scheme as 'c-scaling', with square-well potential given by (3.2) and the many-body hamiltonian given by Equation (3.3); the second scaling scheme as 'L-scaling', with the Equation (3.4) and (3.5). We adopt c-scaling and implicitly use the Equation (3.1) and Equation (3.2) for subsequent discussions, except in Section 3.3, Appendix B.2, and B.3, where L-scaling is used for the discussions of varying interaction.

3.3 The perturbation and variational solutions

Before setting out to discuss the Bethe ansatz method, it is beneficial to consider some special limiting cases and try different approximation methods on them for these special limiting cases.

First of all, for the cases $c = 0$ and $c = \infty$, the solutions of Equation (3.5) are trivial. In the case of $c = 0$, the system reduces to a non-interacting one-body problem, whose energy levels are $k^2/2$ and k is given by a transcendental equation,

$$\frac{k}{k_0} = \begin{cases} |\sin(k/2)|\,, & \sin k < 0, \\ |\cos(k/2)|\,, & \sin k > 0. \end{cases} \tag{3.6}$$

whose wavefunction is

$$\psi(x) = \begin{cases} Ae^{\kappa x}, & x < 0, \\ Be^{ikx} + Ce^{-ikx}, & 0 < x < 1, \\ De^{-\kappa x}, & x > 1, \end{cases} \tag{3.7}$$

where $\kappa = \sqrt{{k_0}^2 - k^2}$ and A, B, C, D are coefficients that can be determined separately.

In the case of $c = \infty$, due to the finite energy restriction, the many-body wavefunction must remain antisymmetric at any point where two atom meet. In other words, the many-atom wavefunction is similar to a many-fermion wavefunction: each of the atoms exclusively occupies an energy level $k^2/2$, where k is a root of Equation (3.6)—in compliance with Pauli Exclusion Principle. This is the celebrated boson-fermion correspondence principle, first discovered in Reference [37].

Of course, we can do more than just the special cases. In the weak interaction regime, $c \ll 1$, we can treat problem with perturbation or variational theory.

To illustrate the perturbation approach, one can split the hamiltonian in Equation (3.5) into $H = H_0 + H_1$, where the zeroth-order part is

$$H_0 = -\frac{1}{2}\sum_{i=1}^{N}\frac{\partial^2}{\partial x_i^2} + \sum_{i=1}^{N} V(x_i) \tag{3.8}$$

and the first-order part is

$$H_1 = c\sum_{\substack{i,j=1 \\ i>j}}^{N} \delta(x_i - x_j). \tag{3.9}$$

According to perturbation theory, the first-order correction to the total energy of the N-atom system may be obtained as

$$\begin{aligned} \Delta E &= \sum_{\substack{i,j=1 \\ i>j}}^{N} \iint \psi^*(x_i)\psi^*(x_j)c\delta(x_i - x_j)\psi(x_i)\psi(x_j)dx_i dx_j \\ &= N(N-1)c\int |\psi(x)|^4 dx. \end{aligned} \tag{3.10}$$

In Figure 3.2**a**, we plot the average energy (total energy divided by number of atoms) vs interaction strength.

The variational approach to calculate single-particle energies is motivated by the wavefunction form taken by the free particles in Equation (3.7). In the weak limit, we can continue to assume that each atom is described by a wave number k_i for $i = 1, 2, \cdots, N$. Then its energy is $k^2/2$ and its wavefunction is of the form of Equation (3.7). The rest of the calculation is done in a routine way and the resulting single-particle energy levels are plotted in Figure 3.2**b**.

As will become clear in Appendix B.2, the calculations in the weak (and strong) limit will help determine the correctness of the Bethe ansatz solutions with arbitrary interaction strength.

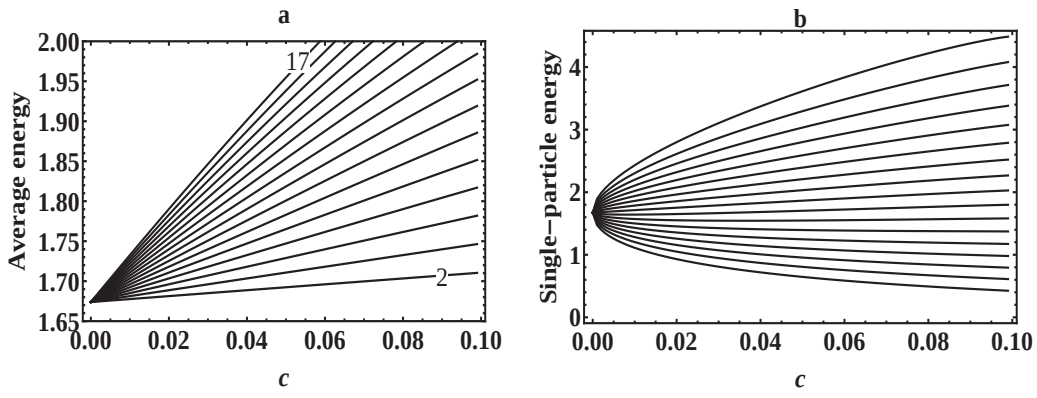

Figure 3.2: Eigenenergies of Equation (3.5) for weakly interacting atoms with perturbation and variational methods. The zero energy reference is the bottom of the square well. **a**. The average energy per atom for a system of 2 through 17 atoms. **b**. The single-particle energies of 17 interacting atoms.

3.4 Bethe Ansatz solutions

We discuss how the Bethe ansatz can be used to calculate Fock states production in many bosonic atoms with arbitrary interaction strengths. We adopt the 'c-scaling': we use $\hbar^2/mL^2$ as the energy unit, L as the length unit, $1/L$ as the wave number unit, *etc.*

Relevant to the production of Fock states is to solve the following eigenvalue problem

$$\mathcal{H}\psi(\vec{x}) = E\psi(\vec{x}), \tag{3.11}$$

where $\vec{x}$ is the shorthand for $x_1, x_2, \cdots, x_N$.

In this section, we obtain the Bethe ansatz solutions. We are primarily interested in bound states whose wavefunctions must be normalizable. As a minimum requirement, the wavefunction of a bound state must satisfy $\lim_{x\to\pm\infty} \psi(\vec{x}) = 0$.

As studied in the literature [60, 62, 94], the Bethe ansatz introduces a set of unknown wave numbers $\vec{k} = \{k_1, k_2, \cdots, k_N\}$. In conjugate to these wave numbers, another set $\vec{\kappa} = \{\kappa_1, \kappa_2, \cdots, \kappa_N\}$ is defined as

$$\kappa_j = \sqrt{k_0^2 - {k_j}^2}, \tag{3.12}$$

for $j = 1, 2, \cdots, N$. The total energy of the Bethe ansatz state is $E = -\sum_j^N {\kappa_j}^2/2 = \sum_j^N \left({k_j}^2 - {k_0}^2\right)/2$. The eigenfunction (wavefunction) of Equation (3.11) is piecewise continuous in the N-dimensional coordinate space $\{x_1, x_2, \cdots, x_N\}$. For simplicity, we consider three representative regions in

the N-dimensional coordinate space:

$$R_1 \;:\; -x_0/2 < x_1 < x_2 < \cdots < x_N < x_0/2, \tag{3.13}$$

$$R_2 \;:\; x_1 < -x_0/2 < x_2 < \cdots < x_N < x_0/2, \tag{3.14}$$

$$R_3 \;:\; -x_0/2 < x_1 < \cdots < x_{N-1} < x_0/2 < x_N. \tag{3.15}$$

R_1 represents a region where all particles are trapped; $R_{2,(3)}$ represent a region where the 1st (Nth) particle tunnels into the left (right) barrier. In fact, each of these regions falls in a class consisting of $N!$ regions that are related by coordinate permutations. For ease of reference, we name $\mathcal{A}$ the class of regions that can be obtained from R_1 by mere coordinate permutations and study the wavefunctions in these regions at once.

We denote the wavefunctions in a region of $\mathcal{A}$ as $\phi_\tau(\vec{x})$, where τ is the permutation operator that transforms R_1 into this region, *i.e.*, $R_\tau = \tau R_1$. This wavefunction is the superposition of pure plane waves with "$\pm$ signs" times permuted wave numbers,

$$\phi_\tau(\vec{x}) = \sum_{\varsigma \in C_2^N} \sum_{\sigma \in \mathbf{G}} A\left(\varsigma, \sigma; \tau\right) e^{i(\varsigma\sigma\vec{k})\cdot\vec{x}}. \tag{3.16}$$

where $\varsigma \equiv \{\varsigma_1, \varsigma_2, \cdots, \varsigma_N\}$ represents a possible combination of N signs each of which is either $+$ or $-$, C_2^N represents the group of such operations (direct product of N C_2 groups), $\mathbf{G}$ is the permutation group of N particles, and $A(\varsigma, \sigma; \tau)$ is the superposition amplitude.

It is clear that the amplitude $A(\varsigma, \sigma; \tau)$ is a functional of the sign-flipping operator, the wave number permutation operator, and the region per-

mutation operator. By bosonic particle permutation symmetry, we establish the first set of equations among the superposition amplitudes,

$$A(\varsigma, \sigma; \tau) = A(\varsigma, \tau\sigma; \mathbf{I}), \tag{3.17}$$

where $\mathbf{I}$ is the identity element in the permutation group.

The wavefunctions in region R_2 have a more complicated form,

$$\phi_2(\vec{x}) = \sum_{\varsigma} \sum_{\sigma \in \mathbf{G}} B(\varsigma, \sigma) e^{(\sigma\vec{\kappa})_1 x_1} e^{i \sum_{j=2}^{N} (\varsigma\sigma\vec{k})_j x_j}, \tag{3.18}$$

where $(\varsigma\sigma\vec{k})_j$ is the jth component wave number after the permutation operation σ and the sign-flipping operation ς, $(\sigma\vec{\kappa})_1 \equiv \sqrt{k_0^2 - (\sigma\vec{k})_1^{\,2}}$, which can be regarded as an extra operator on top of the permutation operator σ, and $B(\varsigma, \sigma)$ is the superposition amplitude. Similarly, the wavefunctions in region R_3 may be written as,

$$\phi_3(\vec{x}) = \sum_{\varsigma} \sum_{\sigma \in \mathbf{G}} C(\varsigma, \sigma) e^{i \sum_{j=1}^{N-1} (\varsigma\sigma\vec{k})_j x_j} e^{-(\sigma\vec{\kappa})_N x_N}, \tag{3.19}$$

where $(\sigma\vec{\kappa})_N \equiv \sqrt{k_0^2 - (\sigma\vec{k})_N^{\,2}}$ and $C(\varsigma, \sigma)$ is the superposition amplitude.

From Equation (3.12), it is clear that if, for some i, $k_i > k_0$, then there will be a corresponding pure imaginary κ_i. In turn, any pure imaginary κ_i will cause the Bethe ansatz wavefunction to be unnormalizable (see Equation (3.18) and Equation (3.19)). Then from the normalizability requirement stated in the beginning of this section, we reason that *a Bethe ansatz state is bound if and only if all of the wave numbers are real and smaller than* k_0. Since we are

primarily interested in bound states, from now on we implicitly mean bound state when we say Bethe ansatz state, unless otherwise stated.

Once we get the Bethe ansatz wavefunctions, the rest is straightforward. The main features of the many-body hamiltonian (Equation (3.3)) are the singular δ-function particle-particle interaction and the nonzero potential step at the edge of the square well. The Bethe ansatz method an elegantly treats both as boundary conditions. The boundary conditions at $x_i - x_j = 0$ for $i, j = 1, 2, \cdots, N$ in regions of class $\mathcal{A}$ requires the continuity of the wavefunctions on the one hand,

$$\psi|_{x_i = x_j{}^+} = \psi|_{x_i = x_j{}^-} \tag{3.20}$$

and certain discontinuity in their first-derivatives on the other,

$$\left[\frac{\partial\psi}{\partial x_i} - \frac{\partial\psi}{\partial x_j}\right]\Bigg|_{x_i = x_j{}^+} - \left[\frac{\partial\psi}{\partial x_i} - \frac{\partial\psi}{\partial x_j}\right]\Bigg|_{x_i = x_j{}^-} = 2c\,\psi|_{x_i = x_j}\,. \tag{3.21}$$

The boundary conditions at $x_i = \pm x_0/2, i = 1, 2, \cdots, N$ require the continuity of both wavefunctions and their first-derivatives:

$$\psi|_{x_i = x_0/2^+} = \psi|_{x_i = x_0/2^-} \tag{3.22}$$

$$\left.\frac{\partial\psi}{\partial x_i}\right|_{x_i = x_0/2^+} = \left.\frac{\partial\psi}{\partial x_i}\right|_{x_i = x_0/2^-}\,. \tag{3.23}$$

Plugging Equation (3.16), Equation (3.18), and Equation (3.19) into Equation (3.20), Equation (3.21), Equation (3.22), and Equation (3.23) and including Equation (3.17), we obtain the complete group of equations for our original problem.

To get the eigen-energies, it suffices to keep just the wave numbers and eliminate all other unknowns. Doing so yields the following secular equations for the N wave numbers,

$$\pi I_j - x_0 k_j = 2\sin^{-1}\left(\frac{k_j}{k_0}\right) + \sum_{\substack{l=1 \\ l\neq j}}^{N} \left[\tan^{-1}(k_j + k_l) + \tan^{-1}(k_j - k_l)\right], \quad (3.24)$$

where $j = 1, 2, \cdots, N$, and $I = \{I_1, I_2, \cdots, I_N\}$ is a set of preselected integers.

In retrospect, you may be wondering how R_1, R_2, and R_3 have been chosen and why we haven't included more regions (and more equations), possibly with two or more particles lying outside the trap area simultaneously. In fact, this is possible, but only with small probability for deeply bound states. The effect on the number-state condition can be ignored. Firstly, insofar as all the representative limiting cases (weak, strong interaction limit and deep trap limit), our Bethe ansatz solutions agree with known results (see Figure 3.7**a** and Appendix B.1). Secondly, the energy spacings between single-particle levels are large near the strong interaction regime where Fock state experiments take place most likely and therefore the probability for more than one particle to tunnel into the barrier is negligible at all times. For this reason, we argue that the Bethe ansatz-based approach is a sufficiently good approximation to our problem.

Equation (3.24) is a transcendental equation and we solve it numerically. We must pick a set of integers $I = \{I_1, I_2, \cdots, I_N\}$ before we start the numerical computation. Apparently, not any set of integers would lead to a physically meaningful solution. As argued in Appendix B.2, we find that

Equation (3.24) *yields valid solutions if and only if the set of integers* I *are mutually distinct*, which is similar to the theorem in Reference [94]. A corollary of this is that the wave numbers thus obtained have mutually distinct absolute values. Because of this one-one correspondence, we use the set I as the *quantum numbers* for the corresponding Bethe ansatz state.

Besides knowing what set of integers are valid quantum numbers, we need to identify the ground state and the first-excited state. As argued in Appendix B.3, we find that the ground state of an N-atom system has the quantum numbers $\{1, 2, \cdots, N\}$, and the first-excited state has the quantum numbers $\{1, 2, \cdots, N-1, N+1\}$ (see Figure 3.3).

Without loss of generality, we reorganize the set of wave numbers such that $0 < k_1 < k_2 < \cdots < k_N < k_0$. We define *the* j*th single particle energy* as $e_j = -{\kappa_j}^2/2$, for $j = 1, 2, \cdots, N$.

On the other hand, had we chosen the L-scaling, we would have arrived at the following equivalent secular equations for the wave numbers:

$$\pi I_j - k_j = 2\sin^{-1}\frac{k_j}{k_0} + \sum_{\substack{l=1 \\ l\neq j}}^{N}\left[\tan^{-1}\frac{k_j + k_l}{c} + \tan^{-1}\frac{k_j - k_l}{c}\right]. \qquad (3.25)$$

By solving the secular equations (Equation (3.24) and/or Equation (3.25)) for the wave numbers k_i's, we can get the single-particle energy levels and the many-particle total energy. Figure 3.3 **a** and **b** gives the dependence of the total energies of the low-lying Bethe ansatz states on trap depth V_0 and interaction strength c, respectively. Note that there are crossovers be-

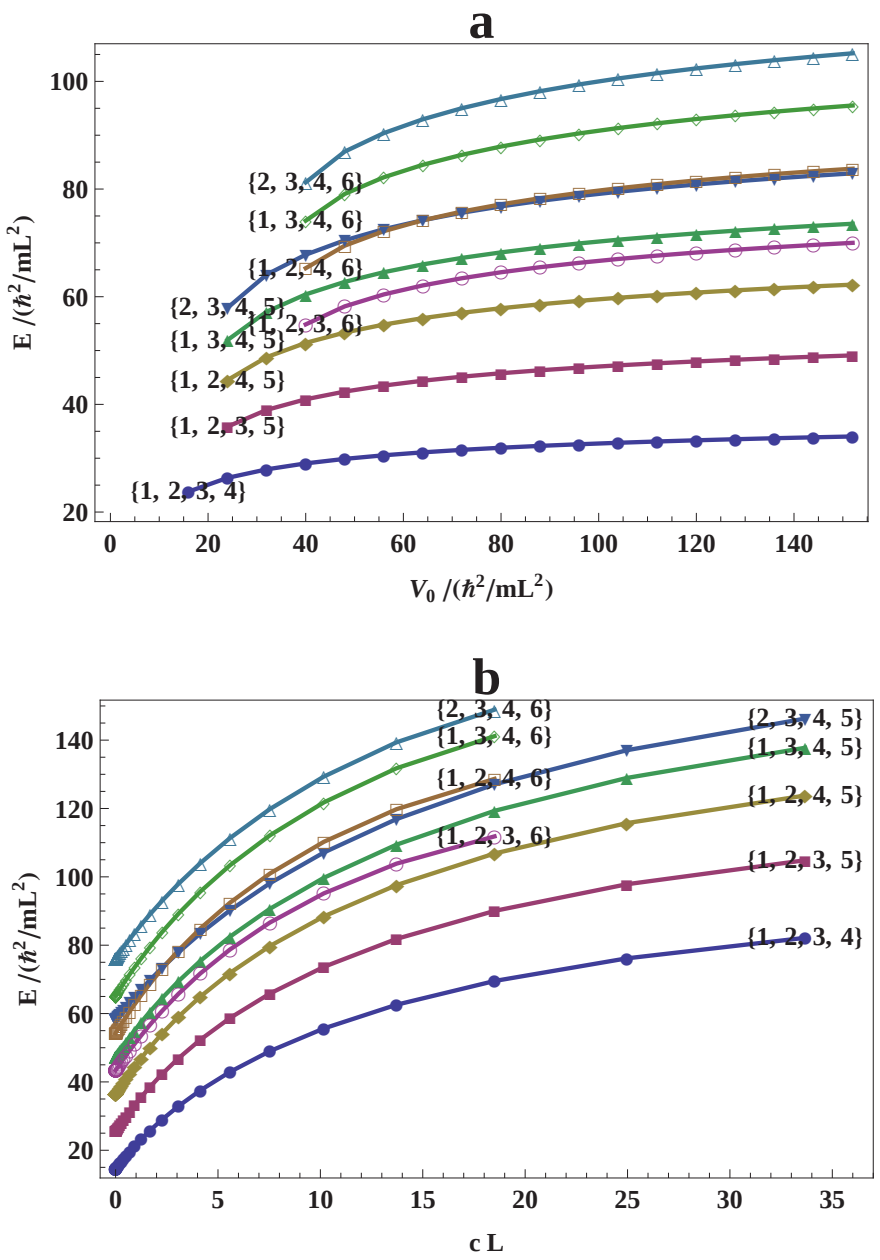

Figure 3.3: Bethe ansatz states for sodium atoms. The total energy of 4-particle bound states are plotted against trap depth (**a**) and interaction strength (**b**). The numbers at the beginning of each energy level are the quantum numbers of the bound state. We used the bottom of the trap as the energy zero. Trap size $L = 5$ μm. Transverse trapping frequency $\omega_\perp = 2\pi \times 150$ kHz.

tween some of the energy levels as the trap depth (or interaction strength) is changed. Also note that the slopes at very small c agrees with the calculated values by perturbation theory (see Section 3.3).

3.5 More about the single-particle energies

We are used to thinking of the concept of 'single-particle energies'—each particle has a definite energy consisting of kinetic energy and potential energy. But single-particle energies are only well-defined for free particles. In interacting many-body physics, the 'single-particle energy' may not be well-defined. In fact, the Bethe ansatz 'single-particle energy', ${k_j}^2/2$, may be purely conceptual. As the interaction strength is varied from extremely weak to extremely strong, we showed the panorama of the 'single-particle energies' of the many-atom system across many orders of magnitude in the interaction strength. In Figure 3.4**a-h**, we show the transition of the energy levels from a free-boson system to a free-fermion system.

One interesting fact of the single-particle energy levels is that a dip occurs in the lowest single-particle level as the interaction strength c reaches the intermediate regime, even for the many-body ground-states. The minimum number of particles for this feature to occur is two and Figure 3.5 shows the dip with a closeup view, being more conspicuous in excited states with large particle number. Nevertheless, a dip in the lowest single-particle energy is anticipated. As calculated both in the Bethe ansatz and in the variational methods, the lowest single-particle energy decreases as interaction increases

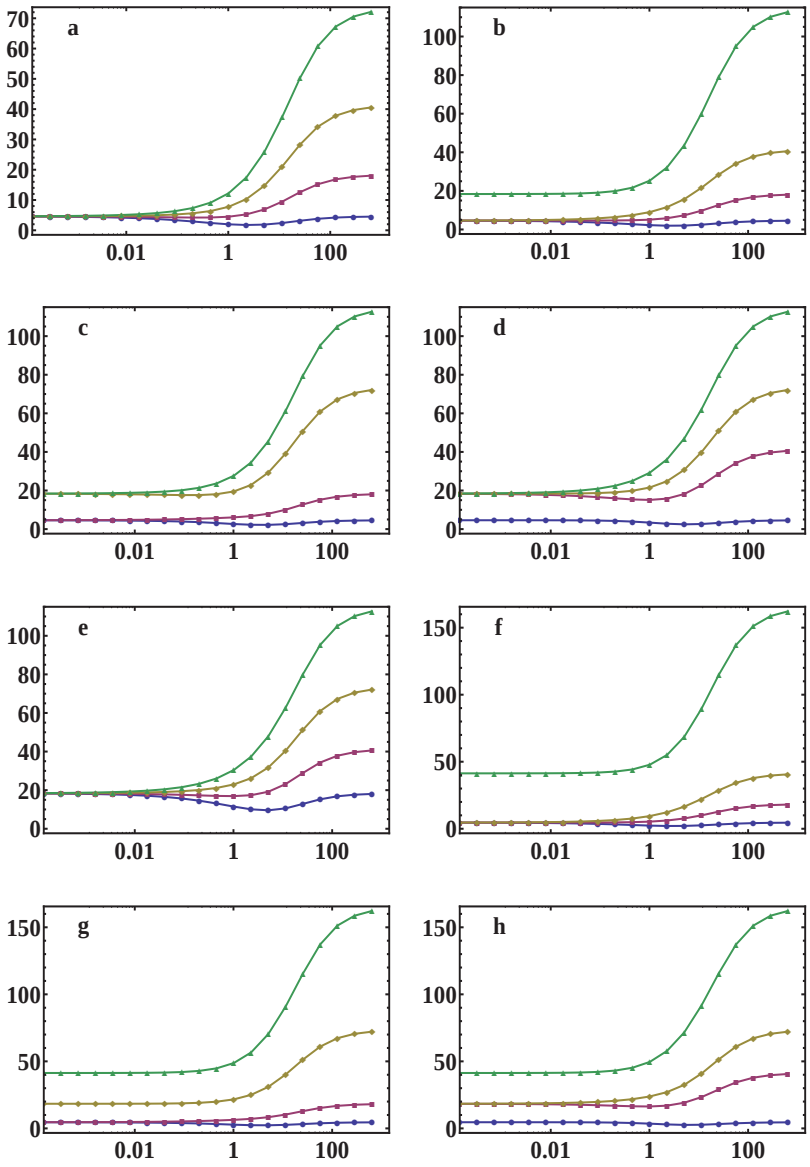

Figure 3.4: Bethe ansatz single-particle energies for sodium atoms. The energy zero is set to the bottom of the trap. The horizontal axis is the interaction c (in unit of $\hbar^2/2mL^2$) and the vertical is the single-particle energy (circle, square, diamond, and triangle in that order). Trap size $L = 5$ μm. Transverse trapping frequency $\omega_\perp = 2\pi \times 150$ kHz. Panel from **a**-**h** shows the ground state and the lowest 7 excited states of Bethe ansatz solutions as shown in Figure 3.3.

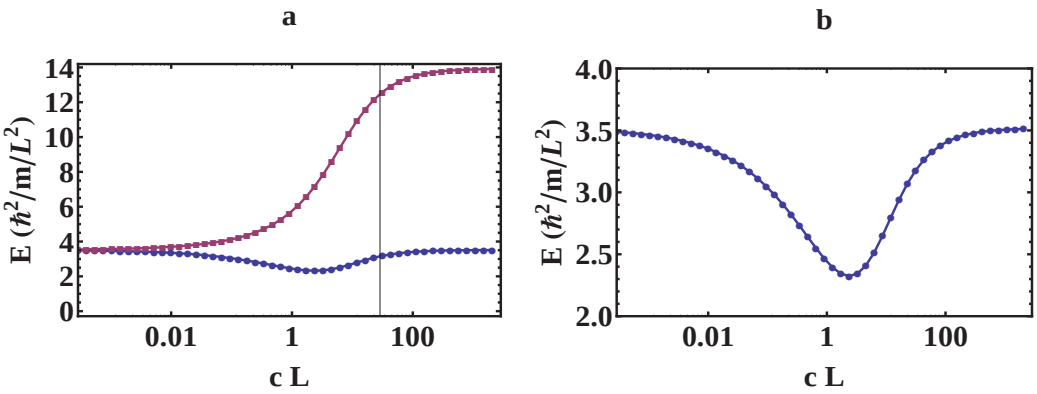

Figure 3.5: **a.** Single-particle energies of 2 sodium atoms in a square well of width 100 μm. **b.** Zoomed-in view of the dip in the lowest single-particle energy.

when $c \ll 1$ (Figure 3.2). However, for both free bosons and free fermions, the lowest single-particle energy should be the same. That is, as the interaction strength varies from extremely weak through extremely strong, the lowest single-particle energy, though first decreases then increases and eventually approaches the same value as $c \to \infty$. This feature, if confirmed, will become an interesting phenomenon. As is well-known, the zero energy in the ground state, $\sim \hbar^2/2mL^2$, originates from the Heisenberg uncertainty principle. If this energy is reduced beyond the uncertainty limit, it has a similar implications to squeezed state in quantum optics.

We designed a gedanken experiment to probe the single-particle energies in the interacting many-atom system. As shown in Figure 3.6, the system is sandwiched in a transistor-like environment with a source, a drain and a gate. We monitor the flow of atoms—the atomic 'current'. Resonance tun-

nelling occurs when the energy levels of the system and the gate are aligned. By tuning the width or energy offset of the gate, we expect to observe peaks in the current whenever a resonance tunnelling occurs. Likewise, by tuning the inter-particle interaction strength c in the system, the same resonance effect should be observed. If a dip is present in the lowest single-particle energy level, it should be reflected in the atomic current. Of course, some details remain to be cleared. For example, the single-particle energies may be modified by the complex trapping potential of Figure 3.6. Possibly, the Bethe ansatz method can be used for that calculation, too.

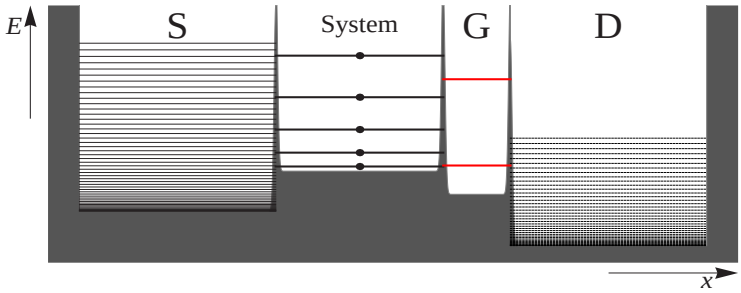

Figure 3.6: Gedanken experiment designed to probe the 'single-particle' (quasi-particle) energy. The experimental setup consists of an ultracold atom source (S), a controlling gate (G) and a drain (D). We assume S is full of particles while D is empty. The 1D many-atom system (System) is embedded between the source and the gate. The source, system, gate, and drain are separated by δ-barriers, which may be generated by tightly focused blue-detuned laser beams. The source and drain may be considered as reservoirs whose chemical potentials can be controlled. The experiment is designed to detect the atomic 'current', which is throttled by the gate energy offset and/or size through the resonant tunnelling. The energy levels are drawn schematically.

3.6 Atomic Fock states

We now apply the results of the previous sections to the production of Fock states. We can safely assume no atom with positive energy is present near the optical trap. In reality, if an atom acquires positive energy, it would be quickly swept out of the chamber by vacuum pumps. Therefore, it is safe to assume that the states in the continuum spectrum are virtually unoccupied all the time.

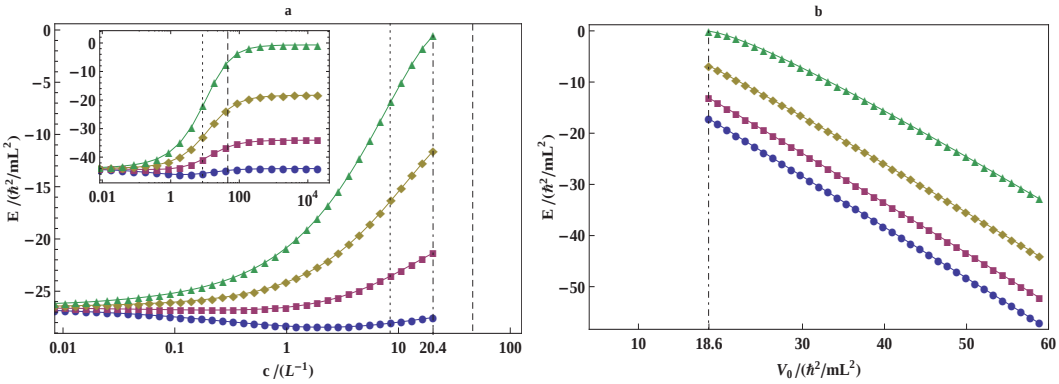

Figure 3.7: Single-particle energies of 4 sodium atoms in Bethe ansatz ground states. Trap size $L = 5\mu$m. **a.** Dependence on interaction strengths (c). Trap depth $V_0 = k_B \times 25$nK, where k_B is Boltzmann's constant. The dotdashed vertical line denotes the maximum interaction strength above which no Bethe ansatz state of 4-atom system exists. The other two vertical lines denote the interaction strengths of sodium (dotted) and ^{87}Rb (dashed) atoms at $\omega_\perp = 2\pi \times 150$ kHz and zero magnetic field. Inset, the trap depth is lifted to $k_B \times 40$nK, the condition at which all 4 atoms remain trapped to the Tonks limit. **b.** Dependence of the single-particle energies of a 4-atom system on the trap depth (V_0). Transverse trapping frequency $\omega_\perp = 2\pi \times 150$ kHz. Magnetic field is zero. The vertical line (dotdashed) denotes the minimum trap depth below which no bound state of the 4-atom system exists.

As dictated by Bethe ansatz, for some given trap parameters (depth V_0, trap size L, scattering length a, and transverse trapping frequency $\omega_\perp$), N atoms can be contained in the trap if and only if there is an N-atom Bethe ansatz state. The energy levels for an N-atom system has been calculated, by numerically solving Equation (3.24). As an example, Figure 3.7 shows a 4-atom Bethe ansatz state that ceases to exist in certain regions of the parameter space. In the main plot of Figure 3.7**a**, the 4-atom Bethe ansatz state can only exist *up* to certain interaction strength for a small trap depth, while in the inset the Bethe ansatz state exists regardless of the interaction for a large trap depth; in panel **b** of the same figure, the 4-atom Bethe ansatz state can only exist *down* to a certain trap depth. We assume that all other parameters are held unchanged. We define *trap capacity* to be the maximum number of particles that can be contained. Trap capacities put upper bounds on the possible Fock states. The whole parameter space is thus partitioned into zones of certain trap capacities. We define the boundaries of these partitions as the *ionization thresholds*, because atom numbers change only at these boundaries in an adiabatic laser-culling process. In Figure 3.8 we show how Bethe ansatz solutions discontinue for 2, 3, 4, 5 and 6 atoms while the corresponding ionization thresholds are approached.

Now that we obtained the trap capacity as the upper limit on the atom number of Fock states that can be contained in a given trap, it remains to be pursued whether or not this limit can be reached. The adiabatic laser culling technique developed in Reference [32] and the simulations in Tonks-Girardeau

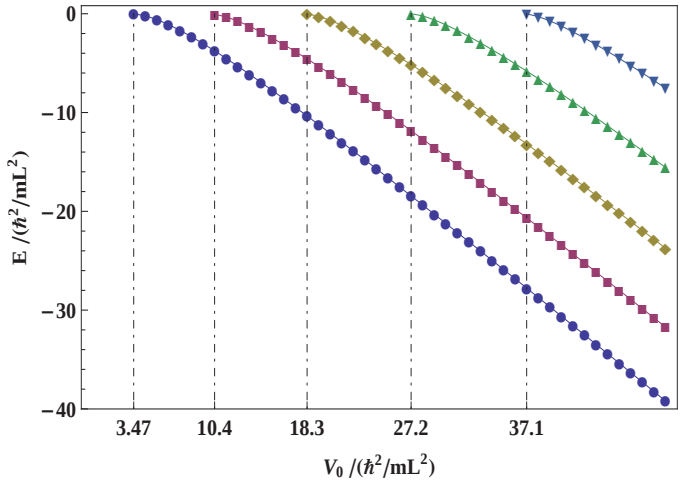

Figure 3.8: Ionization thresholds of sodium atoms with all parameters fixed except trap depth. Only highest single particle energies of the Bethe ansatz N-atom states are shown for $N = 2$ (circle), 3 (square), 4 (diamond), 5 (upright triangle), and 6 (invert triangle). Trap size $L = 5$ μm; Transverse trapping frequency $\omega_\perp = 2\pi \times 150$ kHz. The ionization thresholds (with the current numeric calculation step size) are also ticked along the horizontal axis.

region in Reference [27, 82] seem to suggest that it is possible to reach the trap capacity with the ultracold technique [21, 72].

For bosonic atoms, a convenient starting point is a BEC that is trapped in 1D optical box. Ignoring excitation effects for now, it is useful to view the process from the angle of quantum optics and regard the state of the BEC as a coherent state [5]. A coherent state is essentially a superposition state of an infinite number of Fock states whose particle numbers form a Poisson distribution. As one adiabatically reduces the trap capacity, a smaller and smaller maximum number is enforced on the possible Fock states in the superposition. The system state thus undergoes two changes side by side: No.1,

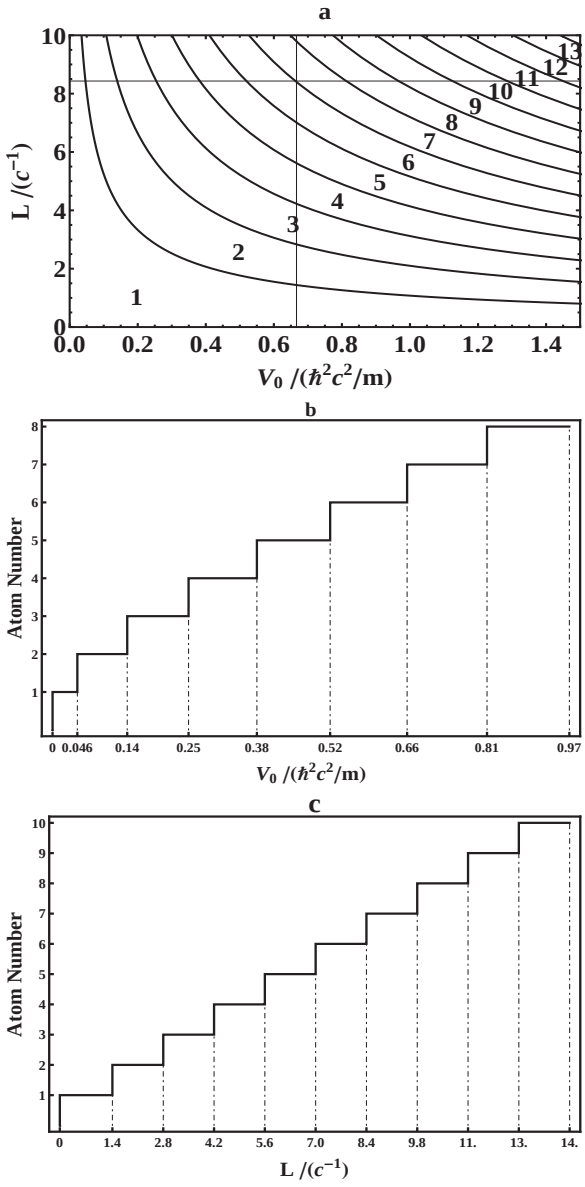

Figure 3.9: Map of Fock states and the calculated ionization thresholds for sodium atoms in a 1D optical trap in the adiabatic limit. Transverse trapping frequency $\omega_\perp = 2\pi \times 150$ kHz and zero magnetic field are assumed. The interaction strength is implicit in the unit we adopted, since c^{-1} and $\hbar^2 c^2/m$ are used to make the axes dimensionless. **a.** Contour plot of Fock states as function of trap depth and size; **b.** and **c.** views of cross-sectional cuts along the lines indicated in **a**, respectively. The ticks on horizontal axes give the corresponding ionization thresholds.

more and more high-energy atoms are ejected; No.2, more and more high-number Fock states are eliminated, resulting in the so-called *squeezed states*. Each of these two changes has its distinctive effect on the system state: the first leads to smaller and smaller average particle number $\overline{N} = \langle N \rangle$ whereas the second leads to a reduction in the number uncertainty $\sigma^2 = \left\langle N^2 - \overline{N}^2 \right\rangle$. Under optimal experimental conditions, the process continues until at some point, while the average number $\langle N \rangle > 0$, the number uncertainty $\sigma \approx 0$. A rigorous simulation of this would require calculating the value $\frac{\sigma}{\overline{N}}$ as a function of time in a dynamic process.

There are several ways to tune the physical parameters to achieve the squeezing effect. In previous references [27, 32, 82], only culling (reducing trap depth), squeezing (reducing trap size), or some combinations of the two are discussed. We propose to tune the interaction strength as a complementary method. In certain circumstances, atom-atom interaction strength c may be a better tuning method. In still other circumstances, it may be the only tunable parameters. Thus interaction strength plays a key roll in producing Fock states in many-atom systems.

To recap, the path to Fock states is clear now. By tuning the physical parameters of the 1D optical trap adiabatically, we force the ultracold atom sample through a series of quantum collapses until it eventually reaches the desired Fock state with some acceptable fidelity. In Figure 3.9, we show a map of Fock states and ionization thresholds in the parameter space of trap size and trap depth.

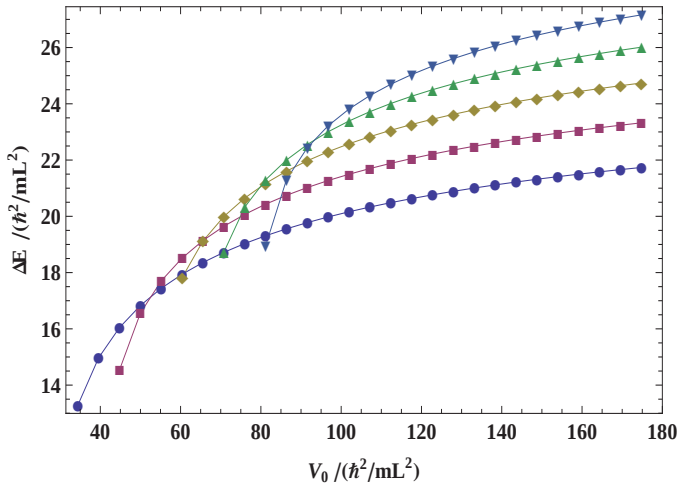

Figure 3.10: Excitation energy gaps between ground and first-excited states as function of trap depth for 2 (circle), 3 (square), 4 (diamond), 5 (upright triangle), and 6 (invert triangle) sodium atoms. Trap size is 5 μm.

Ideally, the path connecting the starting point and a targeted Fock state consists of a series of states (the Bethe ansatz states) with well-defined particle numbers. But in reality, there are always some *elementary excitations*, which are defined here as any deviations from the ideal adiabatic course. Possible elementary excitations include occupations of excited Bethe ansatz state (of the same particle number), earlier ionizations (loss of particles before reaching the Bethe ansatz ionization threshold), and simultaneous ionizations of more than one particles.

We now analyze the effects of excitations. Abrupt changes in the trapping potential tend to introduce extra terms into the system density matrix. As the system gets near an ionization threshold, the system becomes particularly

delicate, since the particle with the highest energy can tunnel further away from the center of the trap and thus external disturbances have larger exciting effects on the system. Moreover, immediately after the ionization threshold is passed, the system density matrix is subject to various excitations due to wave-function collapses. These excitations are crucial to the fidelity of Fock state production, since they cause significant reversion in the number uncertainty of the final state. A characteristic measurement of tendency of excitation is the *energy gap*, Δ, which is defined as the difference between total energies of the ground and first-excited Bethe ansatz states (if both exist). According to our calculation, they are of the order of a few $k_B \times 10$nK (see Figure 3.10). Δ limits the laser culling process in two folds. Firstly, the temperature must be maintained lower than a few 10nK, otherwise, fidelity could be endangered due to thermal excitation. Secondly, the energy gap puts a requirement on the adiabaticity condition [2]: the culling speed must be much smaller than $\frac{\Delta^2}{\hbar}$. To give a sense of the numbers, we consider culling with a trapping potential from the ionization threshold of 3 particles down to that of 2 particles at trap size of 5μm and transverse trapping frequency $\omega_\perp = 2\pi \times 150$kHz. According to our calculation, the minimum time required to complete this portion of the culling should be no less than 0.3ms to be considered as adiabatic.

Chapter 4

Conclusion

In conclusion, we studied the Fock states of bosonic and fermionic atoms with an eye on applying these systems to quantum computation.

We considered the system of fermionic atoms in the micro-traps of optical tweezers for quantum computing. We start from N sites and cull to a series of N spin pairs in the ground state of each micro-trap. We then split them into $2N$ sites, each with one atom. Thus, we initialize our $2N$ qubits in an anti-ferromagnetic configuration. $2N$ qubits can be prepared and manipulated by appropriate rotation either individually or collectively. Entanglement operations are implemented by the collisional shift of the two spin states as two micro-traps are brought together. To read out the spin states, each qubit is split into two sites that are spatially resolved, a total of $4N$ sites. The read-out is provided by fluorescent imaging, where each site is either 0 or 1.

We have shown that fermionic lithium atoms can be the basis for ultra-high fidelity quantum logic. This system has the potential to satisfy all of the DiVincenzo criteria and is therefore a promising candidate for quantum computing.

We also calculated the single-particle energies of interacting bosonic atoms using the Bethe ansatz. We predicted the conditions for producing Fock states in ultracold bosonic atoms in 1D optical trap.

Appendices

Appendix A

Controlling laser power, laser frequency, and temperature

Due to the ubiquitous presence of noise and varying surrounding environment, active feedback control systems are pivotal components in an ultracold physics labs. Usually we want to control the parameters, such as laser frequency, lens position, room temperature, liquid level, in a physical process at some preset points. Any deviation from such a setpoint is considered the *locking error*. A feedback control system usually has three functional modules: the module for locking error detection and error signal generation; the module for purifying and amplifying the error signal; and the module that perceives the error signal and accordingly compensates for the locking error to restore the preset value.

In the following sections, we study proportional-integral-derivative (PID) control basics and a few realistic projects that are most relevant to ultracold atomic physics.

A.1 Basics of PID control

A PID control is a generic closed-loop feedback algorithm that is widely used in industrial control systems. The PID controller provides three separate but related feedbacks based on some statistics of the error signal: the proportional value $P(t)$, the integral value $I(t)$ and the derivative value $D(t)$ (see Figure A.1**a**). The overall reaction of the PID controller is a weighed sum of the three feedbacks,

$$R(t) = K_P P(t) + K_I I(t) + K_D D(t), \tag{A.1}$$

where K_P, K_I, and K_D are tunable constants. Finally $R(t)$ is applied to the system via actuators such as piezoelectric stacks, heating elements, etc.

Let $E(t)$ denote the error signal. The proportional feedback, $P(t) \equiv E(t)$, measures the error signal at the present time. Often, the proportional feedback makes the weight-lifting contribution for AC-coupled processes. Larger K_P typically mean more substantial response. However, an excessively large K_P will lead to instabilities and oscillations.

The integral feedback is given as

$$I(t) \simeq K_I \int_{-T}^{t} E(\tau)\, d\tau, \tag{A.2}$$

where $T \geq 0$ is the characteristic cutoff time of the integrating component. $I(t)$ measures the accumulation of the error signal over a certain period of time in the immediate past. The integral feedback collects small yet persistent errors and generate a remedial output. Larger K_I implies steady state errors

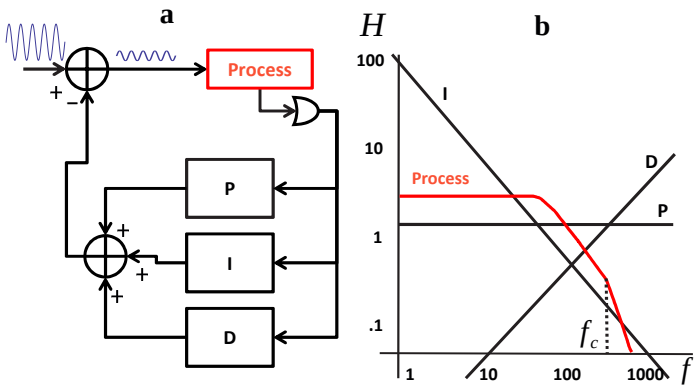

Figure A.1: **a** The PID control flowchart. Arrow denotes direction of control flow. The detector senses fluctuations in the process (red) and sends error signal to the PID controller (labelled as P, I, and D, respectively). The outputs of the PID controller is summed and applied to the process to reduce the fluctuation. **b**. The Bode plots of the transfer functions of the P, I, D control units (black), and the process (red). The latter is assumed to be a two-stage amplifier which starts to roll off at 12dB/octave at frequency f_c [46].

are eliminated more quickly. Since for a sinusoidal signal of frequency ω, $I(t) \propto \frac{1}{\omega}$, integral feedback is inefficient in reducing high-frequency locking-errors. Moreover, since the information collected by the integral feedback is often out-of-date, inappropriately large K_I can cause excessive overshooting.

The derivative feedback, $D(t) = \frac{d}{dt}E(t)$, measures the rate of change of the error signal at the present time. The derivative feedback 'guesses' on the tendency of the near-future error signal based on the measured rate of change and tries to check that tendency with a contravening output. Hence, derivative control is used to reduce the overshoot produced by the integral feedback, at the price of slowing down transient response (lengthening the settling time). Clearly, for a sinusoidal signal with frequency ω, $D(T) \propto \omega$.

Table A.1: Ziegler-Nichols tuning method

Ziegler-Nichols method			
control type	K_P	K_I	K_D
P	$0.5K_c$	-	-
PI	$0.45K_c$	$0.54\ K_c/P_c$	-
PID	$0.60K_c$	$1.20K_c/P_c$	$K_cP_c/13$

Therefore, with sufficiently high loop-gain and large K_D, derivative feedback can lead to oscillations and other instabilities. A common solution is to use low-pass filters to safeguard against the build-up of high-frequency noise. The spectral response of the three feedback controls and a typical system transfer functions are shown in Figure A.1**b**.

It should be clear by now that even with the world best PID controller, substantial tuning is required to harness it to do good. As shown in Figure A.2, overall transfer function of the PID controller is calculated and the product of the transfer functions of the process and the PID controller gives the loop transfer function. The transfer functions of the other components including the detector, the summer circuits are assumed to be unity. A tuning process fits the PID spectral response to that of the process to produce the desired spectral responses, by adjusting the parameters, K_P, K_I and K_D, to the optimum values.

A widely used tuning method is the Ziegler-Nichols method: with the K_I and K_D set to zero, K_P is increased until it reaches the critical gain, K_c, which is characterized by the onset of oscillation in the process output. K_c and the oscillation period P_c are recorded and used to calculate the optimum

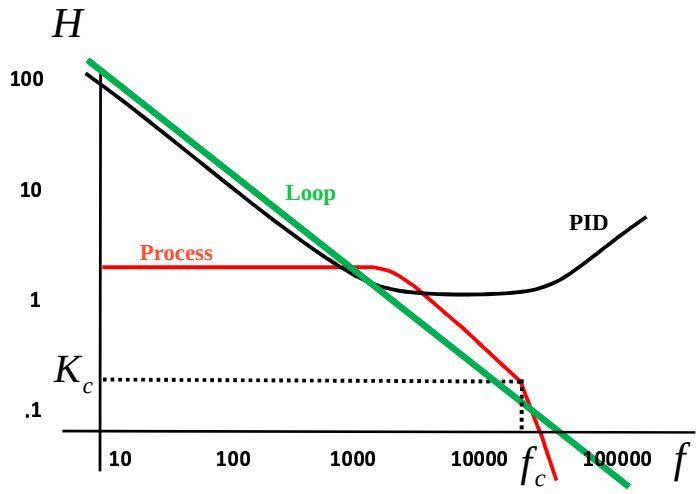

Figure A.2: The Bode plot of the response frequencies of the weighed sum of the P, I, and D control units (black) after the PID tuning. The transfer function of the system is characterized by a two-stage RC-filter (red). Their product gives the overall loop gain, whose Bode plot is shown (green).

values for the PID gain parameters with formulae given Table A.1.

Insights on the above tuning method are made clear in Figure A.2. The critical step in the Ziegler-Nichols tuning method is measuring the values K_c and P_c. If one examines the tuning process carefully, one will be convinced that this just finds the coordinate of the point in the Bode plot where the process transfer function starts to roll off at 12 dB/octave and the phase-shift approaches 180 ° [46]. Because a phase-shift $\sim 180\,^\circ$ would convert a negative feedback to positive. With a high enough gain K_c, a positive feedback with > 1 loop-gain will surely start the oscillation at frequency f_c. Obviously, $P_c = 1/f_c$. After obtaining these two numbers, the rest is straightforward. Depending on the number and types of feedback controls, various optimum values can be

obtained by looking up the above table. Usually, after the tuning, a simple loop-transfer function results. Figure A.1**b** shows a $1/\omega$ transfer function (solid green line).

However, no tuning formula fits all. In practice one should choose a closest tuning method and use it only as a guideline. The ultimate goal is to obtain the desired response.

A.1.1 Feed forwards

PID controllers, when used alone, may perform poorly, *i.e.*, excessive overshoots, oscillations, and/or divergence. And often, one has to improve one feature in the process response function at the price of others. This can be improved by combining a PID controller with a feed-forward controller. Feed-forward is an open-loop control algorithm. With enough knowledge about the system, the next behavior of a system can be successfully anticipated with sufficient accuracy. Accordingly, a preventing measure can be taken, without relying on feedback. An obvious advantage of feed-forward relative to feedback is that it causes no overshooting or transient oscillations. Therefore, the less we rely on feedback, the smaller the overshoots and transient response times are. With the feed-forward, the major portion of the controller output is lifted from the PID feedback which is merely used to respond to the error of the feed-forward and the setpoint. In this way, the overall system performance is substantially improved.

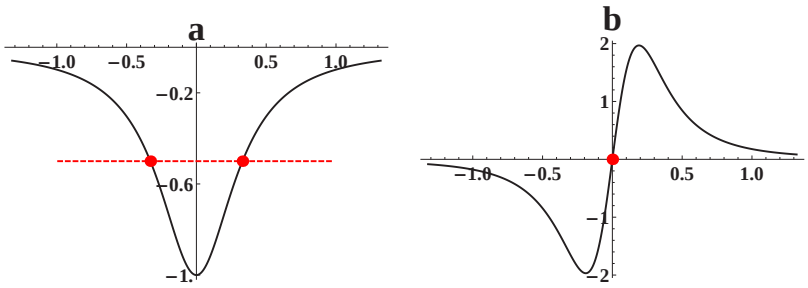

Figure A.3: **a.** Absorption peak as measured by the voltage output of a photodiode. Without using lock-in amplification, the best locking reference level are as shown in the dashed line and the resulted laser frequency is one of the side points (red) of the absorption peak. **b.** The decoded lock-in signal for the absorption peak. With the lock-in amplification, an absolute reference signal at 0 volt can lock laser frequency on the center of the absorption peak.

A.2 Lock-in amplification

A lock-in amplifier is a type of amplifier that can encode and extract a small signal with a known carrier wave in an extremely noisy environment. This is done under the board by a homodyne followed by a narrow-band low-pass filter. In laser spectroscopy, precision control on frequency necessitates the use of lock-in amplifiers to extract small error signals and, more importantly, to lock to the center of an absorption peak, instead of the sides, as will be discussed below.

To see how, consider an absorption peak shown in Figure A.3**a**. Let the laser power after absorption be $I(\omega(t))$, which could be the voltage of a photodiode and where ω is the slowly drifting laser frequency. Without using lock-in amplifiers, the best one can do is to lock laser frequency to one of the two sides of the peak. This has two drawbacks. Firstly, the precision of frequency lock

is entangled with laser power. This is because the photodiode output voltage measures the absolute laser power. If there is power fluctuation, it will appear in frequency fluctuation, by the translation of the locking. Secondly, though locked, the laser frequency may not be exactly known. To obtain the exact laser frequency, we must calculate the peak width. However, the calculation is complicated by various peak broadening effects, *e.g.*, Doppler-broadening, power-broadening, *etc.* [70].

Lock-in technique solves both problems elegantly. Firstly the laser frequency is modulated with a carrier signal, which is usually a sinusoidal function with a clean constant frequency $2\pi f_r$. This modulates the laser intensity $I(\omega(t) + \chi \cos 2\pi f_r t)$. When the modulation amplitude χ is small, we can expand the laser intensity and get

$$I(\omega(t) + \chi \cos 2\pi f_r t) \simeq I(\omega(t)) + I'(\omega(t))\chi \cos 2\pi f_r t, \tag{A.3}$$

where $I'(\omega(t))$ is the derivative of the laser intensity with respect to the laser frequency.

The photodiode signal is sent to the lock-in amplifier, where the signal is homodyned with the carrier signal and subject to a low-pass filter.

$$\begin{aligned} O(\omega(t)) &= \mathrm{LP}\left\{ \left| I(\omega(t)) + I'(\omega(t))\chi \cos 2\pi f_r t + \cos(2\pi f_r t) \right|^2 \right\} \\ &\simeq I'(\omega(t))\chi, \end{aligned} \tag{A.4}$$

where LP stands for the transfer function of the low-pass filter. We have assumed the Fourier component of frequency $2\pi f_r$ in the drifting waveform of the laser frequency is negligible.

The resultant signal $O(\omega(t))$ is the derivative of the absorption peak $I(\omega)$ (see Figure A.3). Within a certain range, $O(\omega(t))$ truthfully reflects the difference between the laser frequency and the absorption center frequency. With help of subsequent PID feedback control, laser frequency is typically locked at the zero-crossing in $O(\omega(t))$ (see Figure A.3).

A.3 Saturated absorption spectroscopy

The Doppler-free, saturated absorption spectroscopy is commonly used to precisely detect errors in laser frequencies. The experimental arrangement for the saturated absorption spectroscopy is shown in Figure A.4. The incident laser beam (with mW power) is split by the beam-splitter BS with power ratio $\approx 1:9$. The less intense beam, called the *probe beam*, passes through the cell and enters the photodiode detector. The more intense beam, called the *pump beam*, traverses the atomic vapor cell in the opposite direction.

Firstly, we consider a single atomic transition with center frequency ω_0 and natural linewidth γ. The absorption probability of a photon with frequency ω by a ground-state atom at rest is

$$\sigma(\omega, \omega_0) = \sigma_0 \frac{\gamma^2}{4(\omega - \omega_0)^2 + \gamma^2}, \tag{A.5}$$

where σ_0 is the on-resonance absorption probability. At room temperature, the velocity distribution of the atoms in the glass cell is

$$N(v) = N_0 e^{-\frac{mv^2}{2k_B T}}, \tag{A.6}$$

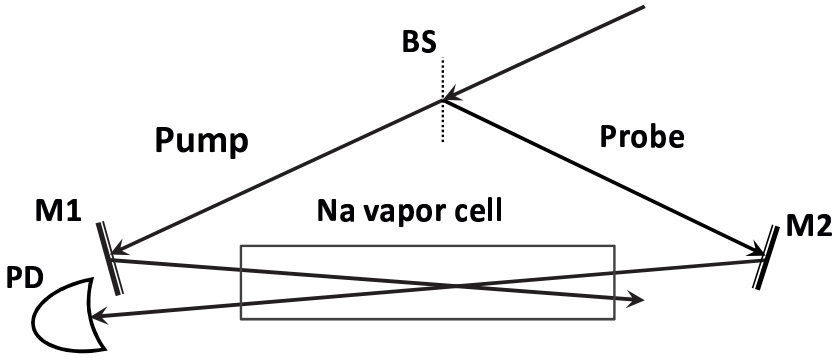

Figure A.4: Experimental set-up for saturated absorption spectroscopy.

where N_0 is the number of atoms at zero velocity, k_B is Boltzmann's constant, and T is the room temperature.

If there is no pump beam, almost all the atomic population would be in ground-state. With the complication of the Doppler-shift (see Section 1.1.1), the absorption peak is given by the convolution between $\sigma(\omega)$ and $N(v)$

$$R(\omega) = \int_{-\infty}^{\infty} \sigma(\omega - kv/c, \omega_0) N(v) d\, v. \tag{A.7}$$

With the intense pump beam, a significant portion of the atomic population whose velocity falls in the following range:

$$|v\omega/c - (\omega - \omega_0)| < \frac{\gamma}{2} \tag{A.8}$$

is pumped to the excited state. The distribution of population in the ground state and the excited state are shown in Figure A.5**a**. Selectively optical pumping atomic population with certain property (velocity in this case) to the excited state is termed 'hole-burning'.

As the laser frequency is scanned, the absorption-effective population of the probe beam and the burnt hole shift oppositely (see Figure A.5). At proper laser frequency, the two oppositely moving peaks overlap. Provably this occurs precisely at zero velocity, where the probe and the pump will compete for absorptions by the low-speed atomic population. Deprived of suitable atomic population to absorb the laser power, the probe beam passes through the cell without much loss of power. This results a peak of linewidth γ in the saturated absorption spectrum for an isolated transition (see Figure A.5**a**).

It is straightforward to see that the saturated absorption spectroscopy of atoms with multiple transitions will have multiple peaks, each of which has the center frequency and natural linewidth of the corresponding transition. However, for atoms with atomic structures of either Figure A.6**a** or **b**, extra peaks can appear.

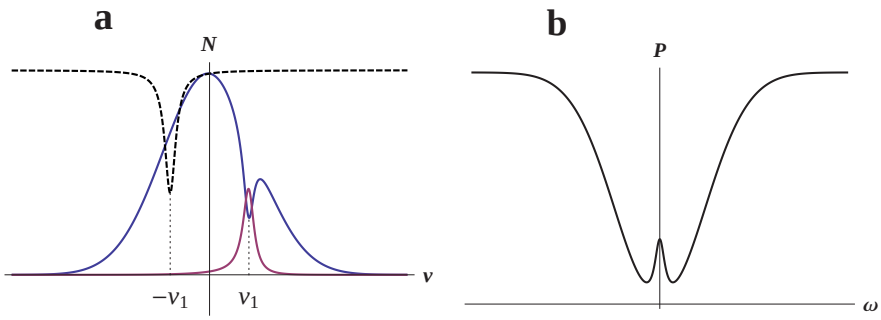

Figure A.5: **a.** Population distribution of the ground state (blue) and the excited state (purple) for a blue-detuned laser frequency. The absorptions distribution of the probe beam is also shown (dashed). **b.** The saturated absorption spectroscopy for an isolated transition. When the peak in the dashed line and the burnt hole aligns at $v = 0$, a peak appears.

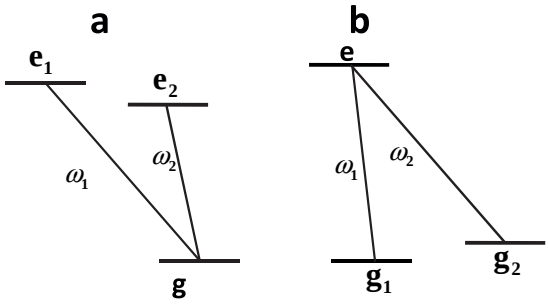

Figure A.6: **a.** Two transitions sharing one ground state. **b.** Two transitions sharing one excited state.

We take Figure A.6**a** for example. If the two transitions at frequencies ω_1 and ω_2 are close enough, both can fall in the frequency range specified by Equation (A.8). Consequently, two holes can be burnt in the population distribution, and both transitions at ω_1 and ω_2 can contribute to the absorption of the probe beam. Figure A.7**a** shows this situation. There are three possible alignments between the absorption peaks of the probe beam and the two burnt holes. Particularly, when the laser frequency is close to $\frac{\omega_1+\omega_2}{2}$, the two absorption peaks and the two burnt holes overlap. This causes the following effects: the atomic transition at ω_1 pumps atomic population with velocity $v_1 \approx v_2 \approx c\frac{\omega_2-\omega_1}{\omega_1+\omega_2}$ to excited state $|e_1\rangle$; at the same time the atomic transition at ω_2 pumps atomic population with velocity $-v_1$ to excited state $|e_2\rangle$. As a result, absorptions of the probe beam at both transitions are blocked and the power loss in the probe beam is reduced twice as strongly. That is, an extra peak at the frequency $\frac{\omega_1+\omega_2}{2}$ appears in the saturated absorption spectroscopy and it is referred to as the *crossover line* (Figure A.7**b**).

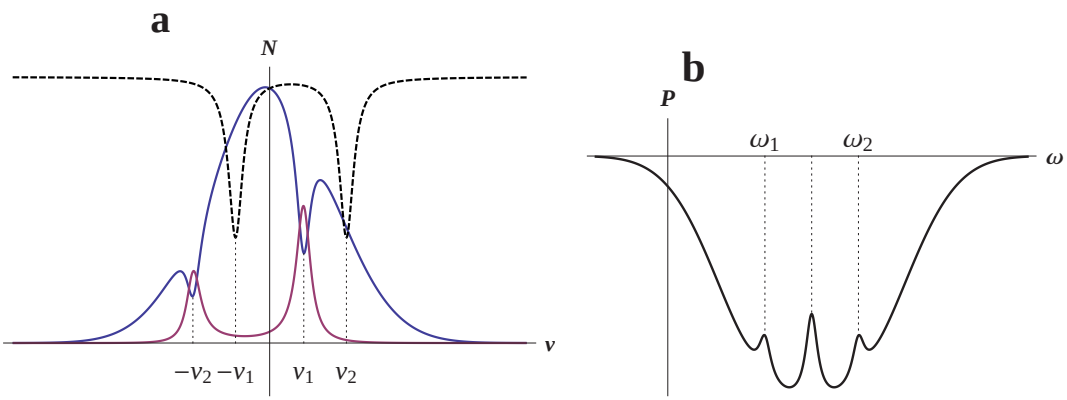

Figure A.7: **a.** Population distribution of the ground state (blue) and the excited state (purple) The absorption distribution of the probe beam has two peaks corresponding to the two transitions ω_1 and ω_2 (dashed). **b.** The saturated absorption spectroscopy for an isolated transition.

A.4 Frequency controls in a semiconductor diode laser

Due to their high-quality mode, tunable frequency, stable power, and low price, semiconductor diode lasers find many applications in laser cooling and trapping experiments. However, a bare laser diode is not a useful laser source with single-frequency and high-quality mode, unless it is wrapped in sophisticated conditioning infrastructure. The infrastructure provides electric current control, temperature control, frequency stabilization and tunability, *etc.* One popular design is the Littrow configuration.

The infrastructures of the Littrow configuration is usually housed in a sealed resin or metal case, for easy control of temperature and humidity. At the heart of this configuration is a diffraction grating (see Figure A.8) which splits the incident power into zeroth-order (about 90% of the incident laser power)

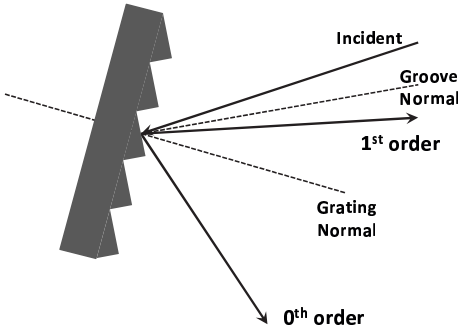

Figure A.8: Diffraction grating used in Littrow configuration for use in a semiconductor diode laser.

and first-order diffraction beams. The first-order beam is directed back into the laser diode. The grating and the back facet in the laser diode thus form an external cavity. With the huge spectral resolution capability of the diffraction grating, the reflection angle of the first-order diffraction beam is very sensitive to the incident laser frequency. As a result, the output laser frequency can be controlled by tilting the grating. By actively controlling this tilting angle, one can accurately control the frequency of the output laser beam to within ± 2 MHz.

Usually, the detection of frequency error is realized through saturated absorption spectroscopy (see Section A.3). Lock-in amplifiers are used to accurately determine the center of the peaks in the absorption spectrum, and the integral control algorithm is enough for fast frequency locking.

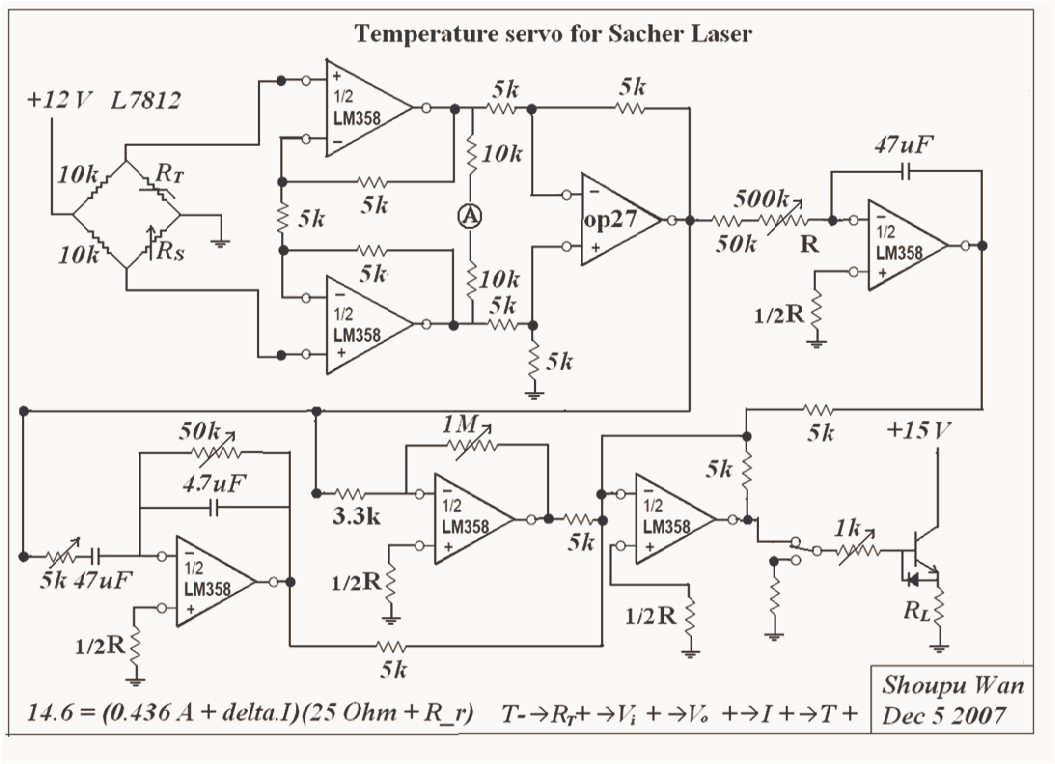

Figure A.9: PID temperature control servo circuit. Starting from upper left are 1) a bridge with a thermistor on one of the 4 arms, error signal generation unit, 2) differential amplifier, error signal filtering and amplifying unit, 3) integral, derivative, and proportional feedbacks, 3) heater, actuator, respectively.

A.5 Temperature Control

The lasing frequency and mode quality of a semiconductor diode laser is very temperature-sensitive. For a common laser diode, the laser wavelength tunes by 0.1 nanometer when temperature changes by 1/4 Kelvin and mode quality deteriorates quickly, too.

To have a reliable laser source, several stages of temperature stabiliza-

tions are needed. Firstly, the laser diode itself must be stabilized to reduce fast temperature fluctuation (with frequencies of a few kHz). Secondly, to reduce warm-up time for day-by-day uses, another stage of temperature control is needed to pin down the temperature of a larger environment, *e.g.*, the platform or baseplate of the Littrow infrastructure. The circuit diagram in Figure A.9 is a broadband temperature stabilization servo module designed for semiconductor diode. With a properly tuned feedback loop, the servo can stabilize the temperature of a diode laser within 10 minutes and extend the duration of locking to about 10 hours without interruption.

A.6 Laser power control

In many applications, one needs to control the fluctuation in the laser power. This becomes important, for example, during entanglement generation and gate operation using stimulated Raman transition where precision control of Rabi oscillation frequency is necessary.

However, the resonance frequency is very sensitive to the laser power of Raman laser beams, due to the notorious light-shift (Equation (1.4)). Therefore, precisely controlling the powers of the Raman laser beams is critical.

More often than not, there are many conditioning optics before the laser is finally delivered into the chamber and among them many are polarizing devices (not necessarily polarizers). To make it worse, laser beams are frequently coupled in and out of optic fibers. As is well-known, significant polarization rotations occur because of optical waveguide bending. The combined effect is

a wild laser power fluctuation.

An active feedback loop can greatly reduce the power fluctuation. One way to do so is to skim the noisy part out of the laser power by power-splitting components such as an electro-optical modulator (EOM).

An EOM consists of two polarizers sandwiching one, sometimes two birefringent crystal(s), such as Lithium niobate. The crystal is cradled in a transverse static electric field created by a pair of electrodes. A laser beam is incident on the input polarizer, passes through the crystal and finally exits the output polarizer. The input polarization is properly oriented with respect to the crystal axes, so that the optical power can be equally split into the ordinary and extraordinary beams in the crystal. With an applied voltage, a variable phase delay can be produced between the ordinary and extraordinary beams. Upon exiting the crystal, the two beams recombine into one, but the polarization of the resultant beam is changed because of the phase delay. As a result, the output polarizer will split off a certain amount of laser power, depending on the phase-delay.

By controlling the phase-delay with a voltage on the electrodes, one can control the transmitted laser power. With a closed-loop feedback system, the noisy part of the laser power can be skimmed away, leaving clean laser power in the chamber. The schematic of the power stabilization system is shown in Figure A.10**a**. The feedback control circuit is shown in the panel **b** of the same figure.

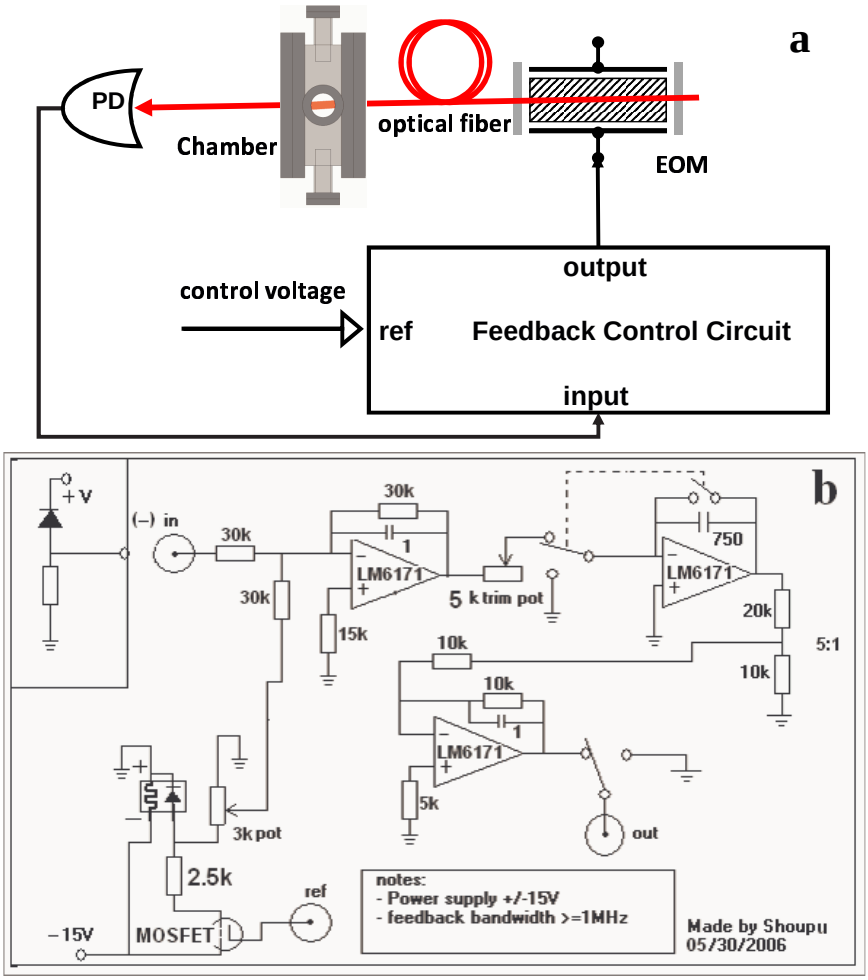

Figure A.10: A laser power stabilization system **a** The schematic drawing for the feedback loop. The laser power in the chamber is the control object. The laser power exiting the vacuum chamber is detected by a photodiode. The difference between the output voltage and a preset voltage is taken as the error signal. This error signal is amplified and conditioned in the feedback control circuit. Finally, the circuit outputs a voltage to adjust the laser power dissevered to the chamber. **b** The feedback control circuit. The reference voltage is generated by a temperature-stabilized zener diode. A simple integral control is used. All electronic components in the feedback loop are of high bandwidth so that the overall signal has a bandwidth ≥ 1 MHz.

Appendix B

Issues Related to Bethe Ansatz

B.1 Truncations on the boundary conditions in Bethe ansatz method

In Section 3.4, we implicitly truncated boundary conditions. We can obtain more equations by joining wavefunctions at boundaries other than those between R_1, R_2 and R_3 but we did not. In fact, we just considered the cases with no more than one particle in the barrier regions. There are more several reasons, but the most important one is that we got just enough equations to derive the secular equations (3.24) and (3.25). On the other hand, had we included more equations, we would have got inconsistencies and the Bethe ansatz method would not bear any solutions. For this reason, we admit that our method is an approximation.

The inconsistency results partly from the finite barrier. To understand this point, note that there are more than one ways of partitioning N (> 1) atoms into the two groups. For example, we can have $0, 1$, or 2 atoms in the barrier while the rest are in the well, respectively. With the finite square well, each partition corresponds to a realizable configuration by placing one group to in the well and the other in the barrier (either left or right). Recall that the interaction energy is proportional to the particle number in the well, from

the discussion of the perturbation solution in Section 3.3 (Equation (3.10)). Thus, each partition has a different interaction energy. In reality, the quantum state of the system could be a simultaneous superposition of all these partitions. However, under the current formulation framework, this cannot be possible—all the different partitions have different energies! We refer to this inconsistency as the *inhomogeneous interaction difficulty*.

Next we illustrate the inhomogeneous interaction difficulty with a interacting two-atom system. The configuration space x_1-O-x_2 is partitioned into various regions by the boundaries where particle-particle interactions take place and the square well potential steps (see Figure B.1). The Bethe ansatz wavefunctions in these regions consist of linear superpositions of plane waves and/or exponentially decaying waves. If one follows the procedure outlined in section 3.4 in the regions 1, 2, 3, and 4 and boundary conditions BC(1,3), BC(1,2), and BC(1,4) (see Figure B.1), one would soon rediscover Equation (3.24) (with $N = 2$).

But this time, we go beyond that. We continue to dig more equations out of other boundary conditions and eventually derive another set of secular equations to be contrasted with Equation (3.24). Let us first write out the wavefunctions in regions 4, 5 and 7,

- Region 4,

$$\phi_4(x_1, x_2) = A_p e^{ik_1 x_1 + \kappa_2 x_2} + A_m e^{-ik_1 x_1 + \kappa_2 x_2} + \\ + B_p e^{ik_2 x_1 + \kappa_1 x_2} + B_m e^{-ik_2 x_1 + \kappa_1 x_2}, \tag{B.1}$$

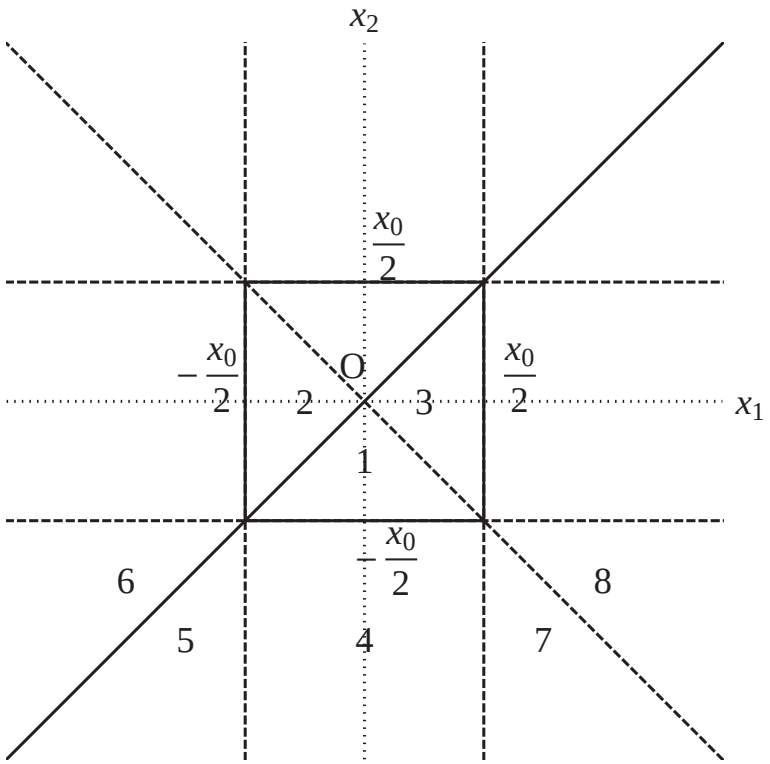

Figure B.1: Configuration space and boundary conditions for a 2-boson system. The perpendicular dotted lines, x_1 and x_2, are the coordinate axes. The solid lines at $x_{1,2} = \pm\frac{x_0}{2}$ denotes the square well enclosed by potential barrier. The solid diagonal line $x_1 + x_2 = 0$ denotes where δ-interaction takes place; the anti-diagonal line $x_1 - x_2 = 0$ (dashed) denotes the additional space-reflection symmetry. The other dashed lines are boundaries for the problem. The numbers 1-8 denote the regions that have distinct forms of wavefunctions where regions 1 & 2, 1 & 3, 5 & 6, and 7 & 8 are related by space-reflection symmetry, respectively.

- Region 5,

$$\phi_5(x_1, x_2) = A_5 e^{\kappa_1 x_1 + \kappa_2 x_2} + B_5 e^{\kappa_2 x_1 + \kappa_1 x_2}, \tag{B.2}$$

- Region 7,

$$\phi_7(x_1, x_2) = A_7 e^{-\kappa_1 x_1 + \kappa_2 x_2} + B_7 e^{-\kappa_2 x_1 + \kappa_1 x_2}. \tag{B.3}$$

Then we explicitly derive the boundary conditions below:

1. BC(4,5) ($x_1 = -x_0/2,$ and $x_2 < -x_0/2$),

   Combine continuity of both wavefunction and first-order derivative,

$$(k_1 - i\kappa_1) A_m e^{ik_1 x_0} = (k_1 + i\kappa_1) A_p, \tag{B.4}$$

$$(k_2 - i\kappa_2) B_m e^{ik_2 x_0} = (k_2 + i\kappa_2) B_p. \tag{B.5}$$

2. BC(4,7) ($x_1 = x_0/2,$ and $x_2 < -x_0/2$),

   Similar to BC(4,5),

$$(k_1 - i\kappa_1) A_p e^{ik_1 x_0} = (k_1 + i\kappa_1) A_m, \tag{B.6}$$

$$(k_2 - i\kappa_2) B_p e^{ik_2 x_0} = (k_2 + i\kappa_2) B_m. \tag{B.7}$$

Here A_p, A_m, B_p, and B_m are superposition coefficients in region 4 and the superposition coefficients $A_{5,7}$ and $B_{5,7}$ have been eliminated. Again we truncate our process, since we have enough equations for demonstrating the inconsistency. Combining Equation (B.4) and (B.6), Equation (B.5) and (B.7), we obtain another set of secular equations,

$$e^{2ik_j x_0} = \left(\frac{k_j + i\kappa_j}{k_j - i\kappa_j}\right)^2, \; j = 1, 2, \tag{B.8}$$

which describes essentially *non-interacting* bosons in the same square well. Obviously, Equation (3.24) and Equation (B.8) are irreconcilable unless $c = 0$. So generally speaking, the problem of δ-function bosons in finite-barrier square well potential has no solution in the framework of Bethe ansatz. Equation (3.24) and Equation (B.8) are irreconcilable as long as partitions with different particle numbers exist in the configuration space. These arguments can be easily extended to an arbitrary number of bosons. *i.e.* when the probability for $m > 1$ particles to tunnel simultaneously into the barrier of the square well is small compared with that for $m = 0, 1$, the Bethe ansatz solution may be taken as a sufficiently good approximation. From our calculation we learned that, away from the strongly interacting region, single particle energy levels cluster. Unless all the levels are deeply seated in the trap, the probability for more than one particle to simultaneously get outside of the square well is comparable with that of the most energetic particle.

Therefore, we conclude that because of the inhomogeneous interaction difficulty, Bethe ansatz method cannot give exact solutions to the interacting many-boson problem in general. However, for the purpose of Fock states simulations, this approximate method is sufficient. The energy spacings between single-particle levels are big near the strong interaction regime where Fock-state experiments will likely take place. Therefore, the probability for more than one particles to tunnel into the barrier of the square well is small, compared with no tunnelling or one tunnelling.

B.2 Valid Bethe ansatz solutions

We work with the $L-$scaling scheme (see Section 3.2). The secular equations (3.25) depend on the interaction strength, the trap depth, and a set of integers. Clearly, the interaction strength and trap depth can assume the values of any positive real numbers. The purpose of this section is to study what are good sets of integers to be used in the secular equations (3.25), to obtain physically meaningful solutions.

Firstly, recall that in Section 3.3, we got the solutions for many-boson systems for a few special cases by simply using textbook methods, perturbation theory, and variational principle. Those solutions are either experimentally verified or corroborated by other theories, and thus are trustworthy. Now, we show how to use those trustworthy solutions to inspect the Bethe ansatz solutions.

Let us once more take a 4-particle system for example. We assume $k_0 = 10$ for the trap. For the mere purpose of obtaining a solution, we plug $\{0, 1, 2, 3\}$ into the secular equations (3.25) with some small interaction strengths in the weak regime. The wave numbers of the solutions are shown in Figure B.2. As we insert more and more points, we expect to see the solutions form continuous paths connecting solutions at some finite interaction strengths to that of $c = 0$. However, we know the solutions for the case of $c = 0$ with the previously mentioned methods and we can simply compare that to the end of the continuous path—if they do not match, the solutions on the whole path are invalid. The three other panels in Figure B.2 show more of

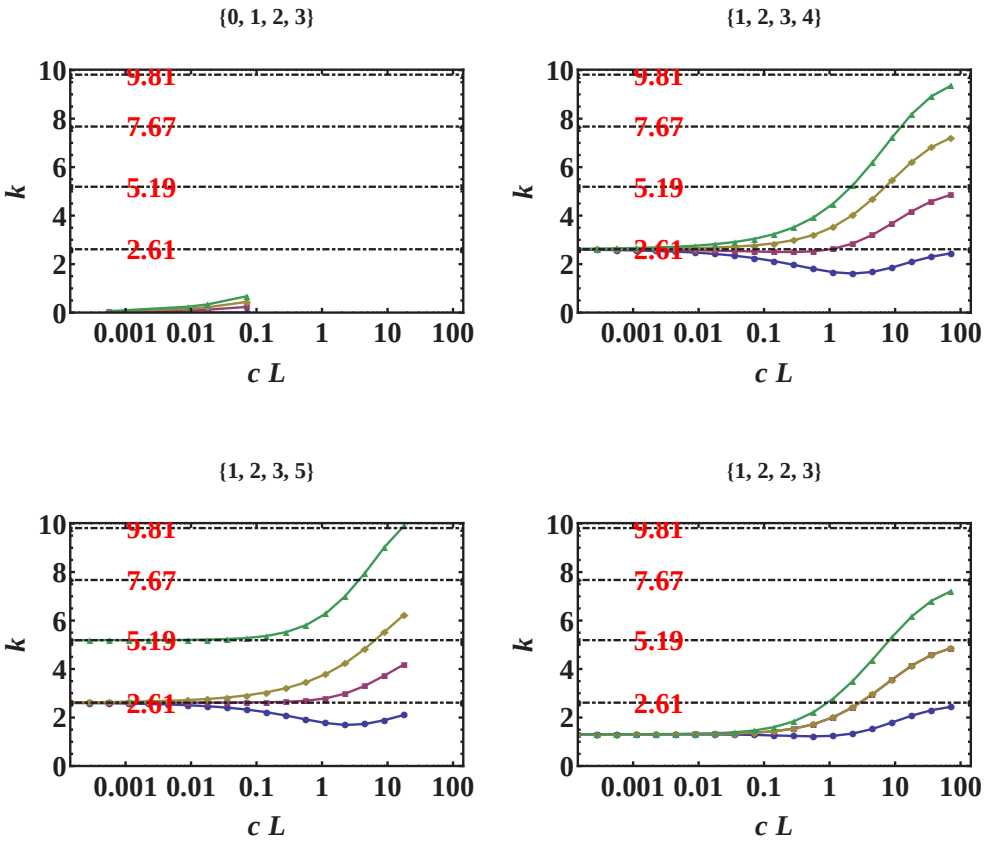

Figure B.2: Verification of the Bethe ansatz solutions using solutions at $c = 0$. The title of each panel denotes the quantum numbers that are used for the calculation; the horizontal axis denotes the interaction strengths; the vertical axis denotes the wave numbers of the Bethe ansatz solutions. The red bold numbers together with the dotdashed lines in each panel denotes the wave numbers of the solutions at $c = 0$. The quantum numbers $\{0, 1, 2, 3\}$ and $\{1, 2, 2, 3\}$ denote states that have no valid limit as $c \to 0$.

the trials with the integer sets $\{1, 2, 3, 4\}$, $\{1, 2, 3, 5\}$, and $\{1, 2, 2, 3\}$, among which, the integer sets, $\{0, 1, 2, 3\}$ and $\{1, 2, 2, 3\}$, should both be rejected.

This method can be generalized to any many-particle system with any trap depths and interaction strengths. A 'promising solution' to Equation (3.25) should be connected to valid solutions at $c = 0$. If this path does not connect to a valid solution at $c = 0$, then we can decide with certainty that the chosen integer set is bad. Our non-exhaustive experiments show that a Bethe ansatz solution is connected to a solution at $c = 0$ if and only if the set I consists of positive and mutually distinct integers, as shown in Figure B.2. We also find that for $c \neq 0$, the wave numbers in the solution are mutually distinct if and only if the integers in the set I are mutually distinct.

B.3 Energy-level ordering of Bethe ansatz states

With the verification process explained in Appendix B.2, we know that only positive, mutually distinct integers can be supplied to Equation (3.25). However it is still left to determine which integer set gives the ground state, which gives the first excited state, and so on.

In this section, we use a similar method as what is used in the previous section to partially order the levels. This time, our clue comes from the solutions in the strong interaction limit $c \to \infty$. In that case, the ground state of the many-boson system is similar to that of a degenerate-fermion gas because of the boson-fermion correspondence principle [37]. Our numerical calculations show that with the set $I = \{1, 2, \cdots, N\}$, the solution of Equation (3.25) ap-

proaches that of the ground state of the degenerate fermion system in the limit $c \to \infty$. We therefore expect that for finite c, the ground state is also obtained with this same set. Knowing that $I = \{1, 2, \cdots, N\}$ generates the ground state, it is almost intuitive to see that $I = \{1, 2, \cdots, N-1, N+1\}$ will generate the first-excited state. Indeed, experiments with this set of integers for all interaction strengths support this viewpoint.

We are thus certain about the ground and first-excited states in general. However, little could be said beyond that. Within the limit of calculation error, our experiment is not conclusive about which is the second excited state for all interaction strength. As shown in Figure 3.3, there are crossovers in the total energies at some interaction strengths and trap depths. In general the energy-level ordering depends on both the largest quantum number and the total of the quantum numbers. For complete ordering, one needs something analogous to Hund's Rule in atomic physics. But for the purpose of applications in producing Fock states, it suffices to know the energy levels of the ground and first-excited states.

To summarize, we conclude that for any given N, the set $I = \{1, 2, \cdots, N\}$ leads to the ground state and the set $I = \{1, 2, \cdots, N-1, N+1\}$ to the first excited state. However, a general rule for ordering all the energy levels at arbitrary interaction strength is neither simple nor necessary.

Appendix C

The Wentzel-Kramers-Brillouin (WKB) method

Generally, the WKB theory is a method for approximating the solution of a differential equation whose highest-order derivative is multiplied by a small parameter in comparison with other variables [23]. As a semiclassical approximate calculation in quantum mechanics, the WKB method is a very efficient method to solve single-particle eigen-problems in a one-dimensional potential. In this section, we use this method to solve the problem of an atom trapped in a truncated harmonic trap and compare the result to a harmonic oscillator with the same trapping frequency.

Let us modify the notation of Section 2.2.1 a little bit and denote the truncated trap size as z_t (where it was originally denoted as z). The notation for truncation energy is still denoted as E_t (see Figure C.1). At the same time, we denote the distance between the classical turning points as z and the energy of the atom as E. We assume $E < E_t$, which also implies that $z < z_t$.

The Schrödinger equation of an atom in such a trap is

$$\left[\frac{-\hbar^2}{2m}\frac{d^2}{dx^2} + V(x)\right]\Psi(x) = E\Psi(x), \tag{C.1}$$

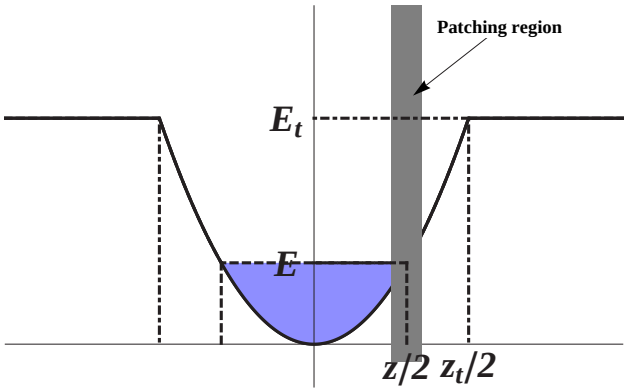

Figure C.1: The trapping potential used for the WKB calculation. For $|x| \leq z_t/2$, the trap is parabolic; for $|x| > z_t/2$, the trap is assumed to be flat. The truncation energy E_t, truncated trap size z_t, atom energy E and classical turning point $z/2$ are as shown. A patching region (gray rectangle)is constructed around the turning point.

where

$$V(x) = \begin{cases} \frac{1}{2}m\omega^2 x^2 & , \quad |x| < z_t \\ \\ \frac{1}{2}m\omega^2 {z_t}^2 & , \quad |x| > z_t \end{cases} \tag{C.2}$$

To the first order following the WKB approach [38], the space can be partitioned into the classical regions, where classically the particle may present, and the quantum regions, where classically the particle is forbidden to enter. In the classical region, one can write the wavefunctions as

$$\Psi(x) = \frac{B}{\sqrt{p(x)}} e^{\frac{i}{\hbar}\int^x p(x')dx'} + \frac{C}{\sqrt{p(x)}} e^{-\frac{i}{\hbar}\int^x p(x')dx'}, \tag{C.3}$$

and in the quantum region,

$$\Psi(x) = \frac{A}{\sqrt{|p(x)|}} e^{\frac{1}{\hbar}\int^x |p(x')|dx'} + \frac{D}{\sqrt{|p(x)|}} e^{-\frac{1}{\hbar}\int^x |p(x')|dx'}, \tag{C.4}$$

where

$$p(x) = \sqrt{2m\left(E - V(x)\right)} \tag{C.5}$$

We classify the wavefunctions as either symmetric or antisymmetric under space reflection about the origin. In this way, we can concentrate on the half-space $x > 0$ only. Around the classical turning points $x = \pm z/2$, both wavefunctions, Equation (C.3) and Equation (C.4), become singular because

$$\lim_{x \to z/2} p(x) \to 0. \tag{C.6}$$

To get over the divergence difficulty, we build the so-called *patching region* (Figure C.1): it wraps the turning point and overlaps on the left with the classical region and on the right with the quantum region. In other words, the turning point is cushioned from both the classical and quantum region by the patching region.

It is known that the wavefunction of a particle in a linear-potential is a superposition of the Airy functions [58]. Therefore, the so-called *patching wavefunction* can be expressed as

$$\Psi(x) = aAi(\alpha(x - z/2)) + bBi(\alpha(x - z/2)), \tag{C.7}$$

where $\alpha^{-1} = \left(\frac{2m}{\hbar^2}V'(0)\right)^{\frac{1}{3}}$ is the scaling length and

$$\mathrm{Ai}(\alpha x) = \frac{1}{\pi}\int_0^\infty \cos\left(\frac{t^3}{3} + \alpha x t\right)\, dt, \tag{C.8}$$

$$\mathrm{Bi}(\alpha x) = \frac{1}{\pi}\int_0^\infty \left[\exp\left(-\frac{t^3}{3} + \alpha x t\right) + \sin\left(\frac{t^3}{3} + \alpha x t\right)\right] dt \tag{C.9}$$

are the Airy functions [58].

There are two useful asymptotic forms of the Airy functions when $|x| \gg 1$: when $x < 0$,

$$\mathrm{Ai}(x) \sim \frac{\sin(\frac{2}{3}(-x)^{3/2} + \frac{1}{4}\pi)}{\sqrt{\pi}\,(-x)^{1/4}}, \tag{C.10}$$

$$\mathrm{Bi}(x) \sim \frac{\cos(\frac{2}{3}(-\alpha x)^{3/2} + \frac{1}{4}\pi)}{\sqrt{\pi}\,(-x)^{1/4}}; \tag{C.11}$$

when $x > 0$,

$$\mathrm{Ai}(x) \sim \frac{e^{-\frac{2}{3}(x)^{3/2}}}{2\sqrt{\pi}\,(x)^{1/4}}, \tag{C.12}$$

$$\mathrm{Bi}(x) \sim \frac{e^{\frac{2}{3}(x)^{3/2}}}{\sqrt{\pi}\,(x)^{1/4}}; \tag{C.13}$$

The Airy functions Ai and Bi approach their asymptotic forms much more quickly than it seems. As a matter of fact, the asymptotic forms in the limits of $\pm\infty$ differ from the Airy function $Ai(x)$ by 1% at $x = 4.57, -1.30$, respectively.

To proceed with the WKB calculations, we assume the existence of the patching region with the following two properties:

1. The patching region is so *thin* that the trapping potential can be linearized in the entire region with sufficient precision;

2. The patching region is so *thick* that the turning point is deeply embedded from both sides and the asymptotic forms are accurate enough approximations before x leaves the patching region.

After all the elaborate discussions about the patching region and the patching wavefunctions, we use them only as a bridge. We splice the asymptotic forms of the patching wavefunction with the quantum wavefunction on the right side, that is, we require that the two become identical in the limit $x \to \infty$. Similarly, we splice the asymptotic forms of the patching wavefunction with the classical wavefunction on the left side. After some algebraic manipulation by eliminating everything about the patching wavefunction, we get the following relationship between the classical and the quantum wavefunctions:

$$A = 0, \tag{C.14}$$

$$\frac{B}{\sqrt{\hbar\alpha}} = -ie^{i\pi/4}D, \tag{C.15}$$

$$\frac{C}{\sqrt{\hbar\alpha}} = ie^{i\pi/4}D. \tag{C.16}$$

The wavefunction can now be written as

$$\Psi(x) = \begin{cases} \frac{2D}{p(x)} \sin\left[\frac{\pi}{4} + \frac{1}{\hbar}\int_x^{z/2} p(x')dx'\right] & |x| < z/2 \\ \\ \frac{D}{p(x)} \exp\left[-\frac{1}{\hbar}\int_{z/2}^{x} p(x')dx'\right] & |x| > z/2 \end{cases} \tag{C.17}$$

Now recall that we required the wavefunctions be either symmetric or anti-symmetric under space reflection about the origin. This is equivalent to requiring that the wavefunction in Equation (C.17) satisfy $\Psi(0) = 0$ (even) or $\Psi'(0) = 0$ (odd), respectively. As can be easily verified, these quantization conditions lead to the eigen-energies $E = (n + \frac{1}{2})\hbar\omega$. That is right! It is the same as a simple harmonic oscillator with identical trapping frequency.

Now it is time for us to examine our assumptions made about the patching region. After all, we may have assumed too much—the two properties

of the patching region are self-conflicting. Provably, the possibility for the existence of such a region diminishes as the truncation energy approaches the ground state energy $\hbar\omega/2$. Therefore, WKB is a valid method to calculate the energy and wavefunction of the ground state of the truncated harmonic trap only if $z_t \gg a \equiv \sqrt{\hbar/m\omega}$.

Bibliography

[1] E.R.I. Abraham, W.I. McAlexander, J.M. Gerton, and R.G. Hulet. Singlet s-wave scattering lengths of ^{6}li and ^{7}li. *Phys. Rev. A*, 53, 1996.

[2] Y. Aharonov and J. Anandan. *Phys. Rev. Lett.*, 58:1593, 1987.

[3] M. H. Anderson, J. R. Ensher, M. R. Matthews, C. E. Wieman, and E. A. Cornell. Observation of Bose-Einstein condensation in a dilute atomic vapor. *Science*, 269:198, 1995.

[4] E. Andersson and S.M. Barnett. *Phys. Rev. A*, 62:052311, 2000.

[5] M.R. Andrews, C.G. Townsend, H.-J. Miesner, D.S. Durfee, D.M. Kurn, and W. Ketterle. *Science*, 275:637, 1997.

[6] J.S. Bell. On the Einstein-Podolsky-Rosen paradox. *Physics (U.S.)*, 1(3):195, 1964.

[7] C.H. Bennett, G. Brassard, C. Crepeau, R. Jozsa, A. Peres, and W.K. Wootters. Teleporting an unknown quantum state via dual classical and Einstein-Podolsky-Rosen channels. *Phys. Rev. Lett.*, 70(13):1895, 1993.

[8] S. Bergamini, B. Darquié, M. Jones, L. Jacubowiez, A. Browaeys, and P. Grangier. Holographic generation of micro-trap arrays for single atoms

using a programmable phase modulator. *J. Opt. Soc. Am. B*, 21:1889, 2004.

[9] H.A. Bethe. *Zeitschrift für Physik*, 71:205, 1931.

[10] J. Beugnon, C. Tuchendler, H. Marion, A. Gaëtan, Y. Miroshnychenko, Y.R.P. Sortais, A.M. Lance, M.P.A. Jones, G. Messin, A. Browaeys, and P. Grangier. Two-dimensional transport and transfer of a single atomic qubit in optical tweezers. *Nature Phys.*, 3:696, 2007.

[11] R. Blatt and D. Wineland. Entangled states of trapped atomic ions. *Nature*, 453:1008, 2008.

[12] I. Bloch. Quantum coherence and entanglement with ultracold atoms in optical lattices. *Nature*, 453:1016, 2008.

[13] S. N. Bose. Plancks gesetz und lichtquantenhypothese. *Z. für Physik*, 26:178, 1924.

[14] Dik Bouwmeester, Jian-Wei Pan, Klaus Mattle, Manfred Eibl, Harald Weinfurter, and Anton Zeilinger. Experimental quantum teleportation. *Nature*, 390(11):575, Dec 1997.

[15] C. C. Bradley, C. A. Sackett, J. J. Tollett, and R. G. Hulet. Evidence of Bose-Einstein condensation in an atomic gas with attractive interactions. *Phys. Rev. Lett.*, 75:1687, 1995.

[16] L. Brillouin. *J. Appl. Phys.*, 22:334, 1951.

[17] L. Brillouin. *J. Appl. Phys.*, 22:338, 1951.

[18] G. Chen, D.A. Church, B.-G. Englert, C. Henkel, and B. Rohwedder. *Quantum Computing Devices: Principles, Designs, And Analysis*. Chapman and Hall/CRC Press, Boca Raton, 2006.

[19] S. Chu, J.E. Bjorkholm, A. Ashkin, and A. Cable. Experimental observation of optically trapped atoms. *Phys. Rev. Lett.*, 57:314, 1986.

[20] S. Chu, L. Hollberg, J.E. Bjorkholm, A. Cable, and A. Ashkin. Three-dimensional viscous confinement and cooling of atoms by resonance radiation pressure. *Phys. Rev. Lett.*, 55:48, 1985.

[21] C.-S. Chuu, F. Schreck, T.P. Meyrath, J.L. Hanssen, G.N. Price, and M.G. Raizen. Direct observation of sub-poissonian number statistics in a degenerate Bose gas. *Phys. Rev. Lett.*, 95:260403, 2005.

[22] C.-S. Chuu and C. Zhang. Suppression of phase decoherence in a single atomic qubit. *arXiv:quant-ph*, 0906.0083.

[23] Wikipedia contributors. Wkb approximation. *Wikipedia, The Free Encyclopedia*, 2009.

[24] J. Dalibard and C. Cohen-Tannoudji. Laser cooling below the doppler limit by polarization gradients: simple theoretical models. *J. Opt. Soc. Am. B*, 6:2023, 1989.

[25] N. Davidson, H.J. Lee, C.S. Adams, M. Kasevich, and S. Chu. *Phys. Rev. Lett.*, 74:1311, 1995.

[26] K. B. Davis, M. O. Mewes, M. R. Andrews, N. J. van Druten, D. S. Durfee, D. M. Kurn, and W. Ketterle. Bose-Einstein condensation in a gas of sodium atoms. *Phys. Rev. Lett.*, 75:3969, 1995.

[27] A. del Campo and J.G. Muga. Atom fock-state preparation by trap reduction. *Phys. Rev. A*, 78:023412, 2008.

[28] P.M.A. Dirac. *Proc. Roy. Soc. London*, 112A:661, 1926.

[29] D. P. DiVincenzo. The physical implementation of quantum computation. *Fortschritte der Physik*, 48:771, 2000.

[30] L. M. Duan, J. I. Cirac, and P. Zoller. Three-dimensional theory for interaction between atomic ensembles and free-space light. *Phys. Rev. A*, 66:023818, 2002.

[31] A.M. Dudarev, R.B. Diener, B. Wu, M.G. Raizen, and Q. Niu. *Phys. Rev. Lett.*, 91:010402, 2003.

[32] A.M. Dudarev, M.G. Raizen, and Q. Niu. Quantum many-body culling: production of a definite number of ground-state atoms in a Bose-Einstein condensate. *Phys. Rev. Lett.*, 98:063001, 2007.

[33] R. Dumke, M. Volk, T. Müther, F.B.J. Buchkremer, G. Birkl, and W. Ertmer. Micro-optical realization of arrays of selectively addressable dipole

traps: A scalable configuration for quantum computation with atomic qubits. *Phys. Rev. Lett.*, 89:097903, 2002.

[34] M. Gaudin. *Phys. Rev. A*, 24:55, 1967.

[35] M.E. Gehm. *Preparation of an optically-trapped degenerate Fermi gas of ^{6}Li: finding the route to degeneracy.* PhD thesis, Duke University, Durham, 2003.

[36] S. Giorgini, L. P. Pitaevskii, and S. Stringari. Theory of ultracold atomic fermi gases. *Rev. Mod. Phys.*, 80:1215, 2008.

[37] M. Girardeau. *J. Math. Phys.*, 1:516, 1960.

[38] David Griffith. *Quantum Mechanics.* Prentice Hall, 2nd edition, 2003.

[39] R. Grimm and M. Weidemuller. Optical dipole traps for neutral atoms. *arXiv:physics/9902072v1*, 1999.

[40] H. Häffner, C.F. Roos, and R. Blatt. Quantum computing with trapped ions. *Phys. Rep.*, 469:155, 2008.

[41] T. Hänsch and A. Schawlow. Cooling of gases by laser radiation. *Opt. Commun.*, 13:68, 1975.

[42] R. Hanson, L. P. Kouwenhoven, J.R. Petta, S. Tarucha, and L.M. Vandersypen. Spins in few-electron quantum dots. *Rev. Mod. Phys.*, 79:1217, 2007.

[43] Y. Hao, Y. Zhang, J.Q. Liang, and S. Chen. *Phys. Rev. A*, 73:063617, 2006.

[44] D. Hayes, P. S. Julienne, and I. H. Deutsch. Quantum logic via the exchange blockade in ultracold collisions. *Phys. Rev. Lett.*, 98:070501, 2007.

[45] K. Henderson, H. Kelkar, T.C. Li, B. Gutiérrez-Medina, and M.G. Raizen. A Bose-Einstein condensate driven by a kicked rotor in a finite box. *Europhys. Lett.*, 75:392, 2006.

[46] Paul Horowitz and Winfield Hill. *The art of electronics*. Cambridge, UK, 2nd edition edition, 1989.

[47] M. Inguscio, S. Stringari, and C. E. Wieman, editors. *Bose-Einstein Condensation in atomic gases*, volume CXL of *Proceedings of the international school of physics*. IOS Press, 1999.

[48] S. Inoue, S. Machida, and Y. Yamamoto. Squeezing in an injection-locked semiconductor laser. *Phys. Rev. A*, 48:2230, 1993.

[49] S. Inouye, M. R. Andrews, J. Stenger, H.-J. Miesner, D. M. Stamper-Kurn, and W. Ketterle. Observation of Feshbach resonances in a Bose-Einstein condensate. *Nature*, 392:151, 3 1998.

[50] D. Jaksch, H.-J. Briegel, J.I. Cirac, C.W. Gardiner, and P. Zoller. Entanglement of atoms via cold controlled collisions. *Phys. Rev. Lett.*, 82:1975, 1999.

[51] B. E. Kane. A silicon-based nuclear spin quantum computer. *Nature*, 393:133, 1998.

[52] M. Karski, K. Förster, J.M. Choi, W. Alt, A. Widera, and D. Meschede. Nearest-neighbor dectection of atoms in a 1d optical lattice by fluorescence imaging. *Phys. Rev. Lett.*, 102:053001, 2009.

[53] W. Ketterle, D. S. Durfee, and D. M. Stamper-Kurn. Making, probing and understanding Bose-Einstein condensates. In M. Inguscio, S. Stringari, and C. E. Wieman, editors, *Proceedings of the International School of Physics - Enrico Fermi*, page 67. IOS Press, 1999.

[54] H.J. Kimble. The quantum internet. *Nature*, 453:1023, 2008.

[55] T. Kinoshita, T. R. Wenger, and D. S. Weiss. All-optical Bose-Einstein codensation using a compressible crossed dipole trap. *Phys. Rev. A*, 71:011602, 2005.

[56] C. Knoernschild, C. Kim, F.P. Lu, and J. Kim. Multiplexed broadband beam steering system utilizing high speed mems mirrors. *Opt. Exp.*, 17:7233, 2009.

[57] P. Kok, W. J. Munro, K. Nemoto, T. C. Ralph, J. P. Dowling, , and G. J. Milburn. Linear optical quantum computing with photonic qubits. *Rev. Mod. Phys.*, 79:135, 2007.

[58] N.N. Lebedev. *Special functions.* Prentice Hall, 1965.

[59] P. Lett, R. N. Watts, C. Westbrook, and W. D. Phillips. Observation of atoms laser cooled below the doppler limit. *Phys. Rev. Lett.*, 61:169, 1988.

[60] Y.Q. Li. *Phys. Rev. A*, 52:65, 1995.

[61] E. Lieb, T. Schultz, and D. Mattis. *Ann. Phys. (N.Y.)*, 16:407, 1961.

[62] E.H. Lieb and W. Liniger. *Phys. Rev.*, 130:1605, 1963.

[63] M. D. Lukin, M. Fleischhauer, and R. Cote. Dipole blockade and quantum information processing in mesoscopic atomic ensembles. *Phys. Rev. Lett.*, 87:037901, 2001.

[64] M. D. Lukin, S. F. Yelin, and M. Fleischhauer. Entanglement of atomic ensembles by trapping correlated photon states. *Phys. Rev. Lett.*, 84:4232, 2000.

[65] L. Luo, B. Clancy, J. Joseph, J. Kinast, A. Turlapov, and J. E.Thomas. *New J. of Phys.*, 8:213, 2006.

[66] E. Majorana. *Nuovo Cimento*, 9:43, 1932.

[67] O. Mandel, M. Greiner, A. Widera, T. Rom, T. W. Hänsch, and I. Bloch. Controlled collisions for multiparticle entanglement of optically trapped atoms. *Nature*, 425:937, 2003.

[68] J.B. McGuire. *J. Math. Phys.*, 5:622, 1964.

[69] Michael B. Mensky. *Quantum measurements and decoherence, models and phenomenology.* Kluwer Academic Publishers, 2000.

[70] H. J. Metcalf and P. van der Straten. *Laser Cooling and Trapping.* Springer; Corrected edition, New York, 1999.

[71] Todd P. Meyrath. *Experiments with Bose-Einstein Condensation in an Optical Box.* PhD thesis, The University of Texas at Austin, 2005.

[72] T.P. Meyrath, F. Schreck, J. L. Hanssen, C.-S. Chuu, and M. G. Raizen. Bose-Einstein condensate in a box. *Phys. Rev. A*, 71:041604, 2005.

[73] Alan L. Migdall, John V. Prodan, William D. Phillips, Thomas H. Bergeman, and Harold J. Metcalf. First observation of magnetically trapped neutral atoms. *Phys. Rev. Lett.*, 54(24):2596, June 1985.

[74] D.L. Moehring, P. Maunz, S. Olmschenk, K.C. Younge, D.N. Matsukevich, L.-M. Duan, and C. Monroe. Entanglement of single-atom quantum bits at a distance. *Nature*, 449:41, 2007.

[75] C. Monroe. Quantum information processing with atoms and photons. *Nature*, 416:238, 2002.

[76] L. Néel. *C. R. Acad. Sci.*, 203:304, 1936.

[77] K. D. Nelson, X. Li, and D. S. Weiss. Imaging single atoms in a three-dimensional array. *Nature Phys.*, 3:556, 2007.

[78] K.M. O'Hara, M.E. Gehm, S.R. Granade, S. Bali, and J.E. Stable Thomas. Strongly attractive, two-state mixture of lithium fermions in an optical trap. *Phys. Rev. Lett.*, 85:2092, 2000.

[79] M. Olshanii. *Phys. Rev. Lett.*, 81:938, 1998.

[80] R. Orbach. *Phys. Rev.*, 112:309, 1958.

[81] C.J. Pethick and H. Smith. *Bose-Einstein Condensation in Dilute Gases*. Cambridge University Press, Cambridge, UK, 2002.

[82] M. Pons, A. del Campo, J.G. Muga, and M.G. Raizen. Preparation of atomic fock states by trap reduction. *Phys. Rev. A*, 79:033629, 2009.

[83] E.L. Raab, M. Prentiss, A. Cable, S. Chu, and D.E. Pritchard. Trapping of neutral sodium atoms with radiation pressure. *Phys. Rev. Lett.*, 59:2631, 1987.

[84] Mark G. Raizen, Shou-Pu Wan, Chuanwei Zhang, and Qian Niu. Ultra-high fidelity qubits for quantum computing. *arXiv:quant-ph*, 0906:2114, 2009.

[85] C.E. Shannon. *Bell System Tech. J.*, 27:379, 1948.

[86] B. Sutherland. *Phys. Rev. Lett.*, 20:98, 1968.

[87] L. Szilard. On the decrease of entropy in a thermodynamic system by the intervention of intelligent beings. *Z. Physik*, 53:840, 1929. (English translation: Behavioral Science 9:301 1964).

[88] J. E. Thomas, P. R. Hemmer, S. Ezekiel, C. C. Leiby, Jr., R. H. Picard, and C. R. Willis. Observation of ramsey fringes using a stimulated, resonance raman transition in a sodium atomic beam. *Phys. Rev. Lett.*, 48(13):867, 1982.

[89] van der Wal C.H., Eisaman MD, Andre A, Walsworth RL, Phillips DF, Zibrov AS, and Lukin MD. Atomic memory for correlated photon states. *SCIENCE*, 301(5630):196, JUL 2003.

[90] L.R. Walker. *Phys. Rev.*, 116:1089, 1959.

[91] Shou-Pu Wan, Mark G. Raizen, and Qian Niu. Calculation of atomic number states: a bethe ansatz approach. *arXiv:quant-ph*, 0906:2123, 2009.

[92] David S. Weiss, Erling Riis, Yaakov Shevy, P. Jeffrey Ungar, and Steven Chu. Optical molasses and multilevel atoms: experiment. *J. Opt. Soc. Am. B*, 6:2072, 1989.

[93] S.R. Wilkinson, C.F. Bharucha, M.C. Fischer, K.W. Madison, Q. Niu, B. Sundaram, and M.G. Raizen. Experimental evidence for non-exponential decay in quantum tunneling. *Nature*, 387:575, 1997.

[94] C.N. Yang. *Phys. Rev. Lett.*, 19:1312, 1967.

[95] D.D. Yavuz, P. B. Kulatunga, E. Urban, T. A. Johnson, N. Proite, T. Henage, T. G. Walker, and M. Saffman. Fast ground state manip-

ulation of neutral atoms in microscopic optical traps. *Phys. Rev. Lett.*, 96:063001, 2006.

[96] C.W. Zhang, V.W. Scarola, and S. Das Sarma. Initializing a quantum register from mott-insulator states in optical lattices. *Phys. Rev. A*, 75:060301, 2007.

[97] P. Zoller, J. I. Cirac, L.-M. Duan, and J.J. Garcia-Ripoll. Implementing quantum information processing with atoms, ions and photons. *arXiv:quant-ph*, 0405025.

Index

Abstract, ix
Acknowledgments, v
Appendices, 83
artists concept
    2D micro-traps *2D micro-traps*, 43
Atomic Fock States, 55
    quantum computing, 18

Bethe ansatz
    single-particle energy
      sodium atoms, 70
    spurious solution, 107
    states, 62
    weyl chamber, 73
Bibliography, 128

circuit
    stabilization
      laser power, 100
    temperature servo, 98
Clebsch-Gordan, 6
    coefficient, 9
Configuration space
    Configuration space Weyl chamber, 57
configuration space
    boundary condition, 103

decoherence, 50
Dedication, iv
diffraction grating
    blaze, 97
DiVincenzo criteria, 18

Entanglement
    universal gates, 44
excitation
    gap, 79

fidelity
    Fock states
      fermionic, 36
    ground state, 40
Fock states
    ionization thresholds, 75

hole-burning, 93

ionization threshold, 75
issues
    Bethe ansatz, 102

laser power
    laser frequency
      control, 84
laser-culling
    simulation model, 30
laser-culling
    holding-time*holding-time*, 39
    model
      peak ratio, 33
    steps*steps*, 24

magnetic coils
    Ioffe-Pritchard, 12
magnetic sublevels , 6
magneto-optical trap, 16

PID

tuning, 88
polarization gradient field, 6
Preparation
Fock states
fermionic, 24

Quantum Computing with Fermionic Atoms in Optical Trap, 23

Rabi oscillations, 14

saturated absorption spectroscopy, 93
scalability
array of micro-traps, 43
Single particle energies, 74

trap-splitting
simulation model, 35

Ultracold Fock States, 1

Wentzel-Kramers-Brillouin, 111
WKB, 111

Ziegler-Nichols, 87

Vita

Shoupu Wan was born in a small village of Qi Xian (County), He Nan Province, China, on Mar 29th, 1974, the third child of Yu-Zhang Wan and Fu-Lian Ge. On his 5th birthday, he received a gift from his father—a female goat. That goat brought a great population of goats. For the next 10 years or so, he spent considerable time taking care of these goats.

In school, he was far from a "good" student. He often ignored courses that cannot arouse his immediate interests. As a result, he failed in numerous exams of numerous courses. Middle school would have been the end of his education otherwise, if not for his once-in-a-life excellent performance in a physics exam, for which he was admitted to a high school without an exam.

In 1994, he entered the Wu-Han University majoring in physics. During his college time, he again pursued an independent study style. He seldom listened to what the professors talked. He was solely driven by his interests. Of course, he failed to meet some course requirements from time to time. He almost transferred to mathematics, if the school system of China was not so inflexible. Anyway, he managed to receive a B.S. in 1998. After that, he received a M.S. from The Institute of Semiconductors, Chinese Academy of Sciences (Beijing) in 2001.

After roughly a year of little employment, he started PhD program in

the Department of Physics, the University of Texas at Austin in August, 2002. He was first attracted by experimental atomic-molecular-optic (AMO) physics and spent 5 years in the basement of RLM. Then he switched to theoretical AMO physics under the supervision of both Professor Qian Niu and Professor Mark Raizen. He worked with them for less than a year before he got the doctoral degree.

Permanent address: 3372 Lake Austin blvd Apt.A
Austin, Texas 78703

This dissertation was typeset with LaTeX[†] by the author.

[†]LaTeX is a document preparation system developed by Leslie Lamport as a special version of Donald Knuth's TeX Program.